HOKKAIDO UNIVERSITY

Title	Ab initio Molecular Dynamics Analysis based on Reduced-dimensionality Reaction Route Map
Author(s)	Tsutsumi, Takuro
Citation	北海道大学. 博士(理学) 甲第14461号
Issue Date	2021-03-25
DOI	10.14943/doctoral.k14461
Doc URL	http://hdl.handle.net/2115/84529
Type	theses (doctoral)
File Information	TSUTSUMI_Takuro.pdf

Instructions for use

Hokkaido University Collection of Scholarly and Academic Papers : HUSCAP

Ab initio Molecular Dynamics Analysis based on Reduced-dimensionality Reaction Route Map

次元縮約反応経路地図に基づく第一原理分子動力学解析

Takuro Tsutsumi

Graduate School of Chemical Sciences and Engineering

Hokkaido University

March 2021

Contents:

Chapter 1 General Introduction 1
1.1 How Chemical Reactions Occur? 1
1.2 Electronic Structure Theory 4
1.2.1 Born–Oppenheimer Approximation 4
1.2.2 Wave Function Theory 5
1.2.3 Density Functional Theory 9
1.3 Static Reaction Path Analysis 13
1.3.1 Intrinsic Reaction Coordinate 13
1.3.2 Global Reaction Route Mapping Strategy 14
1.4 Molecular Dynamics Simulation 16
1.4.1 On-the-fly Molecular Dynamics 16
1.5 Analysis of Dynamics Effects based on Static Reaction Path 18
1.6 Overview of This Thesis 21
1.7 References 24
Chapter 2 Analysis of On-the-fly Trajectory based on Reaction Route Network 29
2.1 Introduction 29
2.2 On-the-fly Trajectory Mapping Method 32
2.2.1 Linear Distance in Mass-weighted Cartesian Coordinate 32
2.2.2 Nuclear Permutation-Inversion Isomer 33
2.2.3 On-the-fly Trajectory Mapping Procedure 36
2.3 Results and Discussion 39
2.3.1 Global Reaction Route Network of Au_5 Cluster 39
2.3.2 On-the-fly Molecular Dynamics Simulation 44
2.3.3 Bifurcation Mechanisms: A Case of TS1-1d 44
2.3.4 Isomerization Reaction Mechanisms with Dynamics Effects 50

2.4 Conclusion 56

2.5 References 58

Chapter 3 Visualization of Unique Reaction Route Map by Dimensionality Reduction Method 62

3.1 Introduction 62

3.2 Concept of Classical Multi-dimensional Scaling 65

3.3 Results and Discussion 68

3.3.1 Intramolecular Proton Transfer in Malonaldehyde 68

3.3.2 Collision Reaction of $OH^- + CH_3F \rightarrow [CH_3OH\cdots F]^-$ 73

3.3.3 Global Reaction Route Map of Au_5 Cluster 77

3.4 Conclusion 86

3.5 References 88

Chapter 4 Projection of Dynamical Reaction Route onto Reduced-dimensionality Reaction Space 91

4.1 Introduction 91

4.2 Out-of-sample extension of Classical Multidimensional Scaling 94

4.3 Results and Discussion 98

4.3.1 Collision Reaction of $OH^- + CH_3F \rightarrow [CH_3OH\cdots F]^-$ 98

4.3.2 Global Reaction Route Map of Au_5 Cluster 107

4.4 Conclusion 115

4.5 References 117

Chapter 5 Theoretical Study of Excited-state Branching Reaction Mechanisms of α-methyl-cis-stilbene 120

5.1 Introduction 120

5.2 Computational Details 124

5.3 Results and Discussion 125

5.3.1 Geometries of Minima, TSs, and S_1/S_0-MECIs 125

5.3.2 Reaction Pathways in the S_1 State 131

5.3.3 Excited State On-the-fly MD Simulations 136

5.4 Conclusion 141

5.5 References 143

Chapter 6 Visualization of Multi-state Potential Energy Landscape: A Case Study on Excited-state Branching Reaction of Stilbene 147

6.1 Introduction 147

6.2 Database of Molecular Structures in the S_0 and S_1 states 152

6.3 Results and Discussion 158

6.3.1 Ground-state Potential Energy Landscape 158

6.3.2 Excited-state Potential Energy Landscape 161

6.3.3 Multi-state Potential Energy Landscape 164

6.3.4 On-the-fly Trajectory Analysis based on Multi-state Landscape 167

6.3.5 Excited-state Reaction Route Maps of Stilbene Derivatives 170

6.4 Conclusion 174

6.5 References 176

Chapter 7 General Conclusion 180

Acknowledgments 187

Chapter 1

General Introduction

1.1 How Chemical Reactions Occur?

A chemical reaction is a multi-step process with chemical transformations of substances, and it proceeds from a reactant through intermediates to a final product. The single reaction is regarded as an elementary reaction process, which has been recognized together with the development of reaction kinetics by Maxwell and Boltzmann's formulation of the particle probability distribution for gaseous molecules[1–3] and Arrhenius' concept of the activation energy[4]. Hence, chemists have interpreted the elementary reaction as a process connecting a reactant and a product *via* an activated complex. Marcelin,[5] Eyring,[6] and Wigner[7] introduced the concept of "*transition state*" and developed transition state theory concerned the activation barrier of elementary reaction. Polanyi studied a collision reaction for atom-diatom systems in the gas phase[8–10] and discussed the efficient energy disposal to the translational and vibrational degrees of freedom, which induced during the elementary reaction process.[8] Also, Herschbach, Lee, and Polanyi were awarded the Nobel Prize in Chemistry in 1986 "*for contributions concerning the dynamics of chemical elementary processes.*" In this way, the driving forces behind chemical reactions and their mechanisms have been elucidated based on elementary reaction processes.

Photochemistry is a study concerned with electronically excited states produced by the interaction between light and molecules. After light irradiation, a molecule experiences a vertical transition from a ground state to electronically excited states. This process is described by the Franck–Condon principle, which relates the intensity of classical vibrational transitions to the overlap of vibrational wave functions. In the early days of photochemistry, there was an interest in light absorption and luminescence. Jablonski is a pioneer in fluorescence spectroscopy and defined a schematic diagram to illustrate photochemical reaction processes, including radiative and non-radiative transitions.[11] This diagram is called the Jablonski diagram and has been widely used in photochemistry. Lewis and Kasha discovered that a metastable state originating phosphorescence is an excited triplet state.[12,13] From such perspectives on fluorescence and phosphorescence, Kasha proposed a rule to interpret the emission spectrum: "*The emitting level of a given multiplicity is the lowest excited level of that multiplicity.*"[14] This is a well-known Kasha's law and states that the luminescence originates from the vibrational ground state of the lowest excited state.

In theoretical chemistry, the transitions of excited molecules occur at the intersection of electronic states, and these intersections between the same spin states are known as conical intersections.[15] On the other hand, a transition between different spin states is an intersystem crossing. El-Sayed studied a transition between singlet and triplet states theoretically and associated the transition probability with the spin multiplicity and the orbital symmetry. This rule is known as El-Sayed law, estimating the relative magnitude of spin-orbit interactions from the molecular orbitals.[16,17] From these results, the photochemical reaction mechanism is summarized as follows: After excitation, when the molecules cannot energetically reach the crossing regions between the electronic states, they relax through the radiative processes with fluorescence or phosphorescence; in contrast, when they can reach the crossing regions, they will relax through the competitive processes including non-radiative and radiative processes. Thus, the conical intersection and the intersystem crossing play a significant role in elucidating the photochemical reaction mechanisms.[18,19]

1.2 Electronic Structure Theory

Electronic structure theory is the study of electrons in a substance and provides a theoretical way to reveal chemical reaction mechanisms. The Schrödinger equation proposed in 1926 is a basic equation in quantum mechanics[20] and is also a central role in the electronic structure theory. This section introduces the electronic structure theory as the foundation of the elucidation of chemical reaction mechanisms based on quantum chemistry.[21,22]

1.2.1 Born–Oppenheimer Approximation

The non-relativistic time-independent Schrödinger equation is given by

$$\mathbf{H}\left|\Phi\right\rangle = E\left|\Phi\right\rangle \tag{1-1}$$

where **H** is the Hamiltonian operator for nuclei and electrons, and E is the energy eigenvalue. The Hamiltonian operator for a molecular system of N electrons and M nuclei is

$$\begin{aligned}\mathbf{H} = &-\sum_{i=1}^{N}\frac{1}{2}\nabla_i^2 + \sum_{i=1}^{N}\sum_{j>i}^{N}\frac{1}{r_{ij}} - \sum_{i=1}^{N}\sum_{A=1}^{M}\frac{Z_A}{r_{iA}} \\ &-\sum_{A=1}^{M}\frac{1}{2M_A}\nabla_A^2 + \sum_{A=1}^{M}\sum_{B>A}^{M}\frac{Z_A Z_B}{R_{AB}}\end{aligned} \tag{1-2}$$

where r_{ij}, r_{iA}, R_{AB}, M_A, and Z_A are the displacements between the ith electron and the jth electron, the ith electron and the Ath nucleus, the Ath nucleus, the Bth nucleus, and the mass and the atomic charge of nucleus A, respectively. Since nuclei are about 1830 times heavier than electrons, it is appropriate for the quantum chemical calculation to separate the electron motions from the nucleus motions. This approximation is called the Born–Oppenheimer approximation.[23] Under this approximation, the electrons are treated as traveling in the field of fixed nuclei, and then the electronic Hamiltonian is given as follow:

$$\mathbf{H}_{elec} = -\sum_{i=1}^{N} \frac{1}{2} \nabla_i^2 + \sum_{i=1}^{N} \sum_{j>i}^{N} \frac{1}{r_{ij}} - \sum_{i=1}^{N} \sum_{A=1}^{M} \frac{Z_A}{r_{iA}} \tag{1-3}$$

where the nuclear coordinates depend on parametrically. In other words, the Born–Oppenheimer approximation neglects the fourth (kinetic energy for nuclei) and the fifth (the nuclear repulsion) term of equation (1-2), respectively. The electronic Schrödinger equation is defined as

$$\mathbf{H}_{elec} \left| \Phi_{elec} \right\rangle = E_{elec} \left| \Phi_{elec} \right\rangle , \tag{1-4}$$

and the total energy E is given by

$$E = E_{elec} + \sum_{A=1}^{M} \sum_{B>A}^{M} \frac{Z_A Z_B}{R_{AB}} . \tag{1-5}$$

Since the electronic energy E_{elec} depends on the nuclear coordinates, a set of total energy E along a chemical reaction process provides an adiabatic potential energy surface.

1.2.2 Wave Function Theory

The electron Schrödinger equation cannot solve analytically except for the Hydrogen atom and Hydrogen-like atoms. This problem is a well-known many-electron problem, and the Hartree-Fock theory[24] overcomes it by introducing a mean-field approximation. Such a Schrödinger equation based theory is called the wave function theory.

In the Hartree-Fock theory, an *N*-electron wave function is described by a single-configuration Slater determinant,

$$|\Psi\rangle = |\chi_i(\mathbf{x}_1)\cdots\chi_j(\mathbf{x}_N)\rangle = (N!)^{-\frac{1}{2}}\begin{vmatrix} \chi_i(\mathbf{x}_1) & \cdots & \chi_j(\mathbf{x}_1) \\ \vdots & \ddots & \vdots \\ \chi_i(\mathbf{x}_N) & \cdots & \chi_j(\mathbf{x}_N) \end{vmatrix} \tag{1-6}$$

where $\chi(\mathbf{x}_i)$ is a spin orbital for *i*th electron $\mathbf{x}_i$. The Slater determinant satisfies the antisymmetric principle and indicates a single configuration wave function. The basic idea of Hartree-Fock theory is a mean-field approximation that is to regard many-electron interactions as a one-electron interaction between an electron and an averaged electrostatic potential for other electrons. Such approximation is introduced by a Fock operator

$$f(i) = -\frac{1}{2}\nabla_i^2 - \sum_{A=1}^{M}\frac{Z_A}{r_{iA}} + v^{\mathrm{HF}}(i) \tag{1-7}$$

where $v^{\mathrm{HF}}(i)$ is the averaged electrostatic potential affecting the *i*th electron. Thus, the Hartree-Fock equation is given by

$$f(i)\chi(\mathbf{x}_i) = \varepsilon_i\chi(\mathbf{x}_i). \tag{1-8}$$

where the ε_i indicates orbital energy. Since the averaged potential $v^{\mathrm{HF}}(i)$ in the Fock operator depends on the spin orbitals of electrons, the Hartree-Fock equation is nonlinear, and then it needs to be solved by the self-consistent-field (SCF) method. In 1951, Roothaan proposed the procedure to solve the Hartree-Fock equation algebraically[25], and it is called the Roothaan equation. This procedure has been utilized for the modern quantum chemical calculation programs. As the Hartree-Fock theory, the procedure solving the Schrödinger equation without empirical parameters is called the *ab initio* method.

For discussions on various chemical problems quantitively, the electron correlation plays a significant role. The electron correlation is the difference between exact energy and Hartree-Fock energy and conceptually divided into a non-dynamical and dynamical correlation. The former is caused by degenerated electron configurations, and the latter is caused by approaching two electrons, which can not be described under the mean-field approximation. Thus, for uncovering dissociation mechanisms, bond-cleavages and -formations, and excited state reactions, it is necessary to handle both correlations well-balanced. In the practical computations, the non-dynamical correlations are incorporated by a multi-configurational wave function, while the dynamical correlations are incorporated by considering electron transitions from occupied orbitals to unoccupied ones.

As more sophisticated wave function methods, post-Hartree-Fock methods, such as the Møller–Plesset method, the configuration interaction method, and the coupled cluster method, have been proposed. The Møller–Plesset method incorporates the electron correlation by the perturbation theory, and the second, third, fourth-order Møller–Plesset (MP2, MP3, and MP4) methods are well-known. The configuration interaction (CI) method generates a multi-configurational wave function, a linear combination of the ground state electronic configuration and multi-electron excitation Slater determinants, and optimizes each coefficient by the variational method. In this scheme, one can mainly handle the non-dynamical correlation. The CI method considered all possible electronic configurations is called the Full-CI method. The coupled-cluster (CC) method uses an exponential cluster operator to describe multi-electron excitations and incorporates the electron correlation by multi-configurational Slater determinations and electron excitations to unoccupied orbitals. The coupled-cluster singles, doubles, and perturbative triples, CCSD(T), provides a good agreement with experimental results, and therefore it is called a gold standard in quantum chemistry.

On the other hand, in the region where two or more electronic states get degenerate, the system should be defined as a multi-configurational wave function rather than a single configurational wave function. This concept is called the multi-configurational method. The multi-configurational SCF (MCSCF) method is well-known and determines both molecular orbital coefficients and CI coefficients simultaneously. The complete active space SCF (CASSCF) method is one of the MCSCF and performs the Full-CI procedure in the active space where selected molecular orbitals and electrons are only included. The complete active space second-order perturbation theory (CASPT2) incorporates the further electron correlation, which is neglected in the CASSCF, by the second-order perturbation theory, and such method is called the multireference method. Sometimes, the electron correlation incorporated by MCSCF is regarded as the non-dynamical correlation, while the one by the multireference method based on the MCSCF is regarded as the dynamical correlation. When two or more electronic states get degenerate, one needs to employ the multi-state method, which handles multi-electronic states simultaneously, and the state-averaged CASSCF (SA-CASSCF) and the multi-state CASPT2 (MS-CASPT2) are well-known.

1.2.3 Density Functional Theory

The density functional theory (DFT)[26] provides a method to solve the Schrödinger equation based on the Hohenberg-Kohn theorem[27], which shows a one-to-one correspondence between the molecular properties obtained from the multi-electron wave function and an electron density with three variables. The molecular energy is a functional of the electron density, and the energy functional is a solution of the Kohn-Sham equation[28] derived from the Hohenberg-Kohn theorem as follow:

$$\begin{aligned} E[\rho] &= T_S[\rho] + V_{ne}[\rho] + V_{ee}[\rho] \\ &= T_S[\rho] + V_{ne}[\rho] + J[\rho] + E_{XC}[\rho] \end{aligned}, \tag{1-9}$$

where $T_S[\rho]$, $V_{ne}[\rho]$, $V_{ee}[\rho]$, $J[\rho]$, and $E_{XC}[\rho]$ is a kinetic energy functional, an electron-nucleus potential functional, an electron-electron potential functional, a Coulomb potential functional, and an exchange-correlation potential functional, respectively. Although $T_S[\rho]$, $V_{ne}[\rho]$, and $J[\rho]$ can be determined by Kohn-Sham orbitals which are provided by the Kohn-Sham equation, there is no exact functional for $E_{XC}[\rho]$. Generally, the exchange-correlation functional is composed of an exchange functional $E_X[\rho]$ and a correlation functional $E_C[\rho]$. The latter one indicates the effects of electron correlation neglected in the Hartree-Fock theory. The Hohenberg-Kohn theorem guarantees that the universal functional of the electron density provides the exact electron energy; however, it does not say how to generate the universal functional. Hence many researchers have developed various exchange and correlation functionals based on the concepts (or assumptions) of a local density approximation (LDA), a generalized gradient approximation (GGA), a hybrid of the Hartree-Fock exchange term, and a semi-empirical way.

The time-dependent Kohn-Sham equation derived from a Runge-Gross theorem is a way to calculate the excited-state and provides the excitation energy by the linear response theory. This procedure is called a time-dependent DFT (TDDFT) method. The computational cost of TDDFT is considerably lower than the excited state calculation based on the wave function theory, and thus the TDDFT is acceptable for the investigation of excited state chemical properties. However, the TDDFT does not include the multi-electron excitation configurations related to the electron correlation and provides a discontinuous potential energy curve at a crossing region between the ground state and the first excited state because of the switch of the reference state (ground state). Therefore, the applications of TDDFT for the excited state are limited.

Spin-flip TDDFT overcomes the TDDFT limitations. In the TDDFT, the reference state is the ground state electronic configuration obtained by the DFT calculation, and then the one-electron excitation is considered. In contrast, the spin-flip TDDFT refers to the open-shell triplet first excited state electronic configuration and generates a muli-configurational wave function as a linear combination of the several configurations generated by the one-electron excitation and the spin flipping (shown in **Figure 1.1**). Consequently, the spin-flip procedure generates four spin-adapted configurations: the closed-shell singlet configuration, the open-shell singlet and triplet one-electron excited configurations, and the double-electrons excited configuration from the highest occupied molecular orbital (HOMO) to the lowest unoccupied molecular orbital (LUMO). This procedure also generates other configurations; however, these configurations lead to the spin-contaminated electronic states called mixed states.

The expectation of $\mathbf{S}^2$ operator $\left\langle \mathbf{S}^2 \right\rangle$ in the spin-flip TDDFT typically indicates 0 for a singlet state, 2 for a triplet state, 1 for a mixed state. However, around the energetically degenerating region, the spin-contamination affects the expectation of $\mathbf{S}^2$, and therefore it was not easy to follow the target state by the expectation values. In 2014, the T_{SF}-index method that specifies the triplet state from the results of spin-flip TDDFT was proposed[29], and this technique helps to follow a singlet target state by neglecting the triplet states. The T_{SF}-index is given by

$$T_{SF} = V^{\text{HOMO-LUMO}} + \left\langle \mathbf{S}^2 \right\rangle \tag{1-10}$$

where $V^{\text{HOMO-LUMO}}$ indicates the squared sum of the configuration interaction coefficients in terms of four electronic configurations: the closed-shell singlet, the open-shell singlet and triplet one-electron excitation, and the double-electrons excitation configuration. $V^{\text{HOMO-LUMO}}$ is close to 1 when the electronic states are mainly composed of four electronic configurations. Hence, the T_{SF}-index becomes relatively larger for the triplet states, and then one can recognize the triplet states from the spin-flip TDDFT results.

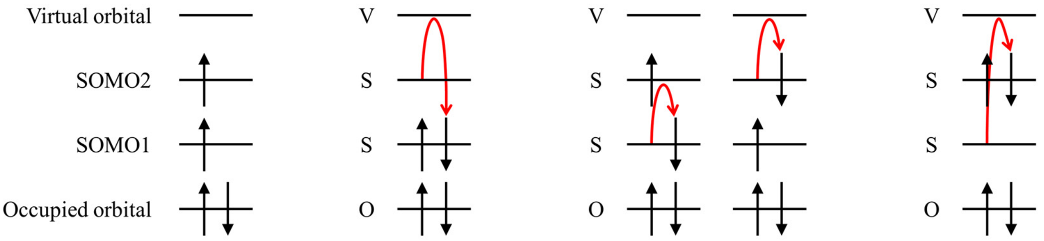

(a) Reference state

(b) Closed-shell singlet state

(c) Open-shell singlet and triplet state

(d) Doubly-excited state

Virtual orbital
SOMO2
SOMO1
Occupied orbital
V
S
S
O
V
S
S
O
V
S
S
O

(e) Mixed states

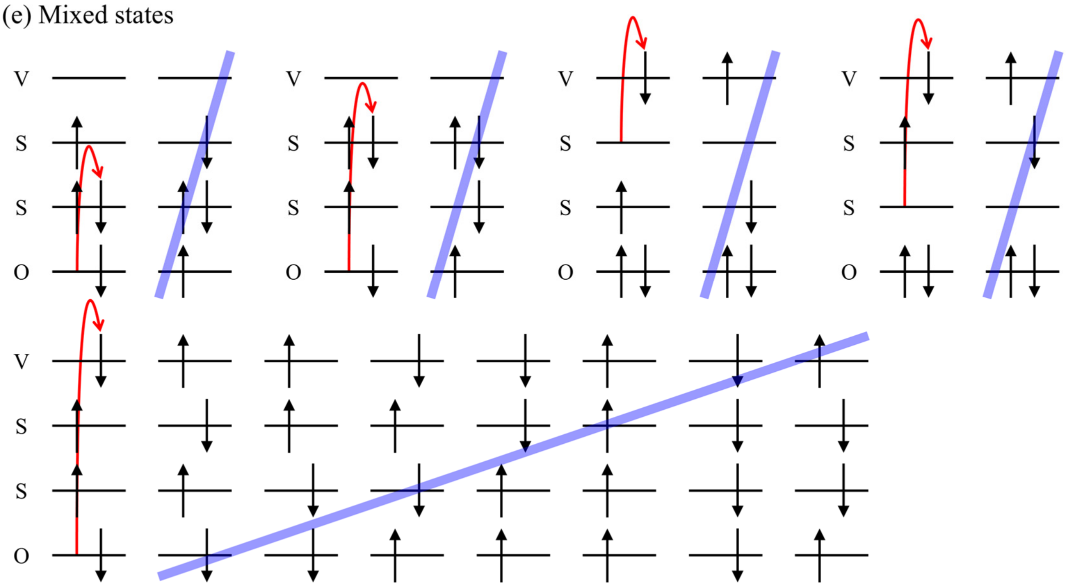

V
S
S
O
V
S
S
O
V
S
S
O
V
S
S
O
V
S
S
O

Figure 1.1. (a) The reference triplet state and (b-e) the electronic states generated by the one-electron spin-flip transition, with their missing configurations depicted by blue slashes: (b) the singlet ground state, (c) the doubly excited state, (d) the open-shell singlet and triplet states, and (e) the mixed states of singlet, triplet, and quintet.

1.3 Static Reaction Path Analysis

This section briefly introduces a representative reaction path on the potential energy surface and an automatic reaction path search method called a global reaction route mapping (GRRM).

1.3.1 Intrinsic Reaction Coordinate

A chemical reaction is a process that transforms a set of chemical compounds to another and is typically a multi-step process. The elementary reaction is a single reaction process which is assumed to pass through a transition state. From the viewpoint of theoretical chemistry, a chemical reaction is a path starting from a reactant region to a product region on the potential energy surface (PES), which depends on nuclear coordinates parametrically. Therefore, the elementary reaction process may be defined as a one-dimensional curve connecting two minima *via* a first-order saddle point on the PES. Note that a minimum indicates a stable structure (denoted as MIN), while a first-order saddle point indicates a transition state structure (denoted as TS).

The PES for an N atomic molecule (N denotes the number of atoms) is in the $3N-6$ dimensional space except for the 6-dimensional invariant subspace for translational and rotational degrees of freedoms. Here, the question emerges: How should one define such an elementary reaction path (curve) on the $3N-6$ dimensional PES? In 1970, Fukui proposed an intrinsic reaction coordinate (IRC) uniquely defined as the steepest descent path starting from TS in the mass-weighted Cartesian coordinate space. For a non-equilibrium structure, the tangent unit vector of IRC is defined as follow:

$$\mathbf{v}(s) = \frac{d\mathbf{X}_{\mathrm{IRC}}(s)}{ds} = -\frac{\nabla V(\mathbf{X})}{\left|\nabla V(\mathbf{X})\right|} \tag{1-11}$$

where $\mathbf{X}$, V, and $\mathbf{X}_{\mathrm{IRC}}(s)$ are mass-weighted $3N$ Cartesian coordinates, adiabatic potential energy, and a mass-weighted $3N$ Cartesian coordinates at a reaction coordinate s on the IRC. In the actual IRC calculation, first, one needs to add a displacement toward a direction of imaginary vibrational mode to the initial molecular structure, TS, because the potential gradient of TS is precisely 0. Then, the IRC keeps descending the PES toward the direction of equation (1-11) with a given displacement until the potential gradient gets close to 0. The IRC analysis provides intuitive knowledge for the elementary reaction process, such as variations of geometrical structures, potential energy, and molecular orbitals. Thus, the IRC calculation is a powerful tool to elucidate chemical reaction mechanisms and is implemented in various quantum chemistry calculation programs.

1.3.2 Global Reaction Route Mapping Strategy

To investigate chemical reaction mechanisms included a set of elementary reactions, one needs to find TS structures, which correspond to initial molecular geometries of IRC calculations. A standard approach finding a stationary point (e.g., minima and saddle points) on the PES is a (constrained) geometry optimization, where presuming an appropriate initial structure is significant. However, because a TS structure is very different from a stable structure in the ground state, it is hard to presume an initial structure for the TS optimization. Even if a TS optimization provides a TS structure connecting desired MINs, there may also be another TS with lower activation energy.

In 2004, Ohno and Maeda proposed the anharmonic downward distribution following (ADDF) method, one of the automated reaction path search methods, based on a scaled hyper-sphere search (SHS) method. The ADDF method enables us to search TS structures as climbing the PES from a given MIN by focusing on a difference between harmonic potential energy and real potential energy. By repeating the ADDF method and the IRC calculation, one can generate a chemical reaction route network. For predicting chemical reaction paths more efficiently, Maeda and coworkers also proposed the artificial force induced reaction (AFIR) method, which pushes or pulls two fragments in a molecule together. In the last decade, the global reaction route mapping (GRRM) program, in which both the ADDF and the AFIR are available, has been developed and applied to organic chemistry, surface chemistry, biochemistry, and photochemistry. Recently, a navigating system based on the kinetic simulation analysis is also developed and accelerates the automated search of feasible reaction paths under experimental conditions.

1.4 Molecular Dynamics Simulation

Due to kinetic energy, an actual reaction path wanders from a reactant to a product region on the PES rather than precisely follow IRC paths. Therefore, clarifying not only static reaction paths but also dynamical reaction processes are necessary to elucidate actual chemical reaction mechanisms. Molecular dynamics (MD) is a simulation method that includes dynamic aspects and provides time evolution pictures of the molecular system traveling on the PES.

1.4.1 On-the-fly Molecular Dynamics

On-the-fly MD is a classical trajectory method that does not require a pre-defined potential function. This method calculates atomic forces derived from WFT or DFT and then evolves the molecular coordinate and velocity by Newton's equation of motion. Therefore, the on-the-fly MD provides a full-dimensional trajectory that includes all degrees of freedom of the molecular system, in contrast to an MD simulation with a potential function defined by selected degrees of freedom. The target of on-the-fly MD has now been applied to excited-state chemical reactions such as photoisomerization and ultrafast relaxation processes. The term *ab initio* MD, which is included in the title of this thesis, is used as an MD method for deriving atomic forces by *ab initio* method. Frequently, *ab initio* calculation is used as a term of a quantum chemistry calculation and is widely recognized, but historically it refers only to WFT. Therefore, strictly speaking, a DFT-based MD is not called *ab initio* MD. Such an MD is often called a first-principles MD.[30] Accordingly, in this thesis, I use the term of on-the-fly MD in the sense of an MD method that derives atomic forces "*on-the-fly*" by the quantum chemistry calculation involving WFT and DFT.

The molecular system on the excited state PES transitions to other electronic states *via* internal conversions to another same spin state and intersystem crossings to another different spin state and finally decays to the ground state. Therefore, it is crucial to deal with the transitions between electronic states for the excited-state MD simulation. Tracking the probability of internal conversions and inter-symmetric crossings requires non-adiabatic couplings and spin-orbit interactions. However, the computational cost for these terms is very high, and thus the application of the excited state on-the-fly MD is limited. As a scheme to incorporate non-adiabatic transitions based on multiple adiabatic electronic states, Tully proposed a surface hopping method to describe the transition from a state to another depending on a non-adiabatic transition probability.[31,32] This scheme, called the Tully's fewest switches algorithm, has been employed as the basis of the non-adiabatic transition dynamics procedures.[33,34] Zhu and Nakamura formulated a two-state one-dimensional non-adiabatic transition probability using diabatic gradients,[35–38] and this Zhu–Nakamura theory was extended to a multidimensional system in 2014.[39] Recently, a non-adiabatic transition MD scheme combining the Zhu–Nakamura theory and Tully's surface hopping has been applied for various excited state reactions.[40,41]

1.5 Analysis of Dynamics Effects based on Static Reaction Path

The PES is a stage for chemical reactions, and if the entire PES is already known, one can reveal all possible chemical reactions. However, generating the full-dimensional PES is limited to a small molecular system because of the numerous electronic structure calculations: If one needs 10 points for one degree of freedom, this requires 10^{3N-6} quantum chemical calculations to generate a PES for an N atomic system. Hence, no matter how fast computation becomes, generating the entire PES is hopeless.

The IRC is a one-dimensional minimum energy path and provides a representative reaction path on a $3N-6$ dimensional PES. In the last decade, the global reaction route mapping (GRRM) method has enabled us to generate a reaction route map and has revealed ideal chemical reaction mechanisms on the PES. However, dynamical aspects are also essential for elucidating actual chemical reactions, and the chemical reactions are often driven by kinetic energy. The on-the-fly MD is a full-dimensional classical trajectory method and gives pictures in which the molecular system with kinetic energy travels on the PES. Of course, the on-the-fly trajectory provides a dynamical aspect of chemical reaction; however, the analysis of complicated dynamical reaction processes requires chemical insights, and no unified analysis way has been proposed. From the viewpoint of molecular dynamics, the IRC is regarded as a trajectory with an infinitesimal velocity, and therefore it is utilized as a reference path for interpreting on-the-fly trajectories.

Miller, Handy, and Adams proposed a reaction path Hamiltonian, a pioneering study of reaction dynamics analysis based on IRC.[42] This scheme describes a chemical reaction in terms of a reaction coordinate and $3N-7$ vibrational coordinates perpendicular to the reaction coordinate, indicating a dynamical reaction process near the IRC based on adiabatic vibrational coordinates. Kato and Morokuma improved the reaction path Hamiltonian by considering the deviation of the origin of vibrational coordinates due to the IRC curvature and discussed the energy partitionings along the IRC.[43] Taketsugu and Gordon also developed a dynamical reaction path analysis method based on a two-dimensional reaction plane, which is determined by the reaction coordinate and the IRC curvature coordinate, and $3N-8$ dimensional vibrational coordinates orthogonal to the reaction plane and discussed dynamical reaction paths nearby the IRC.[44] Such deviation from a reference path by a curvature of path is known as a bobsled effect.[45] Also, Kraka and coworkers reported a method to elucidate the specified modes excited through the curved IRC by projecting the reaction path curvature vector to the vibrational modes orthogonal to IRC.[46–48]

Another well-known dynamic reaction behavior is a bifurcation reaction because of IRC instability.[49–52] The bifurcation reaction occurs when the shape of PES for the vibrational modes orthogonal to the IRC changes from a valley to a ridge. Therefore, the molecular system with kinetic energy deviates from the IRC around the instability point. This point is called a valley-ridge transition (VRT) point, and Taketsugu and Hirano investigated the bifurcation mechanism based on the second-order Jahn-Teller theory and concluded that the IRC instability emerges by the vibrational interaction between the electronic ground-state and the electronic excited-states.[53] Such bifurcation reactions are not quite unusual and have been reported in organic chemistry[54], metal cluster chemistry[55], and complex chemistry[52]. A post-transition state bifurcation has recently received much attention and has been reported in biosynthesis[56], organic[57], and organometallic[58] reactions.

Many researchers have developed methods for analyzing reaction dynamics based on a single IRC. However, the on-the-fly trajectory included the effect of kinetic energy does not always move around only the neighborhood of a single IRC. Furthermore, in high-energy ground state reactions and excited state reactions, since molecules have considerable kinetic energy, the single IRC-based approaches for dynamical reaction processes break down. Therefore, a new reaction dynamics analysis method based on the multi-IRCs has been desired.

1.6 Overview of This Thesis

This thesis is composed of seven chapters. **Chapter 1** is the general introduction and reviewed the analysis ways of chemical reaction mechanisms, including both the static and dynamic approaches in quantum chemistry.

Chapter 2 proposes a general approach to analyze the on-the-fly trajectory based on multi-IRCs, named the on-the-fly trajectory mapping method. This method requires the mass-weighted Euclid distance between the reference structures on the PES and each molecular structure along the on-the-fly trajectory and then clarifies a dynamical reaction route by assigning the trajectory to a time-series data of reference structures given the lowest linear distance. In this chapter, I apply it to the ground-state isomerization reaction of an Au_5 cluster. The reference structures involve five MINs and 14 TSs obtained from the global reaction route map by the GRRM program, and the 200 on-the-fly trajectories are analyzed. Consequently, I uncover dynamical reaction mechanisms, such as the bifurcation reaction and the IRC-jump behavior from one IRC to another.[59]

The on-the-fly trajectory mapping method enables us to trace a dynamical reaction route based on the PES; however, it is still challenging to visualize a chemical reaction process in the two- and three-dimensional space due to the multi-dimensionality. **Chapter 3** focuses on a classical multidimensional scaling (CMDS) method, which is one of the dimensionality reduction methods. The CMDS technique is able to embed multi-dimensional data into a lower-dimensional subspace so that the mutual distance relationship is kept as much as possible. In this chapter, I apply the CMDS method for the IRC of intramolecular proton transfer reaction of malondialdehyde; the IRC of collision reaction of $OH^- + CH_3F \rightarrow CH_3OH + F^-$; and the global reaction route map of isomerization reaction of Au_5, and I attempt to visualize these chemical reaction paths in the two-dimensional coordinate space.[60]

A remaining problem for on-the-fly trajectory analysis is to project the dynamical reaction processes onto the reduced-dimensionality reaction space. Such a problem can be resolved by using the out-of-sample extension of CMDS (oCMDS). The oCMDS method makes it possible to project out-of-sample data (the trajectory) into the reduced-dimensionality subspace (the reduced IRC network) given by the CMDS method. In **Chapter 4**, I employ the oCMDS method to the IRC of $OH^- + CH_3F \rightarrow CH_3OH + F^-$ and the global reaction route map of Au_5 and then investigate the dynamical reaction processes based on the two- and three-dimensional chemical reaction subspace.[61]

Chapter 5 examines the excited-state branching reaction for α-methyl-cis-stilbene (*cis*-mSB), which undergoes the cis-trans photoisomerization reaction and the photocyclization, based on both the excited-state reaction path analysis and the on-the-fly molecular dynamics simulations at the Spin-flip TDDFT level of theory. The excited-state potential energy surface related to the branching reaction is embedded into the two-dimensional coordinate space determined by intuitively selected internal coordinates, and the excited-state reaction dynamics are analyzed based on this reduced-dimensionality subspace. From the viewpoint of the methyl-substituent effects, I also investigate the branching mechanism by comparison with the previous theoretical studies on stilbene (SB) and 1,1′-dimethyl-stilbene (dmSB).[62]

In **Chapter 6**, I extend the present reduced-dimensionality strategy to the excited-state reaction analysis. *Cis*-stilbene is a well-known molecule in which the *cis*-*tran*s photoisomerization competes with the photocyclization after the ππ* excitation, and therefore, it is necessary to investigate the excited-state reaction dynamics and the non-radiative decay processes to the ground state. In this chapter, I construct a multi-state reaction route map determined by representative molecular structures in both the ground and excited states using the CMDS method. In addition, I comprehensively discuss both the photoexcited reactions and the non-radiative relaxation processes by projecting the on-the-fly trajectory onto the multi-state reduced-dimensionality potential energy landscape.

Chapter 7 is a general conclusion, and I summarize this thesis and outline future directions.

1.7 References

(1) Maxwell, J. C. Illustrations of the Dynamical Theory of Gases. —Part I. On the Motions and Collisions of Perfectly Elastic Spheres. *London, Edinburgh, Dublin Philos. Mag. J. Sci.* **1860**, *19*, 19–32.

(2) Maxwell, J. C. Illustrations of the Dynamical Theory of Gases. —Part II. On the Process of Diffusion of Two or More Kinds of Moving Particles among One Another. *London, Edinburgh, Dublin Philos. Mag. J. Sci.* **1860**, *20*, 21–37.

(3) Boltzmann, L. Über Die Beziehung Zwischen Dem Zweiten Hauptsatze Der Mechanischen Wärmetheorie Und Der Wahrscheinlichkeitsrechnung Resp. Den Sätzen Über Das Wärmegleichgewicht. *Akad. der Wissenschaften Wien Math. Klasse Sitzungsberichte Abteilung II* **1877**, *76*, 373–435.

(4) Arrhenius, S. Über Die Dissociationswärme Und Den Einfluss Der Temperatur Auf Den Dissociationsgrad Der Elektrolyte. *Zeitschrift für Phys. Chemie* **1889**, *4U*.

(5) Marcelin, M. R. Contribution à l'étude de La Cinétique Physico-Chimique. *Ann. Phys. (Paris).* **1915**, *9*, 120–231.

(6) Eyring, H. The Activated Complex in Chemical Reactions. *J. Chem. Phys.* **1935**, *3*, 107–115.

(7) Wigner, E. Calculation of the Rate of Elementary Association Reactions. *J. Chem. Phys.* **1937**, *5*, 720–725.

(8) Polanyi, J. C. Concepts in Reaction Dynamics. *Acc. Chem. Res.* **1972**, *5*, 161–168.

(9) Polanyi, J. C. Some Concepts in Reaction Dynamics. *Science* **1987**, *236*, 680–690.

(10) Polanyi, J. C.; Zewail, A. H. Direct Observation of the Transition State. *Acc. Chem. Res.* **1995**, *28*, 119–132.

(11) Jablonski, A. Efficiency of Anti-Stokes Fluorescence in Dyes. *Nature* **1933**, *131*, 839–840.

(12) Lewis, G. N.; Kasha, M. Phosphorescence and the Triplet State. *J. Am. Chem. Soc.* **1944**, *66*, 2100–2116.

(13) Lewis, G. N.; Kasha, M. Phosphorescence in Fluid Media and the Reverse Process of Singlet-Triplet Absorption. *J. Am. Chem. Soc.* **1945**, *67*, 994–1003.

(14) Kasha, M. Characterization of Electronic Transitions in Complex Molecules. *Discuss. Faraday Soc.* **1950**, *9*, 14.

(15) Teller, E. The Crossing of Potential Surfaces. *J. Phys. Chem.* **1937**, *41*, 109–116.

(16) El-Sayed, M. A. Spin—Orbit Coupling and the Radiationless Processes in Nitrogen Heterocyclics. *J. Chem. Phys.* **1963**, *38*, 2834–2838.

(17) El-Sayed, M. A. Triplet State. Its Radiative and Nonradiative Properties. *Acc. Chem. Res.* **1968**, *1*, 8–16.

(18) Yarkony, D. R. Diabolical Conical Intersections. *Rev. Mod. Phys.* **1996**, *68*, 985–1013.

(19) Domcke, W.; Yarkony, D. R. Role of Conical Intersections in Molecular Spectroscopy and Photoinduced Chemical Dynamics. *Annu. Rev. Phys. Chem.* **2012**, *63*, 325–352.

(20) Schrödinger, E. An Undulatory Theory of the Mechanics of Atoms and Molecules. *Phys. Rev.* **1926**, *28*, 1049–1070.

(21) Szabo, A.; Ostlund, N. S. *Modern Quantum Chemistry: Introduction to Advanced Electronic Structure Theory*; Dover Publications, Inc: Mineola, N.Y, 2012.

(22) 常田貴夫. 密度汎関数法の基礎; 講談社, 2012.

(23) Born, M.; Oppenheimer, R. Zur Quantentheorie Der Molekeln. *Ann. Phys.* **1927**, *389*, 457–484.

(24) Fock, V. Näherungsmethode Zur Lösung Des Quantenmechanischen Mehrkörperproblems. *Zeitschrift für Phys.* **1930**, *61*, 126–148.

(25) Roothaan, C. C. J. New Developments in Molecular Orbital Theory. *Rev. Mod. Phys.* **1951**, *23*, 69–89.

(26) Thomas, L. H. The Calculation of Atomic Fields. *Math. Proc. Cambridge Philos. Soc.* **1927**, *23*, 542–548.

(27) Hohenberg, P.; Kohn, W. Inhomogeneous Electron Gas. *Phys. Rev.* **1964**, *136*, B864–B871.

(28) Kohn, W.; Sham, L. J. Self-Consistent Equations Including Exchange and Correlation Effects. *Phys. Rev.* **1965**, *140*, A1133–A1138.

(29) Maeda, S.; Harabuchi, Y.; Taketsugu, T.; Morokuma, K. Systematic Exploration of Minimum Energy Conical Intersection Structures near the Franck–Condon Region. *J. Phys. Chem. A* **2014**, *118*, 12050–12058.

(30) Car, R.; de Angelis, F.; Giannozzi, P.; Marzari, N. First-Principles Molecular Dynamics. In *Handbook of Materials Modeling*; Springer Netherlands: Dordrecht, 2005; pp 59–76.

(31) Tully, J. C.; Preston, R. K. Trajectory Surface Hopping Approach to Nonadiabatic Molecular Collisions: The Reaction of H + with D 2. *J. Chem. Phys.* **1971**, *55*, 562–572.

(32) Tully, J. C. Molecular Dynamics with Electronic Transitions. *J. Chem. Phys.*

1990, *93*, 1061–1071.

(33) Kamiya, M.; Taketsugu, T. Ab Initio Surface Hopping Excited-State Molecular Dynamics Approach on the Basis of Spin–Orbit Coupled States: An Application to the A-Band Photodissociation of CH_3I. *J. Comput. Chem.* **2019**, *40*, 456–463.

(34) Cui, G.; Thiel, W. Generalized Trajectory Surface-Hopping Method for Internal Conversion and Intersystem Crossing. *J. Chem. Phys.* **2014**, *141*, 124101.

(35) Zhu, C.; Nakamura, H.; Re, N.; Aquilanti, V. The Two-State Linear Curve Crossing Problems Revisited. I. Analysis of Stokes Phenomenon and Expressions for Scattering Matrices. *J. Chem. Phys.* **1992**.

(36) Zhu, C.; Nakamura, H. The Two-state Linear Curve Crossing Problems Revisited. II. Analytical Approximations for the Stokes Constant and Scattering Matrix: The Landau–Zener Case. *J. Chem. Phys.* **1992**, *97*, 8497–8514.

(37) Zhu, C.; Nakamura, H. The Two-state Linear Curve Crossing Problems Revisited. III. Analytical Approximations for Stokes Constant and Scattering Matrix: Nonadiabatic Tunneling Case. *J. Chem. Phys.* **1993**, *98*, 6208–6222.

(38) Zhu, C.; Nakamura, H. Two-State Linear Curve Crossing Problems Revisited. IV. The Best Analytical Formulas for Scattering Matrices. *J. Chem. Phys.* **1994**.

(39) Yu, L.; Xu, C.; Lei, Y.; Zhu, C.; Wen, Z. Trajectory-Based Nonadiabatic Molecular Dynamics without Calculating Nonadiabatic Coupling in the Avoided Crossing Case: Trans↔cis Photoisomerization in Azobenzene. *Phys. Chem. Chem. Phys.* **2014**, *16*, 25883–25895.

(40) Xu, C.; Yu, L.; Zhu, C.; Yu, J. Photoisomerization Reaction Mechanisms of O-Nitrophenol Revealed by Analyzing Intersystem Crossing Network at the MRCI Level. *J. Phys. Chem. A* **2015**, *119*, 10441–10450.

(41) Xu, C.; Yu, L.; Zhu, C.; Yu, J.; Cao, Z. Intersystem Crossing-Branched Excited-State Intramolecular Proton Transfer for o-Nitrophenol: An Ab Initio on-the-Fly Nonadiabatic Molecular Dynamic Simulation. *Sci. Rep.* **2016**, *6*, 26768.

(42) Miller, W. H.; Handy, N. C.; Adams, J. E. Reaction Path Hamiltonian for Polyatomic Molecules. *J. Chem. Phys.* **1980**, *72*, 99–112.

(43) Kato, S.; Morokuma, K. Potential Energy Characteristics and Energy Partitioning in Chemical Reactions: Ab Initio MO Study of Four-centered Elimination Reaction $CH_3CH_2F \rightarrow CH_2{=}CH_2{+}HF$. *J. Chem. Phys.* **1980**, *73*, 3900–3914.

(44) Taketsugu, T.; Gordon, M. S. Dynamic Reaction Path Analysis Based on an Intrinsic Reaction Coordinate. *J. Chem. Phys.* **1995**, *103*, 10042–10049.

(45) Anderson, J. B. Statistical Theories of Chemical Reactions. Distributions in the Transition Region. *J. Chem. Phys.* **1973**, *58*, 4684–4692.

(46) Kraka, E.; Cremer, D. Computational Analysis of the Mechanism of Chemical Reactions in Terms of Reaction Phases: Hidden Intermediates and Hidden Transition States. *Acc. Chem. Res.* **2010**.

(47) Zou, W.; Sexton, T.; Kraka, E.; Freindorf, M.; Cremer, D. A New Method for Describing the Mechanism of a Chemical Reaction Based on the Unified Reaction Valley Approach. *J. Chem. Theory Comput.* **2016**, *12*, 650–663.

(48) Kraka, E.; Zou, W.; Tao, Y. Decoding Chemical Information from Vibrational Spectroscopy Data: Local Vibrational Mode Theory. *WIREs Comput. Mol. Sci.* **2020**, *10*.

(49) Valtazanos, P.; Ruedenberg, K. Bifurcations and Transition States. *Theor. Chim. Acta* **1986**, *69*, 281–307.

(50) Baker, J.; Gill, P. M. W. An Algorithm for the Location of Branching Points on Reaction Paths. *J. Comput. Chem.* **1988**, *9*, 465–475.

(51) Taketsugu, T.; Tajima, N.; Hirao, K. Approaches to Bifurcating Reaction Path. *J. Chem. Phys.* **1996**, *105*, 1933–1939.

(52) Yanai, T.; Taketsugu, T.; Hirao, K. Theoretical Study of Bifurcating Reaction Paths. *J. Chem. Phys.* **1997**, *107*, 1137–1146.

(53) Taketsugu, T.; Hirano, T. Bifurcation Analysis in Terms of Second-Order Jahn-Teller Effect. *J. Mol. Struct. THEOCHEM* **1994**, *310*, 169–176.

(54) Harabuchi, Y.; Nakayama, A.; Taketsugu, T. Trifurcation of the Reaction Pathway. *Comput. Theor. Chem.* **2012**, *1000*, 70–74.

(55) Harabuchi, Y.; Ono, Y.; Maeda, S.; Taketsugu, T. Analyses of Bifurcation of Reaction Pathways on a Global Reaction Route Map: A Case Study of Gold Cluster Au_5. *J. Chem. Phys.* **2015**, *143*, 014301.

(56) Hong, Y. J.; Tantillo, D. J. Biosynthetic Consequences of Multiple Sequential Post-Transition-State Bifurcations. *Nat. Chem.* **2014**, *6*, 104–111.

(57) Hare, S. R.; Li, A.; Tantillo, D. J. Post-Transition State Bifurcations Induce Dynamical Detours in Pummerer-like Reactions. *Chem. Sci.* **2018**, *9*, 8937–8945.

(58) Hare, S. R.; Tantillo, D. J. Cryptic Post-Transition State Bifurcations That Reduce the Efficiency of Lactone-Forming Rh-Carbenoid C–H Insertions. *Chem. Sci.* **2017**, *8*, 1442–1449.

(59) Tsutsumi, T.; Harabuchi, Y.; Ono, Y.; Maeda, S.; Taketsugu, T. Analyses of Trajectory On-the-Fly Based on the Global Reaction Route Map. *Phys. Chem. Chem. Phys.* **2018**, *20*, 1364–1372.

(60) Tsutsumi, T.; Ono, Y.; Arai, Z.; Taketsugu, T. Visualization of the Intrinsic Reaction Coordinate and Global Reaction Route Map by Classical

Multidimensional Scaling. *J. Chem. Theory Comput.* **2018**, *14*, 4263–4270.

(61) Tsutsumi, T.; Ono, Y.; Arai, Z.; Taketsugu, T. Visualization of the Dynamics Effect: Projection of on-the-Fly Trajectories to the Subspace Spanned by the Static Reaction Path Network. *J. Chem. Theory Comput.* **2020**, *16*, 4029–4037.

(62) Tsutsumi, T.; Harabuchi, Y.; Yamamoto, R.; Maeda, S.; Taketsugu, T. On-the-Fly Molecular Dynamics Study of the Excited-State Branching Reaction of α-Methyl-Cis-Stilbene. *Chem. Phys.* **2018**, *515*, 564–571.

Chapter 2

Analysis of On-the-fly Trajectory based on Reaction Route Network

2.1 Introduction

A chemical reaction is a set of elementary reaction processes, and, under the Born–Oppenheimer approximation, each elementary process is described as a route on the potential energy surface (PES). The intrinsic reaction coordinate (IRC) proposed by Fukui is a powerful tool to determine the elementary reaction path on the PES and is defined as a minimum energy pathway in mass-weighted coordinates, which connects two minima (MINs) *via* a transition state (TS).[1] The IRC path is a one-dimensional route on the multidimensional PES, and the variations of molecular geometries, potential energy, and molecular orbitals along the IRC provide an intuitive understanding of the elementary reaction process. In the last two decades, the global reaction route mapping (GRRM) strategy, one of the automated reaction path search approaches, has been developed and provides a concept of a reaction route network, which is composed of multiple IRC paths connecting each other.[2–5] Recently, various chemical reaction mechanisms are investigated and clarified by such static reaction path analyses.[6–11]

In actual chemical reactions, since a molecular system has kinetic energy, it will wander around the IRC path. The on-the-fly molecular dynamics (MD) is a full-dimensional classical trajectory method, which requires atomic forces obtained from the quantum chemical calculation, and provides a dynamical reaction path as a function of time. Therefore, it is employed as a standard tool to examine dynamics effects, such as the centrifugal forces and the reaction-path bifurcation. Indeed, the departures from the IRC due to centrifugal forces caused by the IRC curvature[12,13] and the bifurcation due to the IRC instability[14–19] have been reported in various chemical reactions. Recently, the subject of on-the-fly MD has been extended to photochemistry, and the ultrafast dynamics concerned with the excited state have been discussed with experimental results.[20–23]

Although the on-the-fly trajectory with all degrees of freedom is consistent with the reaction route tracing the molecular system on the PES, it is a hard task to clarify the driving force for the chemical reaction. From the viewpoint of dynamics, the IRC is regarded as the reaction path with infinitesimal velocities and is suitable for the reference path to discuss dynamical effects. Indeed, as shown in **Chapter 1**, many researchers have studied dynamics behaviors nearby the given IRC path.[12,24,25] However, the chemical reaction is composed of multiple elementary reaction paths, and thus the dynamical reaction behaviors should be analyzed based on the multi-IRCs and the IRC network.

In this chapter, I develop a method to analyze the on-the-fly trajectory based on a global reaction route map. This *on-the-fly trajectory mapping method* clarifies the dynamical reaction paths by mapping the trajectories onto the IRC network. As a demonstration, I apply the on-the-fly trajectory mapping method to the ground state reaction for the Au_5 cluster and attempt to uncover the dynamical reaction mechanisms.[26] Gold nanoclusters have attracted strong interest because of their ability for optical devices and catalysis and have been studied for various applications.[27–30] Very recently, the geometrical and optical features of small gold cluster Au_n (n = 2-13) were systematically reported by the DFT calculation.[29] Harabuchi and *et al.* reported a global reaction route map of Au_5 by the GRRM program and found several bifurcating paths with valley-ridge transition (VRT) points.[19] In this chapter, I also discuss the detailed mechanism of bifurcating reaction given by the on-the-fly trajectories.[26]

2.2 On-the-fly Trajectory Mapping Method

In order to map the on-the-fly trajectory onto the IRC network, first, I have to introduce a molecular similarity. There are several molecular dissimilarities (or similarities) in biochemistry and chemoinformatics, such as the root mean square deviation (RMSD) and the Tanimoto coefficient[31], but I choose a simple definition, the Euclid distance (linear distance) in mass-weighted Cartesian coordinates. Here, I introduce the mass-weighted linear distance between two molecules (isomers), the nuclear permutation-inversion isomer, and the procedure of the on-the-fly trajectory mapping method. This method is implemented in the SPPR program[32] developed in our laboratory, and I am a member of the major developers.

2.2.1 Linear Distance in Mass-weighted Cartesian Coordinate

Let $\mathbf{x}_i = (x_1, y_1, z_1, \cdots, x_N)$ be a 3*N*-dimensional Cartesian coordinate for an *N* atomic system and $\boldsymbol{\xi} = (\xi_1, \cdots, \xi_{3N}) = (\sqrt{m_1} x_1, \cdots, \sqrt{m_N} z_N)$ be a mass-weighted Cartesian coordinate where m_i is the *i*th atomic mass. The mass-weighted linear distance between molecule *i* and *j* is defined as

$$d_{ij} = \sqrt{\sum_{k}^{3N} \left(\xi_k^{(i)} - \xi_k^{(j)}\right)^2} = \left|\boldsymbol{\xi}^{(i)} - \boldsymbol{\xi}^{(j)}\right|. \qquad (2\text{-}1)$$

For the smallest distance between molecule *i* and *j*, one needs to align them to remove (reduce) the translational and rotational degrees of freedom. The former is precisely removed by setting each center of mass to the origin of the coordinate system. The latter is reduced by determining the best orientation of x-y-z axes so as to minimize d_{ij} by the Kabsch algorithm[33,34], which is one of the best-fit algorithms proposed in biochemistry[35,36]. The Kabsch algorithm for **P** and **Q** in the Cartesian coordinate, where each centroid is translated to the origin of coordinate, gives an optimal rotation matrix **U** such that **P** overlaps **Q** as much as possible by the singular value decomposition as follow:

$$\mathbf{P}^T\mathbf{Q} = \mathbf{V}\mathbf{S}\mathbf{W}^T \qquad (2\text{-}2)$$

where **V** and **W** are orthogonal matrices and **S** is a diagonal matrix. The left-hand side, $\mathbf{P}^T\mathbf{Q}$, corresponds to a covariance matrix. Then, the rotation matrix **U** is defined as

$$\mathbf{U} = \mathbf{V}\begin{pmatrix} 1 & 0 & 0 \\ 0 & 1 & 0 \\ 0 & 0 & d \end{pmatrix}\mathbf{W}^T \qquad (2\text{-}3)$$

where $d = \det(\mathbf{U}) = \det(\mathbf{V})\det(\mathbf{W}^T) = \pm 1$. Note that when **P** and **Q** are mass-weighted Cartesian coordinates, one needs to perform the singular value decomposition for a weighted covariance matrix.

2.2.2 Nuclear Permutation-Inversion Isomer

Another problem in estimating a proper molecular dissimilarity comes from nuclear permutation-inversion (NPI) isomers. The NPI isomer is generated by the permutation of identical nuclei and the spatial inversion operation, and its molecular shape and chemical properties are exactly consistent with other isomers. However, the molecular dissimilarity, such as RMSD and Euclid distance, between these isomers does not become 0 due to the different atom mapping. In addition, the NPI isomerization reactions are represented by IRCs connecting the original atom-mapping structure and the NPI isomers, suggesting that the reaction barrier at the transition state determines the more favorable NPI isomer to arise. Since the GRRM program distinguishes respective structures by a set of interatomic distances, the NPI isomers are merged into a representative structure in the reaction route map. On the other hand, in the on-the-fly MD simulation, the molecule easily changes to other NPI isomers by kinetic energy. Therefore, one should appropriately handle the NPI isomers to estimates the molecular dissimilarity connected with the reaction route map and the on-the-fly trajectory.

In the SPPR program, I implement the option handling NPI isomers, *merged-NPI* option, and it determines the distance between a molecule i and j as follows:

1) Generate NPI isomers from a molecule j.
2) Calculate mass-weighted linear distances between a molecule i and each NPI isomer.
3) Determine d_{ij} as the smallest distance among them.

This procedure is summarized in **Figure 2.1**. By using the *merged-NPI* option, one can always get the optimal distance without a unique atom mapping. Several molecular dissimilarities without a unique atom mapping have been proposed in structural biology.[37–39] For example, Satoh, Iwata, and coworkers, by the matching algorithms, were proposed a generalized RMDS (G-RMDS) restricted not to the size of a molecular system and not to the unique atom mapping.[37]

1) Generate NPI isomers from a molecule j

2) Calculate mass-weighted Cartesian distances [Å amu$^{1/2}$]

$$d_{i,\,j\text{-NPI}} = \{d_{i,\,j\text{-NPI}'}, \ldots, d_{i,\,j\text{-NPI}''}, \ldots\} = \{57.6, \ldots, 3.5, \ldots\}$$

3) Determine the smallest distance $d_{ij} = \min(\mathrm{d}_{i,\,j\text{-NPI}}) = 3.5$

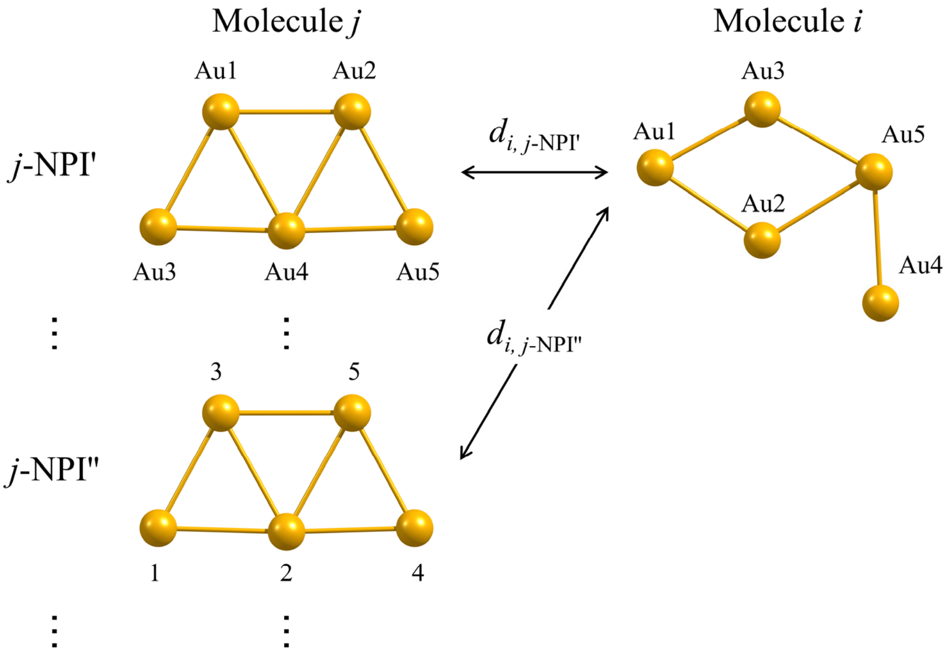
Molecule j
Molecule i
j-NPI'
Au1
Au2
Au3
Au4
Au5
$d_{i,\,j\text{-NPI}'}$
Au3
Au1
Au5
Au2
Au4
$d_{i,\,j\text{-NPI}''}$
3
5
j-NPI''
1
2
4

Figure 2.1. A scheme for calculating the mass-weighted linear distance between a molecule i and a molecule j with the *merged-NPI* option by the SPPR program.

2.2.3 On-the-fly Trajectory Mapping Procedure

Let $\xi^{\mathrm{trj}}(t)$ and $\xi^{(i)}$ be mass-weighted Cartesian coordinates of the on-the-fly trajectory at time t and ith reference structure, respectively. Here, I introduce a distance function $d(t)=\left(d_1(t),\cdots,d_i(t),\cdots d_n(t)\right)$ for n reference structures, where $d_i(t)$ is a mass-weighted linear distance:

$$d_i(t)=\sqrt{\sum_{k}^{3N}\left(\xi_k^{\mathrm{trj}}(t)-\xi_k^{(i)}\right)^2}=\left|\xi^{\mathrm{trj}}(t)-\xi^{(i)}\right|. \qquad (2\text{-}4)$$

The key idea of the on-the-fly trajectory mapping is to assign the trajectory at time t to the closest reference structure on the PES by using the distance function, as the following procedure:

1) Select the reference structures from the PES.
2) At time t, calculate the distance function between $\xi^{\mathrm{trj}}(t)$ and each reference structure.
3) Determine the closest reference structure that gives the smallest distance and assign $\xi^{\mathrm{trj}}(t)$ to it.
4) If the on-the-fly trajectory does not terminate, proceed to the next step $t \leftarrow t+\Delta t$ and return to 2).

Note that the reference structures and the on-the-fly trajectory should be calculated at the same computational level. **Figure 2.2a** shows a schematic picture of an on-the-fly trajectory that runs over a reaction route map. In this situation, I select MIN1, MIN2, TS1, and TS2 as reference structures and then achieve the distance function along the trajectory as shown in Figure 2.2b. Then, by focusing on the closest reference structures, I can uncover the dynamical reaction process: the molecule jumps from the IRC connecting TS1 and MIN1 to the other IRC connecting TS2 and MIN2.

Since the proposed method characterizes the dynamical reaction routes based on the subspace of PES determined by the reference structures, the choice of the reference structures is critical to describe the target chemical reactions properly. For example, when only MINs are chosen from the global reaction route map, one can verify hopping behaviors from one potential well to another well. Also, when a set of structures along multi-IRCs are chosen, one can investigate dynamical reaction processes deviating from one IRC to another IRC during the structural transformations.

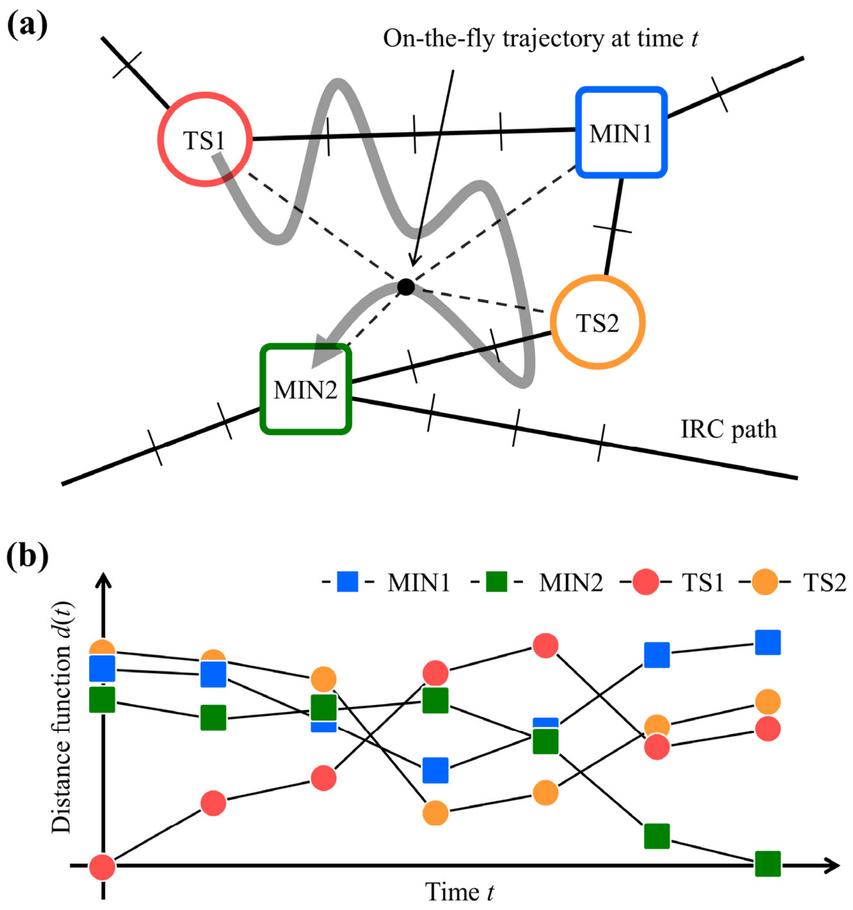
(a)
On-the-fly trajectory at time *t*
TS1
MIN1
TS2
MIN2
IRC path
(b)
MIN1
MIN2
TS1
TS2
Distance function *d*(*t*)
Time *t*

Figure 2.2. (a) A two-dimensional schematic picture of an on-the-fly trajectory that runs over a reaction route map. (b) A variation of a distance function with four reference structures (MIN1, MIN2, TS1, and TS2) as a function of time *t*. The MIN1, MIN2, TS1, and TS2 are denoted as blue circles, green circles, red squares, and orange squares, respectively.

2.3 Results and Discussion

2.3.1 Global Reaction Route Network of Au_5 Cluster

Harabuchi *et al.* recently reported a global reaction route map of Au_5,[19] which is generated by the GRRM program (developmental version) based on the DFT calculation with Perdew-Burke-Ernzerhof (PBE) functionals and LanL2DZ basis sets using Gaussian09[40]. In this study, I reuse this global reaction route map. **Figure 2.3** shows the global reaction route map where five MINs (MIN*i*, *i* = 1~5) are connected *via* 14 TSs (TS*i*-*j* that connects MIN*i* and MIN*j*), and MINs, TSs, and IRCs are denoted by red squares, blue circles, and black solid lines. Among 14 TSs, seven TSs are categorized as TS*i*-*i* connecting two NPI isomers of MIN*i*, which are illustrated by a double line between MIN*i* and TS*i*-*i*. The global minimum, MIN1, is linked with nine TSs: four TS*i*-*i* (TS1-1a, TS1-1b, TS1-1c, TS1-1d) and five TS*i*-*j* (TS1-2, TS1-3a, TS1-3b, TS1-4, TS1-5). Note that the TSs that connect the same pair of MIN*i* and MIN*j* are distinguished by letters (a, b, c, and d) in order of decreasing energy. As shown in Figure 2.3, most MINs and TSs have a planar geometry due to a relativistic effect of gold atoms,[28] and only MIN4, TS1-1d, TS1-4, TS4-4, and TS5-5 have a non-planar geometry.

The valley-ridge transition (VRT) point corresponds to the bifurcation point where a valley nature along the IRC branches into two valleys.[41–44] Of course, the IRC path itself does not allow bifurcating on the way, and the bifurcation reaction is promoted by the dynamics effects. Harabuchi *et al.* also reported five VRT points on the global reaction route map of Au_5 and discovered that a TS connecting between a product and a branching product, which is very similar to a VRT point, exists near the VRT point. In the Au_5 case, they verified that VRT1, VRT2, VRT3, VRT4, and VRT5 correspond to TS1-

1b, TS1-1c, TS5-5, TS3-3, and TS3-3, respectively.[19] To investigate bifurcation mechanisms by the on-the-fly mapping method, in this chapter, I focus on VRT1 existing on the IRC connecting from TS1-1d to MIN1, which is denoted as a black square in Figure 2.3.

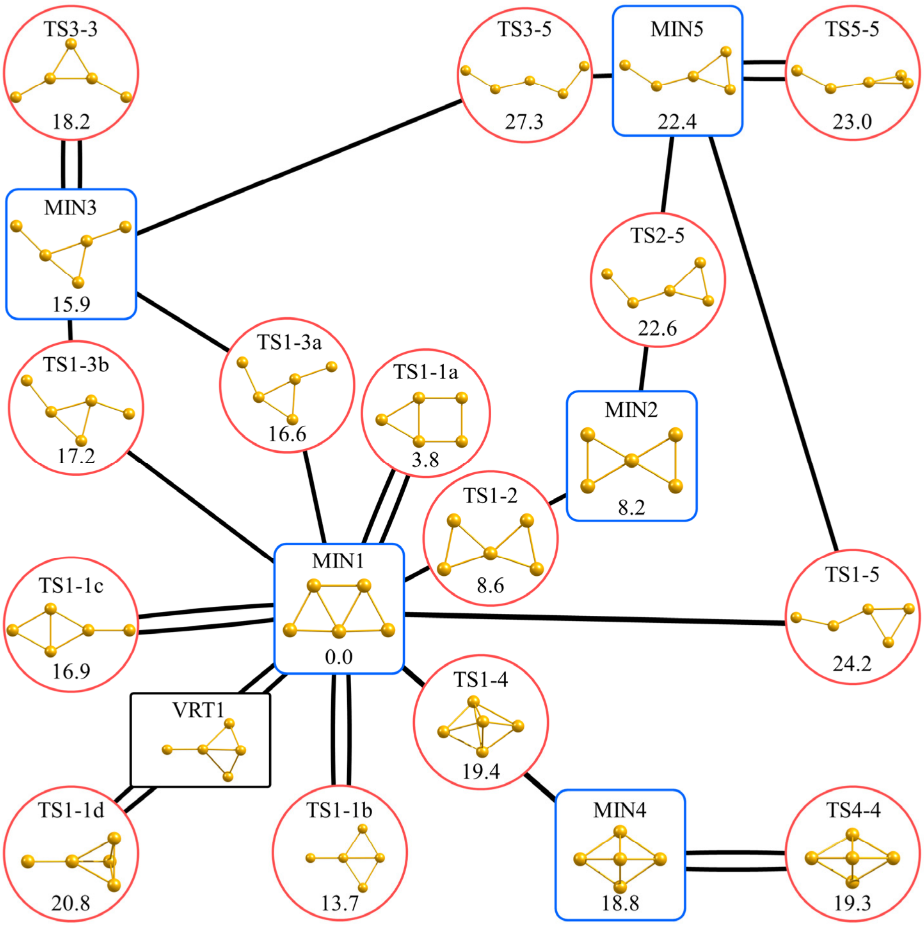
TS3-3
18.2
TS3-5
27.3
MIN5
22.4
TS5-5
23.0
MIN3
15.9
TS2-5
22.6
TS1-3b
17.2
TS1-3a
16.6
TS1-1a
3.8
MIN2
8.2
TS1-2
8.6
MIN1
0.0
TS1-1c
16.9
TS1-5
24.2
VRT1
TS1-4
19.4
TS1-1d
20.8
TS1-1b
13.7
MIN4
18.8
TS4-4
19.3

Figure 2.3. The global reaction route map of Au_5 in the previous study[19], where the IRC paths (solid lines) link five MINs (blue squares) and 14 TSs (red circles). The molecular structure and relative energy (in kcal/mol) are given. The valley-ridge transition (VRT) point on the IRC linking TS1-1d and MIN1 is also shown as a black square.

As mentioned above, the global reaction route map does not distinguish NPI isomers. For the Au_5 cluster, the maximum number of NPI isomers is 240 (= 2 × 5!). Because of the molecular symmetry, the number of isomers is reduced to; 120 for C_s and C_2 structures (MIN3, MIN5, TS1-1d, TS1-3a, TS1-3b, TS1-5, TS2-5, TS3-3, TS3-5, TS5-5), 60 for C_{2v} structures (MIN1, MIN4, TS1-1a, TS1-1b, TS1-1c, TS1-2, TS4-4), and 30 for D_{2h} structure (MIN2). The remaining molecules, TS1-4 and VRT1, belong to C_1 symmetry and then have 240 NPI isomers. The relative energies, the point groups, and the number of NPI isomers for 20 structures (five MINs, 14 TSs, and VRT1) are summarized in **Table 2.1**.

Table 2.1. The relative energies (in kcal/mol), point groups, and the number of NPI isomers for five MINs, 14 TSs, and VRT1.

		Energy	# of NPIs			Energy	# of NPIs
MIN1	C_{2v}	0.0	60	TS1-3a	C_s	16.6	120
MIN2	D_{2h}	8.2	30	TS1-3b	C_s	17.2	120
MIN3	C_s	15.9	120	TS1-4	C_1	19.4	240
MIN4	C_{2v}	18.8	60	TS1-5	C_s	24.2	120
MIN5	C_s	22.4	120	TS2-5	C_s	22.6	120
TS1-1a	C_{2v}	3.8	60	TS3-3	C_2	18.2	120
TS1-1b	C_{2v}	13.7	60	TS3-5	C_s	27.3	120
TS1-1c	C_{2v}	16.9	60	TS4-4	C_{2v}	19.3	60
TS1-1d	C_s	20.8	120	TS5-5	C_s	23.0	120
TS1-2	C_{2v}	8.6	60	VRT1	C_1	17.6	240

Again, MIN1 is linked with four TS*i*-*i* (TS1-1a, TS1-1b, TS1-1c, TS1-1d). These TSs connect the respective NPI isomers of MIN1 in a configuration space, and actually, the molecule can proceed to other NPI isomers crossing over their activation barriers: TS1-1a (3.8 kcal/mol), TS1-1b (13.7 kcal/mol), TS1-1c (16.9 kcal/mol), and TS1-1d (20.8 kcal/mol). **Figure 2.4** shows the NPI isomers connected by the respective TSs, which are named the *closed island* of NPI isomers. In Figure 2.4, the NPI isomers of MIN1 (denoted by blue squares) are connected by the IRCs (black lines) *via* the NPI isomers of respective TSs (red circles), and the molecular structures of NPI isomers of MIN1 and the representative TSs are shown. As shown in Figure 2.4a, five NPI isomers are linked through a structural transformation *via* TS1-1a, which indicates that 60 NPI isomers of MIN1 are divided into 12 closed islands (60/5 = 12). In the same way, four, six, and two NPI isomers are linked through TS1-b (in Figure 2.4b), TS1-1c (in Figure 2.4c), and TS1-1d (in Figure 2.4d), respectively, and then there are 15, 10, and 30 closed islands by the respective TSs. Note that six NPI isomers linked by TS1-1c include two NPI isomers by TS1-1d. Consequently, 60 NPI isomers of MIN1 are completely linked by four sets of TSs: (TS1-1a and TS1-1b), (TS1-1a and TS1-1c), (TS1-1a and TS1-1d) and (TS1-1b and TS1-1c). Also, only 12 NPI isomers are linked by a set of (TS1-1b and TS1-1d).

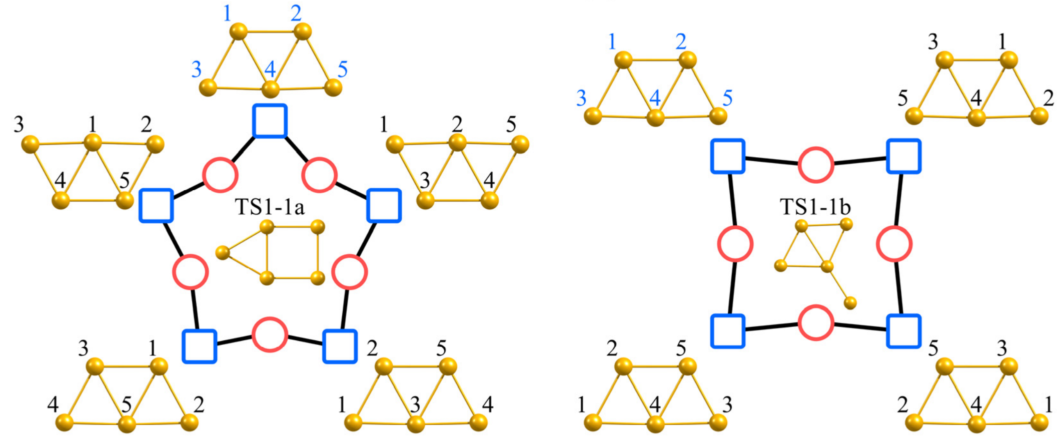

(a) Closed island of TS1-1a

(b) Closed island of TS1-1b

TS1-1a
1 2
3 4 5
3 1 2
4 5
1 2 5
3 4
3 1
4 5 2
2 5
1 3 4
TS1-1b
1 2
3 4 5
3 1
5 4 2
2 5
1 4 3
5 3
2 4 1

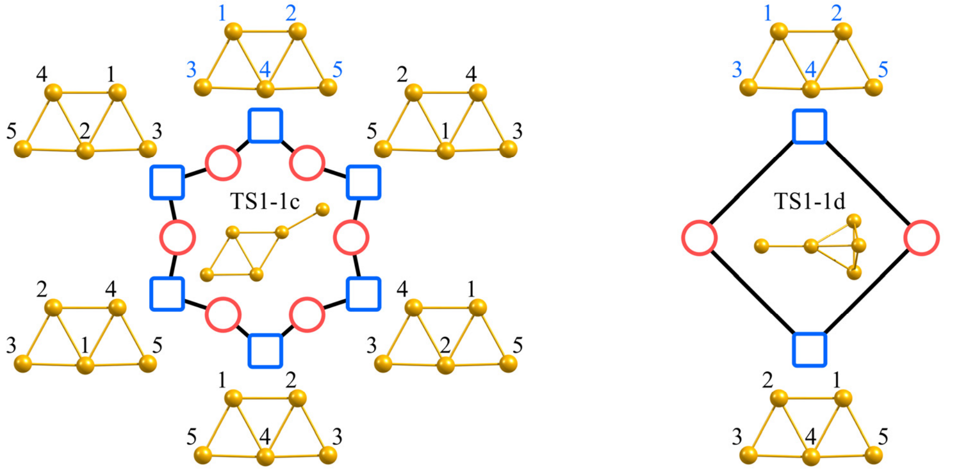

(c) Closed island of TS1-1c

(d) Closed island of TS1-1d

TS1-1c
1 2
3 4 5
4 1
5 2 3
2 4
5 1 3
2 4
3 1 5
4 1
3 2 5
1 2
5 4 3
TS1-1d
1 2
3 4 5
2 1
3 4 5

Figure 2.4. The closed island for NPI isomers of MIN1 connected *via* (a) TS1-1a (the activation barrier with 3.8 kcal/mol), (b) TS1-1b (13.7 kcal/mol), (c) TS1-1c (16.9 kcal/mol), and (d) TS1-1d (20.8 kcal/mol). The NPI isomers of MIN1 (denoted by blue squares) are connected by the IRCs (black lines) *via* the NPI isomers of respective TSs (red circles) in each closed island. The molecular structures of NPI isomers of MIN1 and the representative TSs are also given.

2.3.2 On-the-fly Molecular Dynamics Simulation

The on-the-fly MD trajectories were run from TS1-1d at the PBE/LanL2DZ level using the SPPR program[32]. The initial coordinate was fixed at TS1-1d, and the initial velocity with 5 kcal/mol as kinetic energy was determined randomly in terms of $3N-6$ normal modes (N denotes the total number of atoms). The time step was set to 5 fs, which is determined through preliminary calculations by checking the total energy conservation, and 200 trajectories were run over 3 ps. All electronic structure calculations were performed by the Gaussian09 program[40].

2.3.3 Bifurcation Mechanisms: A Case of TS1-1d

To discuss the bifurcating reaction through the IRC connecting TS1-1d and MIN1, I construct the partial reaction route map for the bifurcation related to TS1-1d. TS1-1d is composed of a pyramidal part of Au_4, which has an isosceles triangle with C_s symmetry on the bottom, and an attached Au atom. Hence, three different TS1-1d with isosceles triangles, in other words, three NPI isomers of TS1-1d, exist around an equilateral triangle with C_{3v} symmetry in the configuration space. Note that the pseudo-TS1-1d with C_{3v} symmetry is a conical intersection between the ground- and the first excited-states. Since each TS1-1d connects two NPI isomers of MIN1, as shown in Figure 2.4d, six NPI isomers of MIN1 are connected by three TS1-1d. **Figure 2.5** shows a schematic reaction route map related to three TS1-1d and six MIN1. The six MIN1 are also linked by three TS1-1b: MIN1 and MIN1", MIN1' and MIN1''', and MIN1'''' and MIN1''''' are linked by TS1-1b, TS1-1b', and TS1-1b", respectively. As mentioned above, such three TS1-1b are located near six NPI isomers of VRT1.[19] Note that the initial structure in the on-the-fly MD simulation is TS1-1d defined in Figure 2.5.

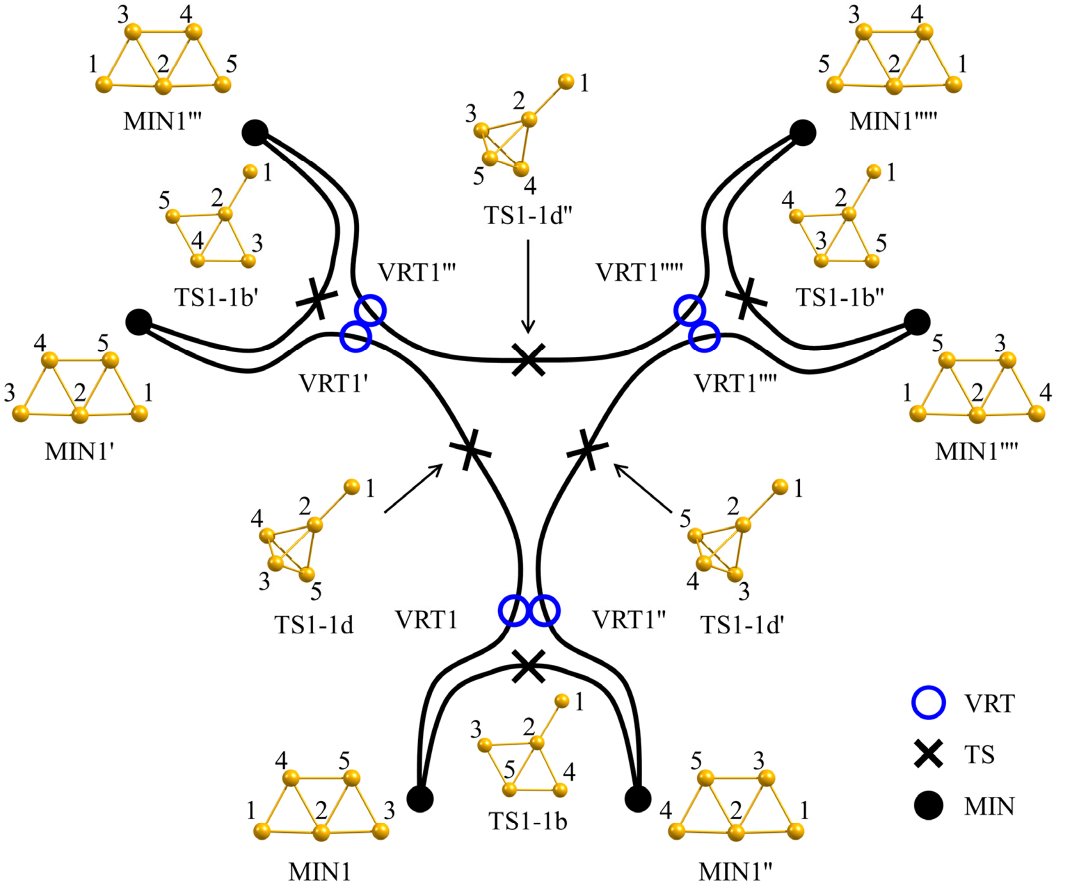
MIN1'''
TS1-1d''
MIN1'''''
TS1-1b'
VRT1'''
VRT1'''''
TS1-1b''
VRT1'
VRT1''''
MIN1'
MIN1''''
TS1-1d
VRT1
VRT1''
TS1-1d'
TS1-1b
MIN1
MIN1''
VRT
TS
MIN

Figure 2.5. A schematic reaction route map for bifurcating paths including three TS1-1d (denoted by cross marks), six MIN1 (denoted by black circles), three TS1-1b (denoted by cross marks), and six VRT1 (denoted by blue circles).

Here, I analyze the on-the-fly trajectory based on the distance function $d_i(t)$ in equation (2-4). In order to discuss the bifurcation for Au_5, the reference structures are defined as 2130 NPI isomers for 20 molecular structures (five MINs, 14 TSs, and VRT1 summarized in Table 2.1), and the on-the-fly trajectory mapping method is employed without the merged-NPI option. Because the distance function plots without the merged-NPI option are too complicated to grasp dynamical reaction processes, I attempt to discuss reaction processes by using the schematic reaction route map of Figure 2.5.

As shown in Figure 2.5, three TS1-1d (TS1-1d, TS1-1d', and TS1-1d'') are located very close to each other in the configuration space. Hence, some trajectories possibly jump to other IRCs immediately, proceeding to not only MIN1 or MIN1', but also other NPI isomers of MIN1. Such a jump-like behavior from one IRC to another IRC can realize only through a dynamics simulation, which can not be recognized by a static reaction path analysis. Indeed, some trajectories show one or more hopping over TS1-1d, TS1-1d', and TS1-1d'' in the early simulation time. This behavior driven by the dynamics effects is named "*IRC-jump*" in this thesis. According to the number of the initial hoppings, the trajectories are classified into five cases: (A) no hopping (96 trajectories), (B) one hopping (74 trajectories), (C) two hopping (23 trajectories), (D) three hopping (6 trajectories), and (E) four hopping (1 trajectory). As a result, it is revealed that almost half trajectories (96/200) go along the IRC without hopping, while the remaining trajectories (104/200) stay in the region related to three TS1-1d before going down.

Figure 2.6 shows schematic pictures for initial dynamical processes from TS1-1d to VRT1: (A) no hopping (96/200) and (B) one hopping (74/200), where three TS1-1d and six VRT1 are arranged in the same way as Figure 2.5. Henceforth, to simplify the discussion, I define three types of VRT1: $VRT1_{IRC}$ is directly linked with TS1-1d staying after the end of hoppings, VRT1$_{\mathrm{bifur}}$ is located on the IRC next to that with VRT1$_{\mathrm{IRC}}$, and VRT1$_{\mathrm{other}}$ is VRT1 excluding VRT1$_{\mathrm{IRC}}$ and VRT1$_{\mathrm{bifur}}$. In Figure 2.6, the red, blue, and green arrows indicate the reaction routes from the respective TS1-1d toward VRT1$_{\mathrm{IRC}}$, VRT1$_{\mathrm{bifur}}$, and VRT1$_{\mathrm{other}}$. In the case of (A), most trajectories proceed to VRT1$_{\mathrm{IRC}}$ (A1: 86/96), while a few trajectories proceed to VRT1$_{\mathrm{bifur}}$ (A2: 7/96). Such behavior is the well-known bifurcation reaction, indicating that the molecule jumps from the near VRT region on the IRC to the next IRC while descending on the PES. Also, only one trajectory proceeds to VRT1$_{\mathrm{other}}$ (A3: 1/96). Exceptionally, the other two trajectories directly proceed to MIN3 and TS1-4 without through VRT1 (A4: 1/96 and A5: 1/96). In the case of (B), the trajectories initially hop from TS1-1d to TS1-1d' (37/74) or TS1-1d'' (37/74), which are regarded as the IRC-jump behaviors. After hopping to TS1-1d', most trajectories descend toward VRT1'' (26/37) while only two trajectories go toward VRT1'''' (2/37). Similarly, after hopping to TS1-1d'', most trajectories descend toward VRT1''' (26/37) while eight trajectories go toward VRT1''''' (8/37). Such bias to VRT1'' and VRT1''' can be intuitively described by the fact that these trajectories are already descending toward VRT1 and VRT1' before hopping. As a result, in this case, 62 trajectories proceed to VRT1$_{\mathrm{IRC}}$ (B1: 62/74), and several trajectories proceed to VRT1$_{\mathrm{bifur}}$ (B2: 11/74) and VRT1$_{\mathrm{other}}$ (B1: 1/74). In summary, the on-the-fly trajectory mapping uncovers the dynamical reaction processes (A2 and most of B1) that proceed to the bifurcating products that correspond to two minima linking from VRT1'' and VRT1''', respectively. Thus, the proposed method reveals not only the conventional bifurcation processes that occur at the VRT point on the IRC (A2) but also the non-trivial bifurcation processes accompanying the IRC-jumps before reaching the VRT region (most of B1).

(A) No hopping (96/200 trajectories)

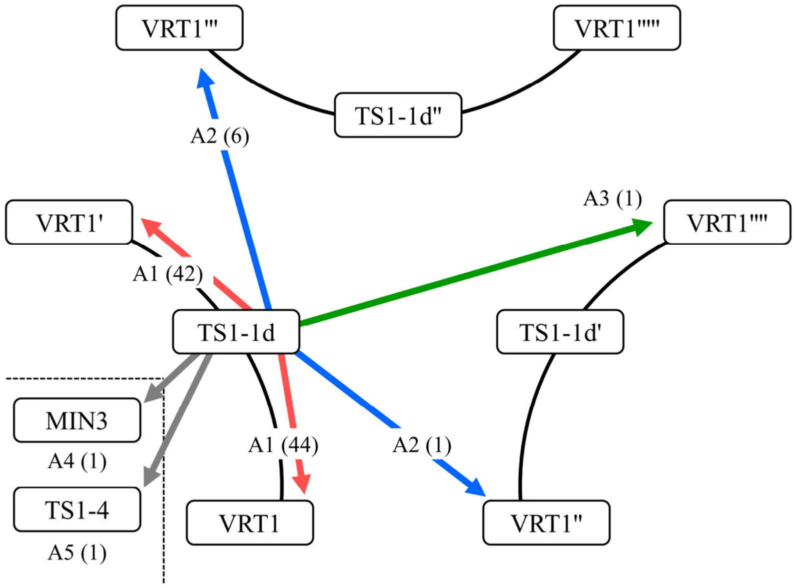
VRT1'''
VRT1'''''
TS1-1d''
A2 (6)
A3 (1)
VRT1'
VRT1''''
A1 (42)
TS1-1d
TS1-1d'
MIN3
A4 (1)
A1 (44)
A2 (1)
TS1-4
VRT1
VRT1''
A5 (1)

(B) One hopping (74/200 trajectories)

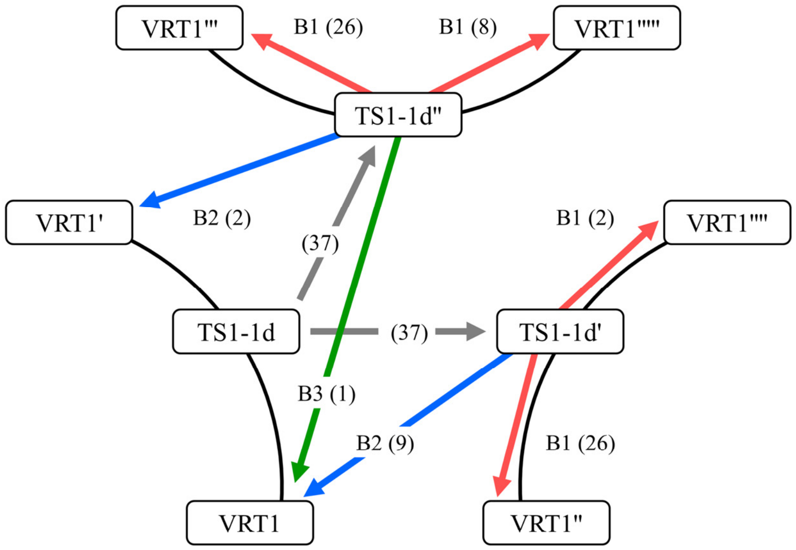
VRT1'''
B1 (26)
B1 (8)
VRT1'''''
TS1-1d''
VRT1'
B2 (2)
(37)
B1 (2)
VRT1''''
TS1-1d
(37)
TS1-1d'
B3 (1)
B2 (9)
B1 (26)
VRT1
VRT1''

Figure 2.6. Schematic pictures for initial dynamical processes from TS1-1d to VRT1: (A) no hopping (96/200) and (B) one hopping (74/200), where three TS1-1d and six VRT1 are arranged in the same way as Figure 2.5. The red, blue, and green arrows indicate the reaction routes from the respective TS1-1d toward $\mathrm{VRT1_{IRC}}$, $\mathrm{VRT1_{bifur}}$, and $\mathrm{VRT1_{other}}$. The number of trajectories is also shown in parentheses.

Figure 2.7 shows a dendrogram of 200 trajectories from TS1-1d until reaching VRT1, where TS1-1d(*n*) denotes TS1-1d after the *n*th hopping over TS1-1d, TS1-1d', and TS1-1d''. The number of trajectories and the averaged time to reach VRT1 are also shown. In total, 175 trajectories reach $\mathrm{VRT1_{IRC}}$, 21 trajectories reach $\mathrm{VRT1_{bifur}}$, and two trajectories reach $\mathrm{VRT1_{other}}$, and thus, the branching ratio for $\mathrm{VRT1_{bifur}}/\mathrm{VRT1_{IRC}}$ is 21/175 (~0.12). As the number of hopping increases, the averaged time to reach $\mathrm{VRT1_{IRC}}$ also increases as 342 fs (no hopping), 453 fs (n = 1), 583 fs (n = 2), 1055 fs (n = 3), and 1245 fs (n = 4). Interestingly, in no hopping and one hopping cases, the trajectories reach $\mathrm{VRT1_{bifur}}$ and $\mathrm{VRT1_{other}}$ faster than $\mathrm{VRT1_{IRC}}$ on average.

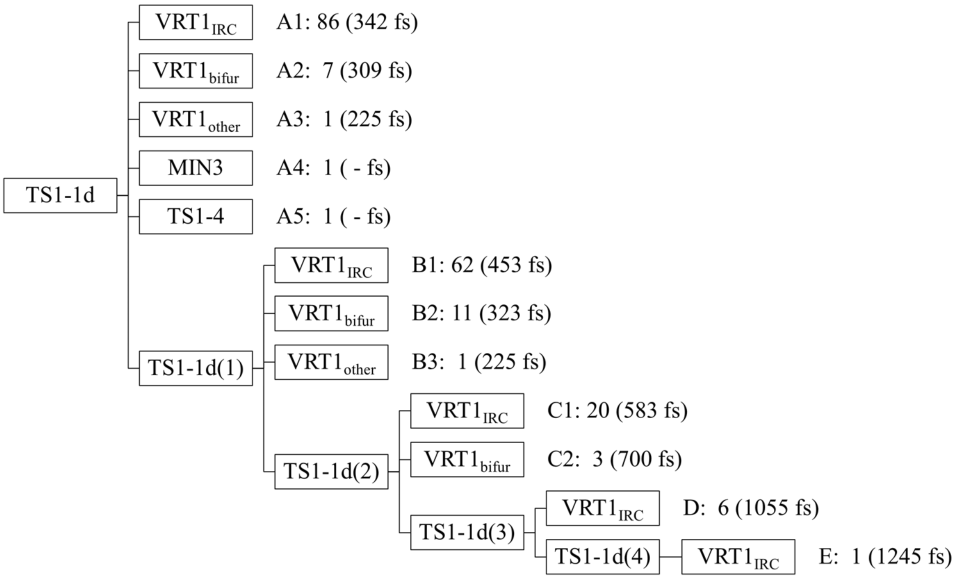
TS1-1d
VRT1IRC
A1: 86 (342 fs)
VRT1bifur
A2: 7 (309 fs)
VRT1other
A3: 1 (225 fs)
MIN3
A4: 1 (- fs)
TS1-4
A5: 1 (- fs)
TS1-1d(1)
VRT1IRC
B1: 62 (453 fs)
VRT1bifur
B2: 11 (323 fs)
VRT1other
B3: 1 (225 fs)
TS1-1d(2)
VRT1IRC
C1: 20 (583 fs)
VRT1bifur
C2: 3 (700 fs)
TS1-1d(3)
VRT1IRC
D: 6 (1055 fs)
TS1-1d(4)
VRT1IRC
E: 1 (1245 fs)

Figure 2.7. A dendrogram of 200 trajectories that start from TS1-1d and reach VRT1 where TS1-1d(*n*) denotes TS1-1d after the *n*th hopping over TS1-1d, TS1-1d', and TS1-1d''. The labels indicate (A) no hopping, (B) one hopping, (C) two hoppings, (D) three hoppings, and (E) four hoppings. For the respective routes, the number of trajectories and the average time to reach VRT1 are shown.

2.3.4 Isomerization Reaction Mechanisms with Dynamics Effects

Let’s move to discussions on the on-the-fly trajectories over 3 ps. In order to discuss the isomerization reaction based on the global reaction route map, distance functions with 2130 reference structures are calculated for 601 points of each trajectory (every 5 fs over 3 ps) with the merged-NPI option and then are plotted as a function of time. **Figure 2.8** shows six patterns of variations of distance functions along the on-the-fly trajectory. In all cases, because all trajectories start from TS1-1d, a distance from TS1-1d is zero at $t = 0$ fs. Remember that the on-the-fly trajectory mapping method assigns a series of the closest reference structures as the dynamical reaction routes.

Figure 2.8a shows that the trajectory descends on the PES along the IRC and reaches VRT1 at $t \sim 500$ fs. Then, this trajectory proceeds to TS1-1b, which is located near VRT1 as mentioned above, and succeedingly reaches MIN1 at $t \sim 1200$ fs. This is the most typical route, which is observed in 86 trajectories. After that, this trajectory shows continuous structural transformations among the NPI isomers of MIN1 *via* TS1-1a with the lowest barrier height (3.8 kcal/mol). Figure 2.8b indicates the trajectory following a similar route as Figure 2.8a, but, after passing through MIN1, it reaches MIN2 at $t \sim 2500$ fs *via* TS1-2. Although MIN2 is the second-lowest energy MIN, only five trajectories reach it. Among 200 trajectories, the number of trajectories reaching MINn within 3 ps is 192 ($n = 1$), 5 ($n = 2$), 1 ($n = 3$), 0 ($n = 4$), and 0 ($n = 5$). In Figure 2.8c, the trajectory proceeds to the non-planar structure and attempts to go over TS1-4 twice, but it does not reach MIN4 due to the relatively high activation barrier of TS1-4 (19.4 kcal/mol). In Figure 2.8d, the trajectory wanders around TS1-1d with four hoppings over TS1-1d, TS1-1d', and TS1-1d''. Then, it reaches the NPI isomer of TS1-1d except for TS1-1d, TS1-1d', and TS1-1d'' (referred to as TS1-1d$_{\mathrm{outside}}$) after passing through VRT1 and

TS1-1b (denoted as VRT1/TS1-1b), and finally, it does not reach MIN1 during 3 ps. Figure 2.8e and f show very rare trajectories that approach MIN3 and TS1-4 from TS1-1d directly (not *via* VRT1/TS1-1b), which correspond to A4 and A5 in Figure 2.7, respectively.

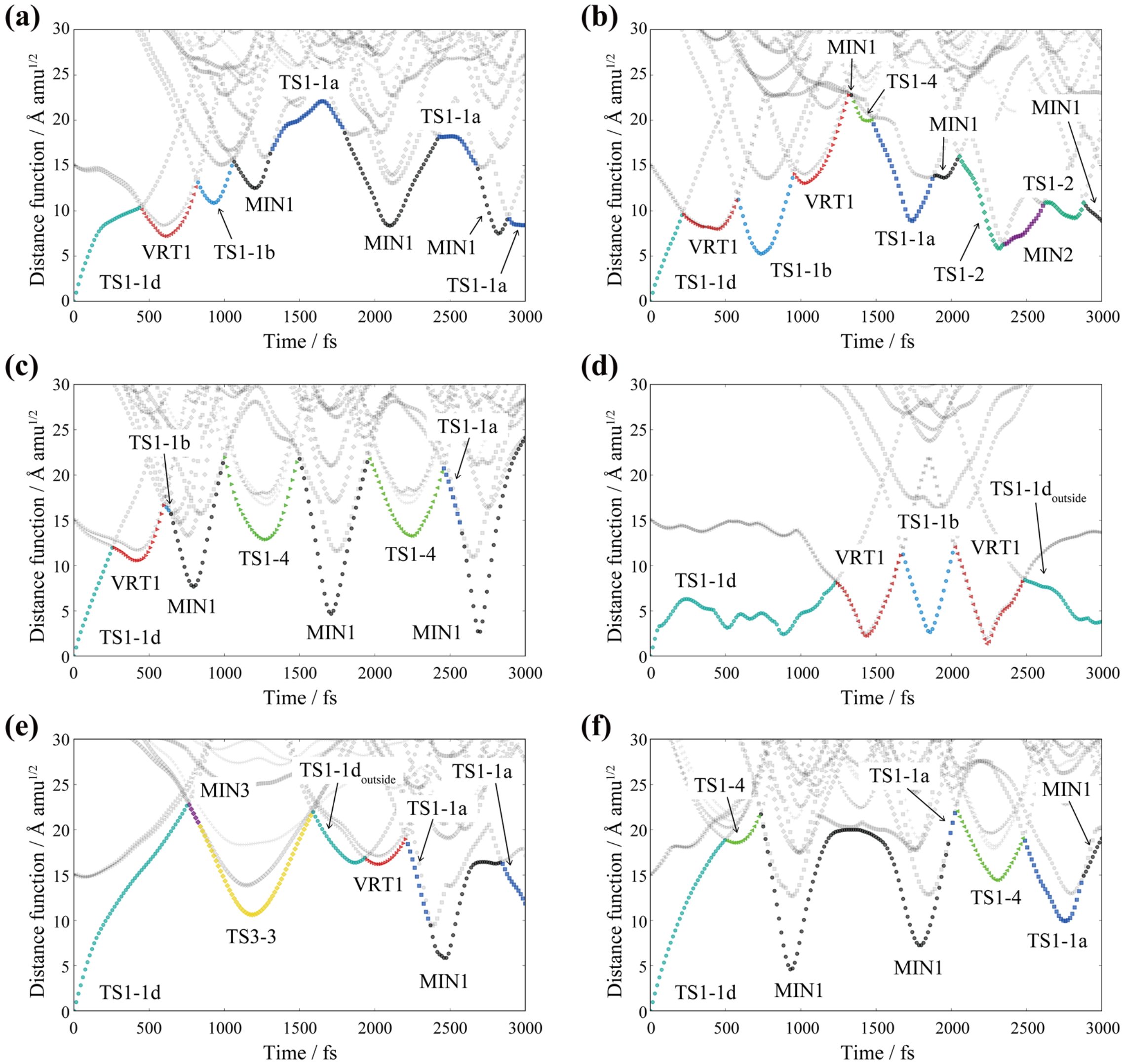

Figure 2.8. Variations of distance functions with reference structures as a function of time. (a) the trajectory proceeds to directly MIN1 along the IRC, and then it continues to transform among the NPI isomers of MIN1 *via* TS1-1a. (b) the trajectory reaches MIN2 *via* TS1-2 after passing through MIN1. (c) the trajectory transforms to the non-planar structure of TS1-4. (d) the trajectory wanders around TS1-1d, and then, it reaches the NPI isomer of TS1-1d except for TS1-1d, TS1-1d', and TS1-1d'' (referred to as TS1-1d$_{outside}$). (e) and (f) rare trajectories approach MIN3 and TS1-4 from TS1-1d directly, which correspond to A4 and A5 in Figure 2.7, respectively.

Figure 2.9 shows a schematic picture of the on-the-fly trajectory routes from TS1-1d to MIN1 *via* VRT1/TS1-1b. Here, the dynamical reaction routes of 198 trajectories are illustrated, while two trajectories do not go through VRT1/TS1-1b as discussed above. After passing VRT1/TS1-1b, trajectories approach to seven different reference structures: (F) MIN1 (86/198), (G) TS1-3a (62/198), (H) TS1-1$d_{outside}$ (22/198), (I) TS1-1a (16/198), (J) TS1-2 (7/198), (K) TS1-4 (4/198), and (L) TS1-3b (1/198). In cases of (H) (7/22) and (L) (1/1), several trajectories do not reach MIN1 during 3 ps. The detailed routes from TS1-1d to the first arrival of MIN1 are summarized in **Figure 2.10**. As shown here, 198/200 trajectories passing through VRT1/TS1-1b are classified into 20 patterns, including eight trajectories not reaching MIN1 during 3 ps. Most trajectories (198/200) go down along the IRC *via* VRT1/TS1-1b, but before reaching MIN1, the trajectories show various routes going through several TSs (IRCs). In other words, the reaction process from TS1-1d to MIN1 is described as complicated dynamical reaction routes related to multiple elementary reaction paths rather than a single IRC. Such a behavior can be regarded as IRC-jump routes, caused by the existence of closely-lying reaction path networks in the configuration space, which sometimes appear as a VRT feature in the IRC pathway. The on-the-fly MD is a powerful tool to detect such a feature of the global reaction route map.

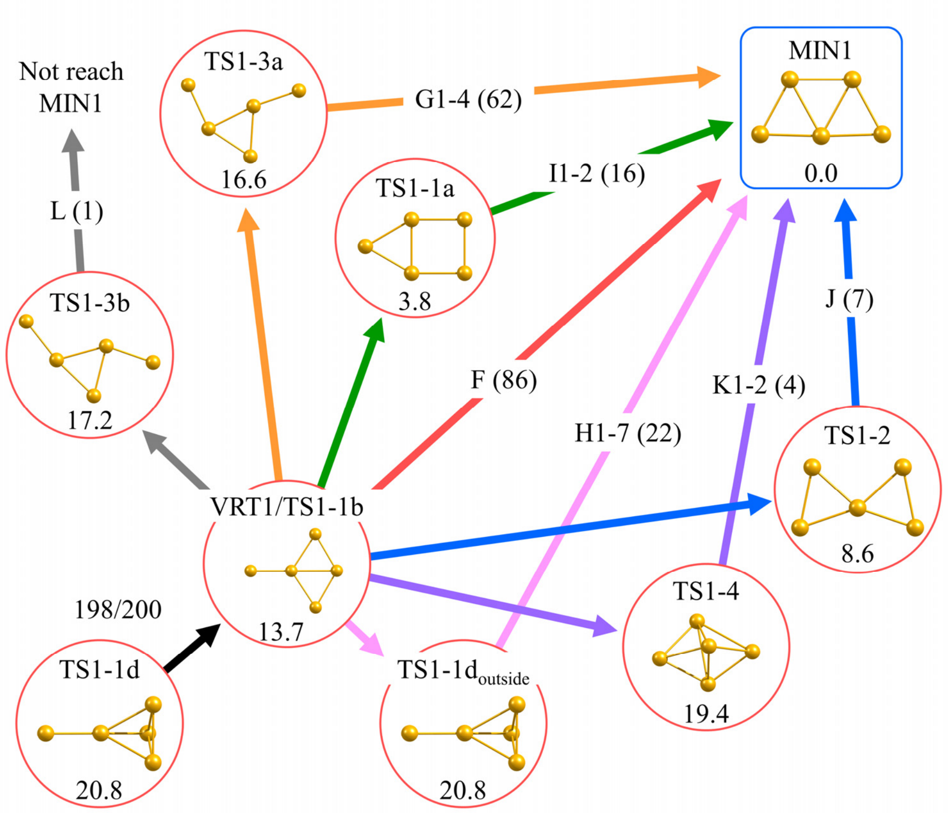
Not reach
MIN1
TS1-3a
16.6
G1-4 (62)
MIN1
0.0
TS1-1a
3.8
I1-2 (16)
L (1)
TS1-3b
17.2
F (86)
H1-7 (22)
K1-2 (4)
J (7)
TS1-2
8.6
VRT1/TS1-1b
13.7
198/200
TS1-1d
20.8
TS1-1d$_{\text{outside}}$
20.8
TS1-4
19.4

Figure 2.9. A schematic picture for the dynamical reaction processes of 198 on-the-fly trajectory from TS1-1d to MIN1 *via* VRT1/TS1-1b after passing through VRT1/TS1-1b. Seven different routes, F ~ L, are illustrated with the number of assigned trajectories. The molecular structure and relative energy (in kcal/mol) are given. Note that TS1-1d$_{\text{outside}}$ indicates the NPI isomer of TS1-1d except for TS1-1d, TS1-1d', and TS1-1d''.

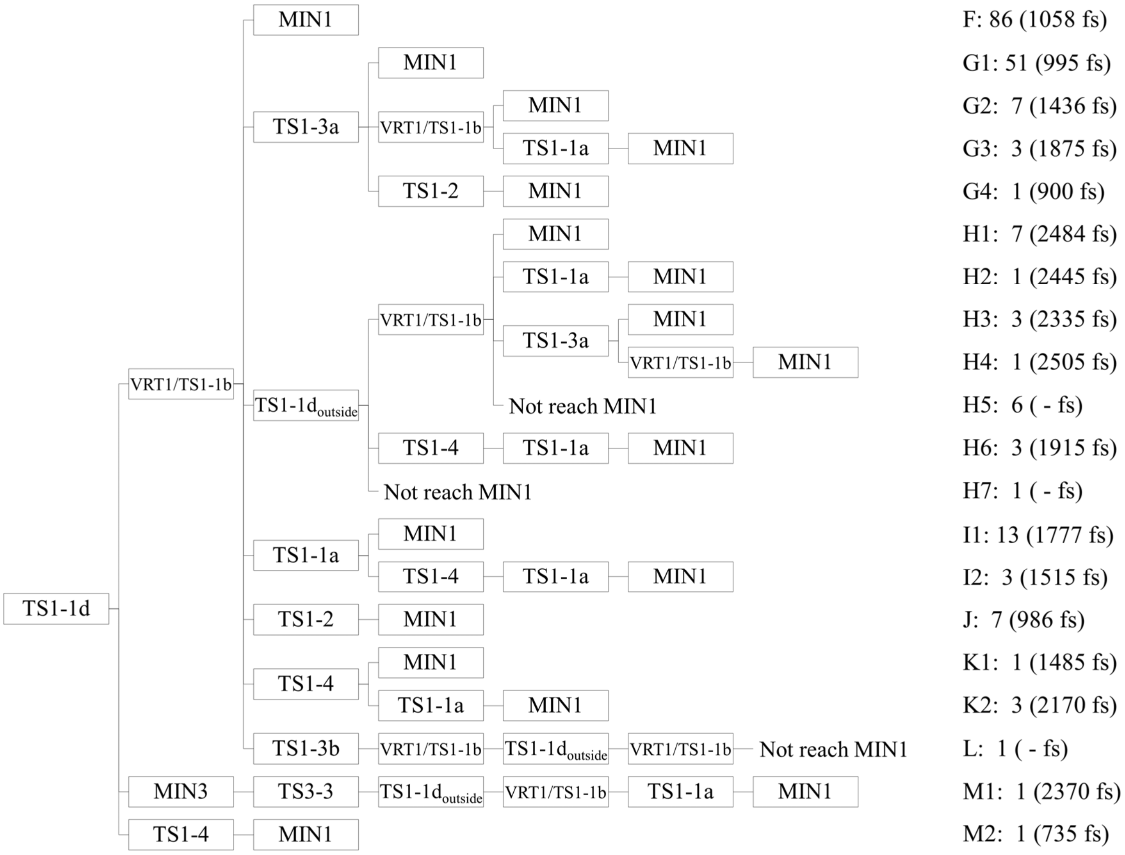
TS1-1d
VRT1/TS1-1b
MIN1
F: 86 (1058 fs)
TS1-3a
MIN1
G1: 51 (995 fs)
VRT1/TS1-1b
MIN1
G2: 7 (1436 fs)
TS1-1a
MIN1
G3: 3 (1875 fs)
TS1-2
MIN1
G4: 1 (900 fs)
TS1-1d$_{\text{outside}}$
VRT1/TS1-1b
MIN1
H1: 7 (2484 fs)
TS1-1a
MIN1
H2: 1 (2445 fs)
TS1-3a
MIN1
H3: 3 (2335 fs)
VRT1/TS1-1b
MIN1
H4: 1 (2505 fs)
Not reach MIN1
H5: 6 (- fs)
TS1-4
TS1-1a
MIN1
H6: 3 (1915 fs)
Not reach MIN1
H7: 1 (- fs)
TS1-1a
MIN1
I1: 13 (1777 fs)
TS1-4
TS1-1a
MIN1
I2: 3 (1515 fs)
TS1-2
MIN1
J: 7 (986 fs)
TS1-4
MIN1
K1: 1 (1485 fs)
TS1-1a
MIN1
K2: 3 (2170 fs)
TS1-3b
VRT1/TS1-1b
TS1-1d$_{\text{outside}}$
VRT1/TS1-1b
Not reach MIN1
L: 1 (- fs)
MIN3
TS3-3
TS1-1d$_{\text{outside}}$
VRT1/TS1-1b
TS1-1a
MIN1
M1: 1 (2370 fs)
TS1-4
MIN1
M2: 1 (735 fs)

Figure 2.10. A dendrogram of 200 trajectories that start from TS1-1d and reach MIN1: (F) VRT1/TS1-1b → MIN1, (G) VRT1/TS1-1b → TS1-3a, (H) VRT1/TS1-1b → TS1-1d$_{\text{outside}}$, (I) VRT1/TS1-1b → TS1-1a, (J) VRT1/TS1-1b → TS1-2, (K) VRT1/TS1-1b → TS1-4, (L) VRT1/TS1-1b → TS1-3b, and (M) not through VRT1/TS1-1b. For the respective routes, the number of trajectories and an average time to reach MIN1 are shown.

2.4 Conclusion

In this chapter, I proposed a new method to analyze on-the-fly trajectories based on a global reaction route map, and this was named the on-the-fly trajectory mapping method. Through developing the proposed method, I introduced the mass-weighted linear distance for molecules and the concept of the nuclear permutation-inversion (NPI) isomer, and then, I defined the distance function, which is a key concept of the on-the-fly trajectory mapping method. The procedure is very simple: the trajectories are mapped on the IRC networks based on the distance functions between given molecular structures (*i.e.* on-the-fly trajectory) and reference points on the reaction pathways in $3N$-dimensional mass-weighted coordinates. The proposed analyses were applied to the Au_5 cluster, which has five MINs and 14 TS structures in the global reaction route map. In this chapter, I selected all NPI isomers generated from five MINs, 14 TSs, and one VRT as the reference structures, in total, 2130 reference structures. The on-the-fly trajectories were run from TS1-1d, which has the highest activation barrier among TSs connecting NPI isomers of MIN1, indicating various bifurcation mechanisms and complicated dynamical reaction processes classified as 20 different routes. From this analysis, I discovered the IRC-jump behaviors caused by the existence of closely-lying reaction path networks in the configuration space and clarified the non-trivial bifurcating processes induced by the IRC-jumps.

In general, the more the molecular system can depart far from the IRC path as the total energy is higher, and thus, the IRC will lose the role of the reference reaction path in high-energy dynamics. In contrast, the on-the-fly trajectory provides the appropriate dynamical reaction route even in the high-energy situation. Therefore, even in such a situation, the present analysis provides fruitful insights into the dynamical reaction processes, which include IRC-jump behaviors.

Recently, such trajectory mapping concepts have been developed for various purposes, and finally, I mention related researches. Olasz and Czakó proposed a new approach to analyze on-the-fly trajectories in the coordinate space by combining the Eckart-transformation-based approach and stationary-point probability, and they discussed the role of the stationary points during various S_N2 reactions.[45,46] Martínez-Núñez *et al.* analyzed the accelerated dynamics simulation using spectral graph theory to obtain stationary points and observed the IRC jumps, which was the basis for obtaining transition states of bimolecular reactions.[47–49] Such as these related studies, I hope that the proposed method will be applied not only to the on-the-fly trajectory analysis but also to the PES-based chemical reaction analysis and the transition state search method.

2.5 References

(1) Fukui, K. Formulation of the Reaction Coordinate. *J. Phys. Chem.* **1970**, *74*, 4161–4163.

(2) Ohno, K.; Maeda, S. Global Reaction Route Mapping on Potential Energy Surfaces of Formaldehyde, Formic Acid, and Their Metal-Substituted Analogues. *J. Phys. Chem. A* **2006**, *110*, 8933–8941.

(3) Maeda, S.; Ohno, K.; Morokuma, K. Systematic Exploration of the Mechanism of Chemical Reactions: The Global Reaction Route Mapping (GRRM) Strategy Using the ADDF and AFIR Methods. *Phys. Chem. Chem. Phys.* **2013**, *15*, 3683.

(4) Maeda, S.; Taketsugu, T.; Morokuma, K.; Ohno, K. Anharmonic Downward Distortion Following for Automated Exploration of Quantum Chemical Potential Energy Surfaces. *Bull. Chem. Soc. Jpn.* **2014**, *87*, 1315–1334.

(5) Maeda, S.; Harabuchi, Y.; Takagi, M.; Saita, K.; Suzuki, K.; Ichino, T.; Sumiya, Y.; Sugiyama, K.; Ono, Y. Implementation and Performance of the Artificial Force Induced Reaction Method in the GRRM17 Program. *J. Comput. Chem.* **2018**, *39*, 233–250.

(6) Maeda, S.; Sugiyama, K.; Sumiya, Y.; Takagi, M.; Saita, K. Global Reaction Route Mapping for Surface Adsorbed Molecules: A Case Study for H 2 O on Cu(111) Surface. *Chem. Lett.* **2018**, *47*, 396–399.

(7) Harabuchi, Y.; Taketsugu, T.; Maeda, S. Exploration of Minimum Energy Conical Intersection Structures of Small Polycyclic Aromatic Hydrocarbons: Toward an Understanding of the Size Dependence of Fluorescence Quantum Yields. *Phys. Chem. Chem. Phys.* **2015**, *17*, 22561–22565.

(8) Maeda, S.; Harabuchi, Y.; Taketsugu, T.; Morokuma, K. Systematic Exploration of Minimum Energy Conical Intersection Structures near the Franck–Condon Region. *J. Phys. Chem. A* **2014**, *118*, 12050–12058.

(9) Suzuki, K.; Maeda, S.; Morokuma, K. Roles of Closed- and Open-Loop Conformations in Large-Scale Structural Transitions of <scp>l</Scp> -Lactate Dehydrogenase. *ACS Omega* **2019**, *4*, 1178–1184.

(10) Sumiya, Y.; Maeda, S. A Reaction Path Network for Wöhler's Urea Synthesis. *Chem. Lett.* **2019**, *48*, 47–50.

(11) Fumanal, M.; Harabuchi, Y.; Gindensperger, E.; Maeda, S.; Daniel, C. Excited-State Reactivity of [Mn(Im)(CO) 3 (Phen)] + : A Structural Exploration. *J. Comput. Chem.* **2019**, *40*, 72–81.

(12) Kato, S.; Morokuma, K. Potential Energy Characteristics and Energy Partitioning

in Chemical Reactions: Ab Initio MO Study of Four-centered Elimination Reaction $CH_3CH_2F \rightarrow CH_2{=}CH_2 + HF$. *J. Chem. Phys.* **1980**, *73*, 3900–3914.

(13) Sun, L.; Song, K.; Hase, W. L. A S_N2 Reaction That Avoids Its Deep Potential Energy Minimum. *Science* **2002**, *296*, 875–878.

(14) Taketsugu, T.; Hirano, T. Mechanism of Bifurcation along the Reaction Path: An Application in the Case of Thioformaldehyde. *J. Chem. Phys.* **1993**, *99*, 9806–9814.

(15) Hare, S. R.; Tantillo, D. J. Cryptic Post-Transition State Bifurcations That Reduce the Efficiency of Lactone-Forming Rh-Carbenoid C–H Insertions. *Chem. Sci.* **2017**, *8*, 1442–1449.

(16) Hare, S. R.; Li, A.; Tantillo, D. J. Post-Transition State Bifurcations Induce Dynamical Detours in Pummerer-like Reactions. *Chem. Sci.* **2018**, *9*, 8937–8945.

(17) Hong, Y. J.; Tantillo, D. J. Biosynthetic Consequences of Multiple Sequential Post-Transition-State Bifurcations. *Nat. Chem.* **2014**, *6*, 104–111.

(18) Harabuchi, Y.; Nakayama, A.; Taketsugu, T. Trifurcation of the Reaction Pathway. *Comput. Theor. Chem.* **2012**, *1000*, 70–74.

(19) Harabuchi, Y.; Ono, Y.; Maeda, S.; Taketsugu, T. Analyses of Bifurcation of Reaction Pathways on a Global Reaction Route Map: A Case Study of Gold Cluster Au_5. *J. Chem. Phys.* **2015**, *143*, 014301.

(20) Ootani, Y.; Satoh, K.; Nakayama, A.; Noro, T.; Taketsugu, T. Ab Initio Molecular Dynamics Simulation of Photoisomerization in Azobenzene in the $N\pi^*$ State. *J. Chem. Phys.* **2009**, *131*, 194306.

(21) Tsutsumi, T.; Harabuchi, Y.; Yamamoto, R.; Maeda, S.; Taketsugu, T. On-the-Fly Molecular Dynamics Study of the Excited-State Branching Reaction of α-Methyl-Cis-Stilbene. *Chem. Phys.* **2018**, *515*, 564–571.

(22) Harabuchi, Y.; Keipert, K.; Zahariev, F.; Taketsugu, T.; Gordon, M. S. Dynamics Simulations with Spin-Flip Time-Dependent Density Functional Theory: Photoisomerization and Photocyclization Mechanisms of Cis- Stilbene in $\Pi\pi^*$ States. *J. Phys. Chem. A* **2014**, *118*, 11987–11998.

(23) Harabuchi, Y.; Yamamoto, R.; Maeda, S.; Takeuchi, S.; Tahara, T.; Taketsugu, T. Ab Initio Molecular Dynamics Study of the Photoreaction of 1,1′-Dimethylstilbene upon $S_0 \rightarrow S_1$ Excitation. *J. Phys. Chem. A* **2016**, *120*, 8804–8812.

(24) Miller, W. H.; Handy, N. C.; Adams, J. E. Reaction Path Hamiltonian for Polyatomic Molecules. *J. Chem. Phys.* **1980**, *72*, 99–112.

(25) Taketsugu, T.; Gordon, M. S. Dynamic Reaction Path Analysis Based on an

Intrinsic Reaction Coordinate. *J. Chem. Phys.* **1995**, *103*, 10042–10049.

(26) Tsutsumi, T.; Harabuchi, Y.; Ono, Y.; Maeda, S.; Taketsugu, T. Analyses of Trajectory On-the-Fly Based on the Global Reaction Route Map. *Phys. Chem. Chem. Phys.* **2018**, *20*, 1364–1372.

(27) Haruta, M. Gold Rush. *Nature* **2005**, *437*, 1098–1099.

(28) Pyykkö, P. Theoretical Chemistry of Gold. *Angew. Chemie Int. Ed.* **2004**, *43*, 4412–4456.

(29) Xu, S.; Zhang, Y.; Wei, Y.; Tian, G. Ground and Excited State Geometrical and Optical Properties of Au (n = 2–13) Nanoclusters: A First-Principles Study. *Comput. Theor. Chem.* **2020**, *1190*, 113007.

(30) Gao, M.; Lyalin, A.; Takagi, M.; Maeda, S.; Taketsugu, T. Reactivity of Gold Clusters in the Regime of Structural Fluxionality. *J. Phys. Chem. C* **2015**, *119*, 11120–11130.

(31) Rogers, D. J.; Tanimoto, T. T. A Computer Program for Classifying Plants. *Science* **1960**, *132*, 1115–1118.

(32) Harabuchi, Y.; Okai, M.; Yamamoto, R.; Tsutsumi, T.; Ono, Y.; Taketsugu, T. SPPR. Hokkaido University: Sapporo, Japan 2020.

(33) Kabsch, W. A Solution for the Best Rotation to Relate Two Sets of Vectors. *Acta Crystallogr. Sect. A* **1976**, *32*, 922–923.

(34) Kabsch, W. A Discussion of the Solution for the Best Rotation to Relate Two Sets of Vectors. *Acta Crystallogr. Sect. A* **1978**, *34*, 827–828.

(35) McLachlan, A. D. Gene Duplications in the Structural Evolution of Chymotrypsin. *J. Mol. Biol.* **1979**, *128*, 49–79.

(36) Miyashita, N.; Yonezawa, Y. On-the-Fly Analysis of Molecular Dynamics Simulation Trajectories of Proteins Using the Bayesian Inference Method. *J. Chem. Phys.* **2017**, *147*, 124108.

(37) Fukutani, T.; Miyazawa, K.; Iwata, S.; Satoh, H. G-RMSD: Root Mean Square Deviation Based Method for Three-Dimensional Molecular Similarity Determination. *Bull. Chem. Soc. Jpn.* **2020**, bcsj.20200258.

(38) Ortiz, A. R.; Strauss, C. E. M.; Olmea, O. MAMMOTH (Matching Molecular Models Obtained from Theory): An Automated Method for Model Comparison. *Protein Sci.* **2009**, *11*, 2606–2621.

(39) Vásquez-Pérez, J. M.; Martínez, G. U. G.; Köster, A. M.; Calaminici, P. The Discovery of Unexpected Isomers in Sodium Heptamers by Born–Oppenheimer Molecular Dynamics. *J. Chem. Phys.* **2009**, *131*, 124126.

(40) Frisch, M. J.; Trucks, G. W.; Schlegel, H. B.; Scuseria, G. E.; Robb, M. A.;

Cheeseman, J. R.; Scalmani, G.; Barone, V.; Petersson, G. A.; Nakatsuji, H.; et al. Gaussian 09. Gaussian, Inc.: Wallingford CT 2016.

(41) Valtazanos, P.; Ruedenberg, K. Bifurcations and Transition States. *Theor. Chim. Acta* **1986**, *69*, 281–307.

(42) Baker, J.; Gill, P. M. W. An Algorithm for the Location of Branching Points on Reaction Paths. *J. Comput. Chem.* **1988**, *9*, 465–475.

(43) Bofill, J. M.; Quapp, W. Analysis of the Valley-Ridge Inflection Points through the Partitioning Technique of the Hessian Eigenvalue Equation. *J. Math. Chem.* **2013**, *51*, 1099–1115.

(44) Hirsch, M.; Quapp, W.; Heidrich, D. The Set of Valley–Ridge Inflection Points on the Potential Energy Surface of Water. *Phys. Chem. Chem. Phys.* **1999**, *1*, 5291–5299.

(45) Czakó, G.; Győri, T.; Olasz, B.; Papp, D.; Szabó, I.; Tajti, V.; Tasi, D. A. Benchmark Ab Initio and Dynamical Characterization of the Stationary Points of Reactive Atom + Alkane and S_N2 Potential Energy Surfaces. *Phys. Chem. Chem. Phys.* **2020**.

(46) Olasz, B.; Czakó, G. Uncovering the Role of the Stationary Points in the Dynamics of the F^- + CH_3I Reaction. *Phys. Chem. Chem. Phys.* **2019**, *21*, 1578–1586.

(47) Martínez-Núñez, E. An Automated Transition State Search Using Classical Trajectories Initialized at Multiple Minima. *Phys. Chem. Chem. Phys.* **2015**, *17*, 14912–14921.

(48) Martínez-Núñez, E. An Automated Method to Find Transition States Using Chemical Dynamics Simulations. *J. Comput. Chem.* **2015**, *36*, 222–234.

(49) Vázquez, S. A.; Otero, X. L.; Martinez-Nunez, E. A Trajectory-Based Method to Explore Reaction Mechanisms. *Molecules* **2018**, *23*, 1–21.

Chapter 3

Visualization of Unique Reaction Route Map by Dimensionality Reduction Method

3.1 Introduction

The intrinsic reaction coordinate (IRC) is a powerful tool to describe an elementary reaction process that connects two minima (a reactant and a product) *via* a transition state (TS) structure in mass-weighted coordinates.[1,2] Recently, Maeda, Ohno, and Morokuma developed automated reaction-path search methods and then produced a concept of "*global reaction route map*," where all minima and TSs for a given molecular system are connected by IRCs.[4] Therefore, the global reaction route map provides a chemical insight into the IRCs and their connectivity, revealing chemical reaction mechanisms and feasible reaction processes. The kinetic simulation analysis with the rate constant matrix contraction method is recently applied to various reaction route map analyses to discuss the reactivity and selectivity based on the experimental conditions and to navigate automated chemical reaction searches.[3,4] Also, by combining the global reaction route map and the molecular dynamics analysis, I developed the on-the-fly trajectory mapping method to examine dynamical reaction routes traveling on a static reaction route map, as shown in **Chapter 2**.[5]

The reaction route map has fruitful information, such as molecular structures, connectivity of stationary points, and quantum chemical properties for each molecular structure. However, since the global reaction route map lies in the $3N-6$ dimensional configurational space, it is hard to appropriately construct the reaction route map (or network) in the lower-dimensional space. Previous studies schematically visualized reaction route maps, including minima, TSs, and IRCs, so that the IRC connectivity is well reproduced,[6–8] but there has been no attempt to generate a reduced-dimensional reaction route map automatically.

Dimensionality reduction techniques are widely used to characterize multi-dimensional data in numerous research fields of natural and social sciences, and several methods are applied to the chemistry: principal component analysis (PCA),[9,10] multidimensional scaling (MDS),[11,12] self-organizing map[13,14], and *t*-distributed stochastic neighbor embedding (*t*-SNE)[15]. The MDS approach embeds multi-dimensional data into a reduced dimensional space by using the pairwise dissimilarity, and the classical MDS (CMDS) is a kind of MDS method that employs the Euclid pairwise distance as the dissimilarity, which is also called the principal coordinate analysis (PCoA).[11,16–18] The CMDS enables us to construct the lower-dimensional principal coordinate space that reflects the mutual distance relationship between multi-dimensional data as much as possible, where similar (non-similar) data are located close together (far apart). Recently, the CMDS approach was applied to the classification of protein conformers and the analysis of molecular dynamics simulation.[19,20] In this chapter, I propose a reduced-dimensionality reaction space determined by the CMDS approach and discuss chemical reaction mechanisms based on two- and three-dimensional reaction space. The CMDS method is applied to the IRC pathway of the intramolecular proton transfer in malonaldehyde ($C_3O_2H_4$) and the S_N2 reaction of $OH^- + CH_3F \rightarrow CH_3OH + F^-$. Finally, I apply the method to all stationary points obtained from the Au_5 cluster to visualize the global reaction route map.

3.2 Concept of Classical Multi-dimensional Scaling

This section introduces the procedure of the CMDS method. In the same manner as **Chapter 2**, let $\boldsymbol{\xi}$ be a 3*N* mass-weighted Cartesian coordinates for an *N* atomic molecular system. Here, the center of mass of molecule *i*, $\boldsymbol{\xi}^{(i)}$, is set as the origin of the x-y-z coordinate system. Conceptually, the CMDS approach transforms a pairwise Euclid distance matrix for a set of *n* data to a configuration matrix, which defines a reduced-dimensional subspace. Thus, for application to molecules, one must prepare the pairwise distance matrix $\mathbf{D}$ where *ij*th element is the Euclid distance (linear distance) between molecule *i* and *j*, $\boldsymbol{\xi}^{(i)}$ and $\boldsymbol{\xi}^{(j)}$, defined by

$$d_{ij} = \sqrt{\sum_{k}^{3N} \left(\xi_k^{(i)} - \xi_k^{(j)}\right)^2} = \left|\boldsymbol{\xi}^{(i)} - \boldsymbol{\xi}^{(j)}\right|. \tag{3-1}$$

To get the optimal pairwise distance, I have to align the orientation of the x-y-z coordinate axes so as to minimize d_{ij}. As mentioned in **Chapter 2**, such alignment is performed by the Kabsch algorithm.[21] Note the distance matrix is, of course, a real symmetric matrix. The CMDS procedure is as follows.[11,16–18]

1) Prepare a distance matrix $\mathbf{D}$ ($n \times n$ matrix) from a set of *n* molecules using equation (3-1).
2) Apply the Young-Householder transformation[22] to a squared distance matrix $\mathbf{D}_{ij}^{(2)} = d_{ij}^2$, and then obtain an inner product matrix $\mathbf{Q}$.

$$\mathbf{Q} = -\frac{1}{2}\left(\mathbf{E} - \frac{1}{n}\mathbf{1}\right)\mathbf{D}^{(2)}\left(\mathbf{E} - \frac{1}{n}\mathbf{1}\right)^T \tag{3-2}$$

Here, $\mathbf{E}$ is a unit matrix and $\mathbf{1}$ is a square matrix with all elements as 1. Through the Young-Householder transformation, a point like the centroid of the distance matrix is set to the origin of data space, resulting in the sum of each row/column of the inner product matrix gets 1. In this sense, this is called *double centering*. Such an operation is regarded as *normalization* in data science and is used in the preprocessing phase.

3) Diagonalize the inner product matrix $\mathbf{Q}$, and then eigenvalues $\{\lambda_1, \cdots, \lambda_n\}$ and the corresponding eigenvectors $\{L_1, \cdots, L_n\}$ are ordered in a descending way of the eigenvalues $(\lambda_1 \geq \lambda_2 \cdots \geq \lambda_n)$.
4) Take p largest eigenvalues $\{\lambda_1, \cdots, \lambda_p\}$ with the corresponding eigenvectors $\{L_1, \cdots, L_p\}$, and generate principal coordinates $\mathbf{X}_a = \mathbf{L}_a \sqrt{\lambda_a} \quad (1 \leq a \leq p)$.

Strictly speaking, for an N atomic molecule, the maximum number of positive eigenvalues (denoted by m) is $3N-6$, corresponding to the dimension of PES. However, it becomes $3N-3$ because three rotational degrees of freedom cannot remove perfectly. The kth eigenvalue describes the amount of information for the kth principal coordinate, X_k, and thus, for validation, I introduce the proportion of variance Λ_k defined as[17]

$$\Lambda_k = \frac{\lambda_k}{\sum_i^m \lambda_i}. \tag{3-3}$$

The cumulated proportion Λ is also determined as[17]

$$\Lambda = \frac{\sum_{k}^{p} \lambda_k}{\sum_{i}^{m} \lambda_i}, \tag{3-4}$$

which describes the accuracy of the *p*-dimensional configuration quantitatively.

There are two limitations to the Euclid distance. One limitation is that it is inapplicable to the different molecular species because the Euclid distance is defined between two isomers of a given molecular system. In order to overcome such a limitation, I will attempt to visualize the reduced-dimensionality reaction space based on a framework of different molecular species in **Chapter 6**. Another limitation is that the Euclid distance depends on the atom mapping. This problem concerned with the nuclear permutation-inversion (NPI) isomers is solved by the merged-NPI approach described in **Chapter 2**. The CMDS method is implemented in the SPPR program developed in our laboratory, where the merged-NPI option is available.[23]

3.3 Results and Discussion

3.3.1 Intramolecular Proton Transfer in Malonaldehyde

The malonaldehyde ($C_3O_2H_4$) with an intramolecular hydrogen bonding of O–H···O undergoes an intramolecular proton transfer *via* tunneling mechanism and has been used to test various semiclassical tunneling theories.[24–29] In such a heavy-light-heavy system, it is well-known that the reaction path is sharply curved around the TS region, where the reaction path can not determine the one-dimensional coordinate. Therefore, the basic approach, the semiclassical WKB method based on the one-dimensional reaction path[30], is insufficient to estimate tunneling contributions. Miller and coworkers proposed a reaction plane model, which is defined by the two reaction-coordinate-like degrees of freedom, two OH bond lengths, and estimated the tunneling behaviors successfully.[25,26] However, they emphasized that "*We have chosen to rely on "chemical intuition" to select them* [two OH bond lengths: r_1 and r_2]. *Thus the choice of* r_1 *and* r_2 *as the two reaction surface coordinates ... seems reasonable, but it is not unique.*"[26] Indeed, Shida *et al.* proposed a three-dimensional reaction model including two OH and OO bond lengths and discussed a tunneling path and an isotope effect.[27,28] In order to avoid such ambiguity, in this section, I construct the uniquely defined two-dimensional reaction coordinate space by the CMDS method.

First, I employed the IRC calculation for this intramolecular proton transfer process in malonaldehyde, which was performed at the B3LYP/6-31G** level using the GAMESS program package.[31] The malonaldehyde has a planar structure with C_s symmetry conserved through the intramolecular proton transfer, while only the TS structure has a more symmetric structure of C_{2v} symmetry. I first optimized the TS geometry under a C_{2v} symmetry restriction, and then I verified that the optimized TS structure has only one imaginary frequency mode. After that, the IRC calculation was carried out from the TS.

Figure 3.1a shows the energy profile (denoted by a black line) and the variations of three bond lengths (denoted by red lines): r(O1H2), r(O3H2), and r(O1O3). The energy variation indicates the symmetric profile with respect to the TS since the geometries of reactant and product minima are symmetric with each other. Figure 3.1b shows the molecular structures of MIN, TS, and MIN' with the labels of several atoms. This IRC path involves three processes: (1) an approach of OH and O ($s = -7.38 \sim -3.00$), (2) an H transfer between O and O ($s = -3.00 \sim 3.00$), and (3) a departure of O and HO ($s = 3.00 \sim 7.38$); where the single and double bonds are exchanged as OH and O approach to (or depart from) each other. This reaction process suggests the sharply curved IRC path around the TS region, indicating that the one-dimensional tunneling path model breaks down.[25,26,29] As shown in Figure 3.1, the IRC is composed of 29 structures, including two minima and one TS. Also, the malonaldehyde involves nine atoms, with 21 internal degrees of freedom (6 out-of-plane and 15 in-plane modes). Since the molecular structure conserves C_s symmetry along the IRC, 29 structures on the IRC can be expressed only by 15 totally symmetric coordinates of C_s symmetry.

(a) Energy profile along the IRC

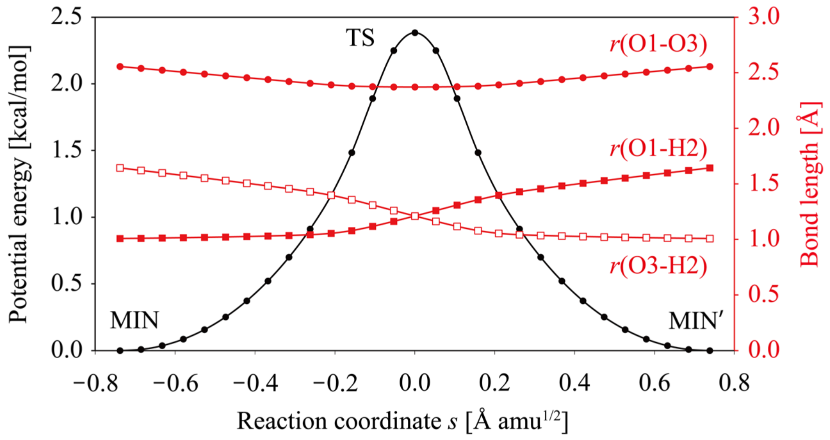

(b) MIN ($s = -7.38$) TS ($s = 0.00$) MIN′ ($s = 7.38$)

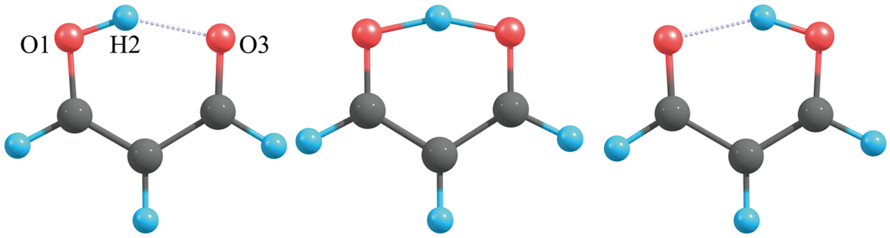

Figure 3.1. (a) The energy profile (black line) and the variations of three internal coordinates (red lines), *r*(O1H2), *r*(O3H2), and *r*(O1O3), along the IRC for the intramolecular proton transfer in malonaldehyde. (b) The molecular structures of MIN, TS, and MIN'.

Next, I applied the CMDS analysis to the 29 structures along the IRC of the intramolecular proton transfer in malonaldehyde. Through a diagonalization of the inner product matrix **Q** in equation (3-2), I obtained 15 positive eigenvalues, which is consistent with 15 totally symmetric coordinates of a planar malonaldehyde. The proportions of variance from the largest and second-largest eigenvalues, Λ_1 and Λ_2, were 0.657 and 0.340, respectively. Therefore, the cumulated proportion, Λ, was 0.997 (almost one) in the two-dimensional subspace, indicating that the multi-dimensional coordinate space correctly reproduces on the reduced-dimensionality reaction space. These results also clarify that the IRC for the intramolecular proton transfer in malonaldehyde is well determined by only two principal coordinates, X_1 and X_2. **Figure 3.2** shows the two-dimensional IRC profile with 29 molecular structures determined by X_1 and X_2. By focusing on the structural changes along each coordinate, I discover the physical meanings of them: X_1 correlates with the atomic movements in terms of proton transfer accompanying the bond alternation between CC single and double bonds, while X_2 correlates with the movements of approach (departure) of O and O atoms. From those results, it is verified that the reduced-dimensionality IRC profile adequately reproduces the features of the intramolecular proton transfer and the two degrees of freedom (Λ_1 = 0.657 and Λ_2 = 0.340) mainly contribute to the reaction process. Again, I should emphasize that the present analysis does not require any chemical intuition of the reaction process and automatically chooses the significant principal coordinates based on the reference structures along the IRC.

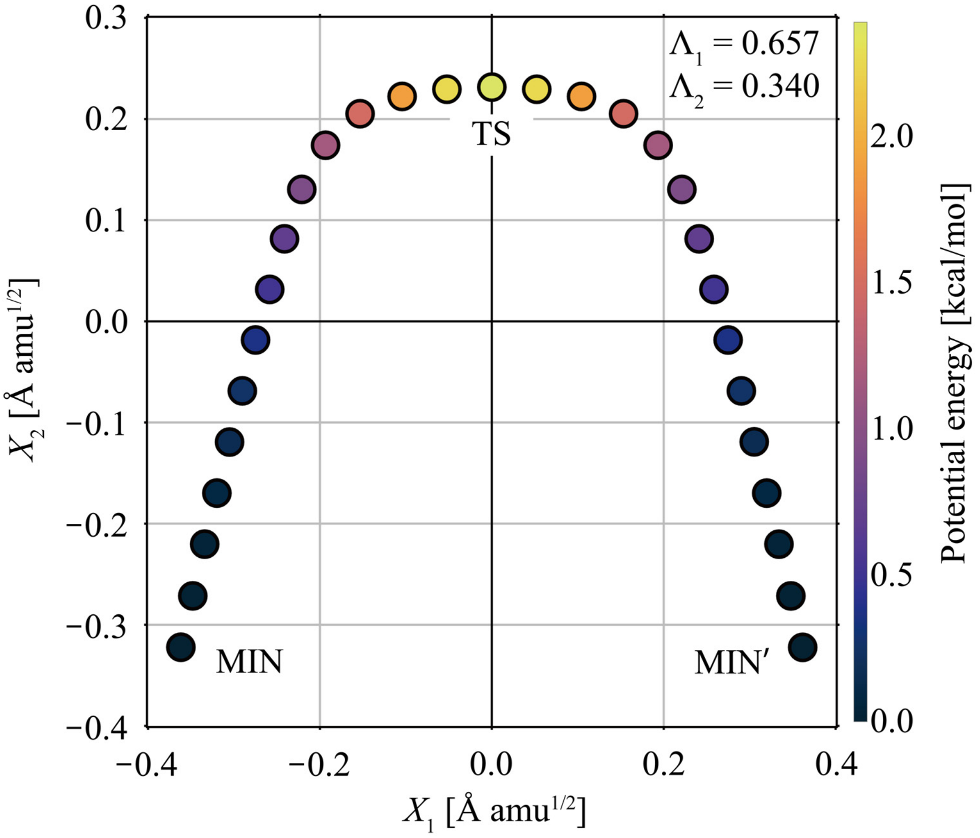

Figure 3.2. The IRC profile of the intramolecular proton transfer of malonaldehyde in the two-dimensional principal coordinate space. The colormap shows the relative energies in kcal/mol. The proportions of variance for two coordinates, Λ_1 and Λ_2, are also shown.

3.3.2 Collision Reaction of OH^{-} +CH_3F → $[CH_3OH\cdots F]^{-}$

The second target reaction is the S_N2 nucleophilic substitution reaction, $OH^- + CH_3F \rightarrow CH_3OH + F^-$ (involving seven atoms with 15 degrees of freedom). According to the IRC calculation at the MP2/6-31+G* level,[32] the product minimum is assigned as a hydrogen-bonded complex, $CH_3OH\cdots F^-$, which is 28.6 kcal/mol more stable than the dissociative products of $CH_3OH + F^-$. Hase and coworkers carried out *ab initio* direct dynamics simulations[33,34] for this reaction, which starts from the transition state toward the product minimum.[32] They found that 90% of trajectories lead to the dissociative products of $CH_3OH + F^-$ (direct dissociation) while only 10% of trajectories lead to the $CH_3OH\cdots F^-$ complex, indicating the significance of "*non-IRC*" dynamical pathways in the actual reaction process.[32] Such non-IRD dynamics can be induced by the curvature of the IRC; when a molecule proceeds along a highly-curved IRC region, a centrifugal force pushes it off the IRC to a negative direction of the curvature vector.[35]

To investigate the geometrical features of the IRC, I carried out the IRC calculation for this S_N2 reaction at the MP2/6-31+G* level using GAMESS.[31] **Figure 3.3a** shows the energy profile along the IRC path, which includes 109 geometries with the reactant (R), the transition state (TS), and the product (P), and the representative structures are also shown in Figure 3.3b. The set of structural change, R → TS → A, corresponds to the intuitive S_N2 reaction process: OH^- attacks the carbon of CH_3F^- from the backside of F^- (R → TS), and then OH is bound to CH_3 through the inversion of the CH_3 umbrella, with departing F^- atom (TS → A). However, unlike a common S_N2 reaction, the IRC continues as follows: (1) F^- loosely bound to C atom moves to the position loosely bound to H atom of CH_3 side (A → B), (2) F^- comes around behind CH_3OH and is finally bound to H atom of the OH (B → P).

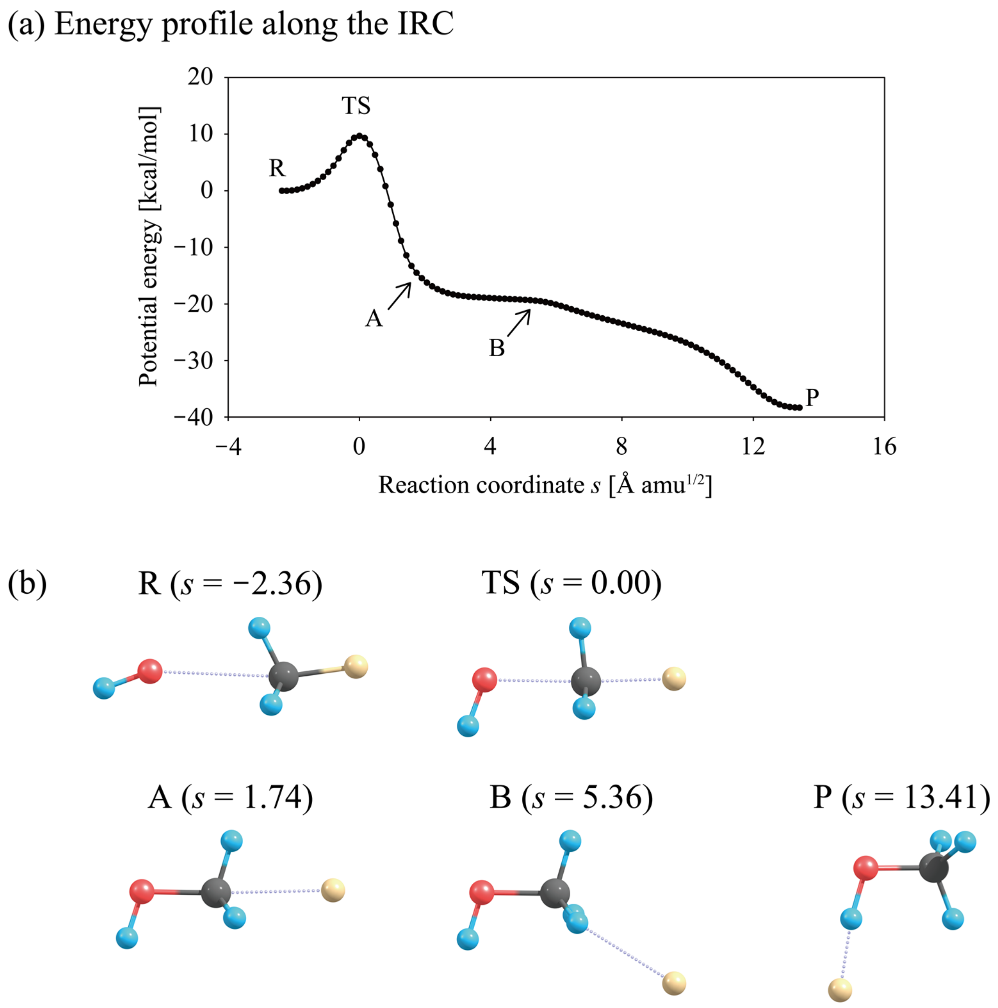

Figure 3.3. (a) The energy profile along the IRC for the S$_\mathrm{N}$2 reaction of OH$^-$ + CH$_3$F → CH$_3$OH + F$^-$. (b) The five representative structures of reactant (R), transition state (TS), product (P), structure A, and B.

Next, I applied the CMDS analysis to the 109 structures located on the IRC. **Figure 3.4a** shows the IRC profile determined by the two principal coordinates, X_1 and X_2, in terms of the 109 structures along the IRC. Interestingly, the IRC path is visualized as a continuous curve in this reduced dimensional space. The proportions of variance, Λ_1 and Λ_2, are 0.815 and 0.137, respectively, and the cumulated proportion, Λ, is 0.952, which indicates that the IRC of the target S_N2 reaction can be mostly defined by two principal coordinates. In order to consider the non-IRC processes reported in the previous study[32], I added five structures of A_i (i = 1~5) where only the C-F interatomic distance r of structure A was modified as follows: the C-F interatomic distance of structure A is 2.28 Å, and that of each A_i is set to 2.50, 2.75, 3.00, 3.25, and 3.50 Å while the other geometrical parameters are fixed. For such 114 structures (IRC + five structures), I carried out the CMDS analysis. Figure 3.4b shows the IRC profile with the direct dissociation pathway (A_1 ~ A_5) determined by the two principal coordinates, Y_1 and Y_2. The proportions of variance from Y_1 and Y_2 become 0.801 and 0.146, respectively, and the cumulated proportion is 0.947. Comparing Figure 3.4a and b, the reduced-dimensionality IRC profile are almost the same, indicating that the two sets of principal coordinates, (X_1 and X_2) and (Y_1 and Y_2), represent similar two-dimensional subspaces even though they refer to the different data set.

From TS to the point around $Y_2 \sim 1.0$ in Figure 3.4b, Y_2 mainly varies with small changes in Y_1, corresponding to the F^- departure from CH_3. After passing through B, the IRC changes its direction suddenly so that both Y_1 and Y_2 decrease linearly, corresponding to the F^- migration. Such aspects suggest that Y_1 is mainly correlated with O-C-F bond angle, while Y_2 is mainly correlated with the C-F interatomic distance. Indeed, the dissociation path to CH_3OH and F^- represented by A_1 ~ A_5 is mainly expressed by Y_2 and branches around the sharply curved region near B. Thus, the CMDS analysis clarifies that the non-IRC reactions are promoted by the dynamics effect such as the centrifugal force (the inertial force), which effectively pushes the molecule off the IRC toward this direct dissociation path.

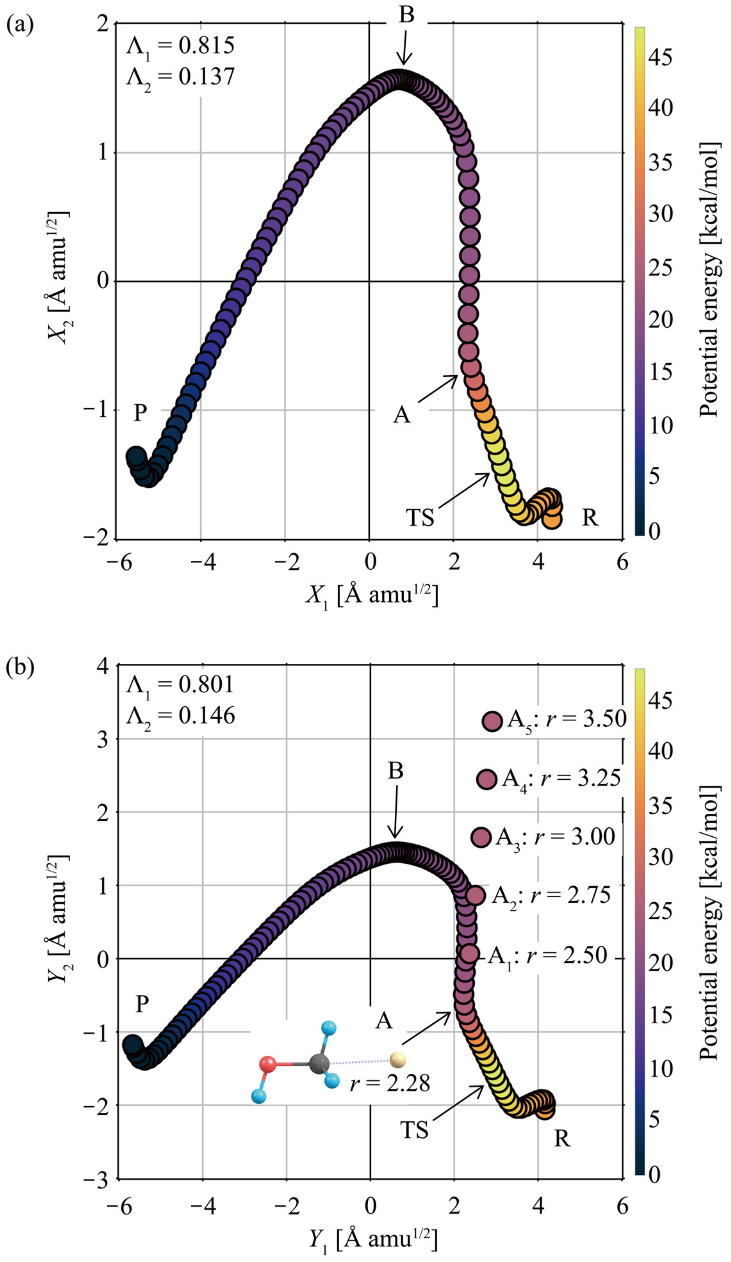

Figure 3.4. The IRC profile of the $\mathrm{S_N2}$ reaction of $OH^- + CH_3F \rightarrow CH_3OH + F^-$ in the two-dimensional principal coordinate space generated from (a) 109 structures along the IRC and (b) 114 structures with the additional five points A_i (i = 1~5) whom the C-F interatomic distance r is set to 2.50, 2.75, 3.00, 3.25, and 3.50 Å while other geometrical parameters are fixed. The colormap shows the relative energies in kcal/mol. The proportions of variance for two coordinates, Λ_1 and Λ_2, are also shown.

3.3.3 Global Reaction Route Map of Au_5 Cluster

Gold bulk is an inert material, but gold nanoparticle achieves a catalytic activity; the smaller the nanoparticle radius, the more sharply the activity increases.[36] The significance of theoretical studies on the catalytic activity of the gold cluster increases more and more.[37,38] In the previous study, Harabuchi *et al.* investigated the global reaction route map of the Au_5 cluster and discussed features of the reaction-path bifurcation by surveying valley-ridge transition points along the IRC paths.[8] In **Chapter 2**, I also investigate the isomerization reaction mechanisms of Au_5 by the on-the-fly trajectory mapping method, which examines a dynamical reaction route along a trajectory based on an IRC network, and uncovered that many trajectories do not follow the IRC path and undergo the IRC-jump behaviors.[5] In this section, I apply the CMDS analysis to the stationary points on the global reaction route map of Au_5 in order to visualize the reduced-dimensionality map. As shown in **Chapter 2**, the Au_5 cluster has five minima (referred to as MINi; $i = 1{\sim}5$) and 14 transition states (referred to as TSi-j connecting MINi and MINj) in the global reaction route map.[8] Among 14 TSs, seven TSs are categorized as TSi-i that connects the NPI isomers of MINi. The global minimum, MIN1, is directly linked to nine TSs, consisting of four TSi-i (TS1-1a, TS1-1b, TS1-1c, and TS1-1d) and five TSi-j (TS1-2, TS1-3a, TS1-3b, TS1-4, and TS1-5). **Figure 3.5** shows the geometrical structures of five minima and 14 TSs, relative energies, and the principal coordinates (X_1, X_2, and X_3) determined by the CMDS analysis.

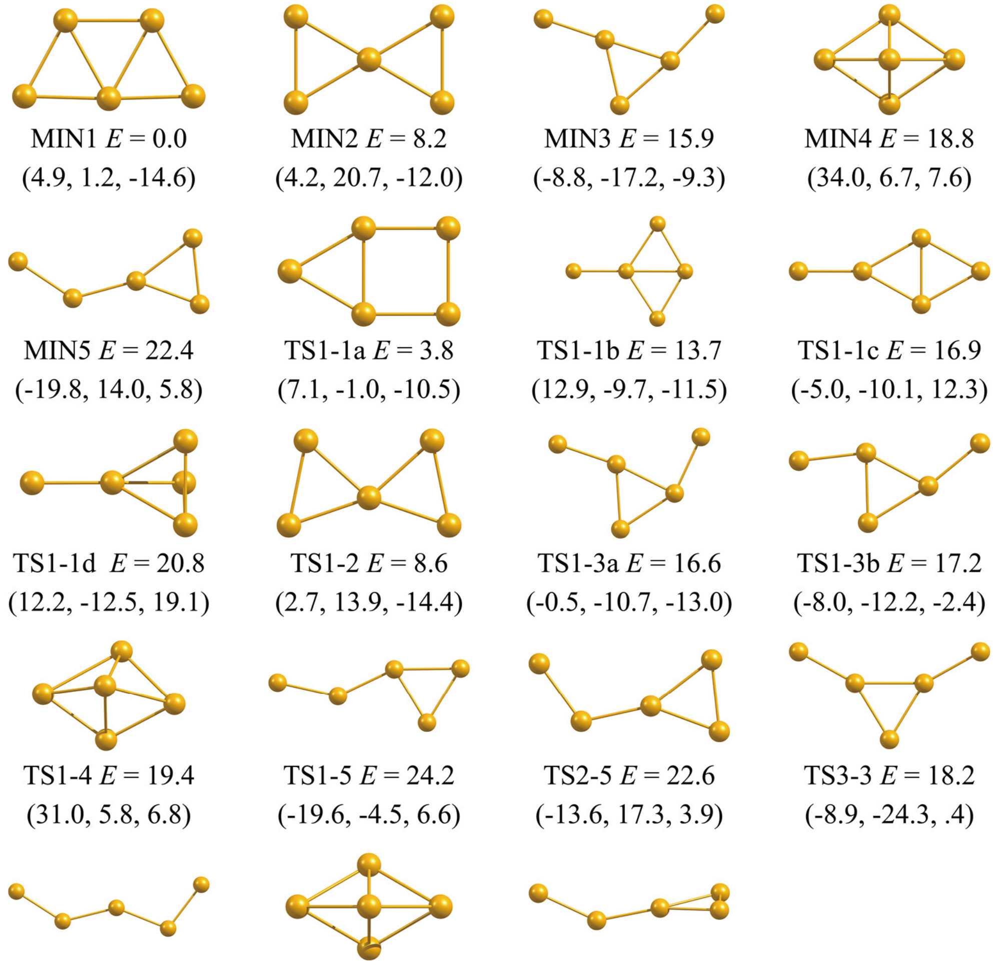

MIN1 $E = 0.0$ (4.9, 1.2, -14.6)

MIN2 $E = 8.2$ (4.2, 20.7, -12.0)

MIN3 $E = 15.9$ (-8.8, -17.2, -9.3)

MIN4 $E = 18.8$ (34.0, 6.7, 7.6)

MIN5 $E = 22.4$ (-19.8, 14.0, 5.8)

TS1-1a $E = 3.8$ (7.1, -1.0, -10.5)

TS1-1b $E = 13.7$ (12.9, -9.7, -11.5)

TS1-1c $E = 16.9$ (-5.0, -10.1, 12.3)

TS1-1d $E = 20.8$ (12.2, -12.5, 19.1)

TS1-2 $E = 8.6$ (2.7, 13.9, -14.4)

TS1-3a $E = 16.6$ (-0.5, -10.7, -13.0)

TS1-3b $E = 17.2$ (-8.0, -12.2, -2.4)

TS1-4 $E = 19.4$ (31.0, 5.8, 6.8)

TS1-5 $E = 24.2$ (-19.6, -4.5, 6.6)

TS2-5 $E = 22.6$ (-13.6, 17.3, 3.9)

TS3-3 $E = 18.2$ (-8.9, -24.3, .4)

TS3-5 $E = 27.3$ (-34.9, 9.2, 1.4)

TS4-4 $E = 19.3$ (34.6, 5.0, 9.6)

TS5-5 $E = 23.0$ (-24.5, 8.4, 14.1)

Figure 3.5. All minima and TS structures for Au_5, calculated by PBE/LanL2DZ.[8] The relative energy E (in kcal/mol) and the principal coordinates (X_1, X_2, X_3) (in Å amu$^{1/2}$) are also given for each structure.

To construct the reduced-dimensionality reaction space of Au_5, I prepare the distance matrix $\mathbf{D}$ for 19 structures (five MINs and 14 TSs) with the merged-NPI option by using the SPPR program[23] and then define the principal coordinates with following the CMDS procedure (Section 3.2). **Figure 3.6** shows the proportion of variance of each eigenvector from the CMDS analysis. There are 12 positive eigenvalues corresponding to the rotational and vibrational degrees of freedom of Au_5 ($3N - 3 = 12$). The top three proportions of variance are 0.466, 0.200, and 0.143, and then the cumulated proportion for the first two principal coordinates is 0.666, while the one for the first three is 0.809. Thus, the configuration of MINs and TSs placed in the reduced two- or three-dimensional subspace should work well to provide intuitive pictures of the mutual relations for each structure.

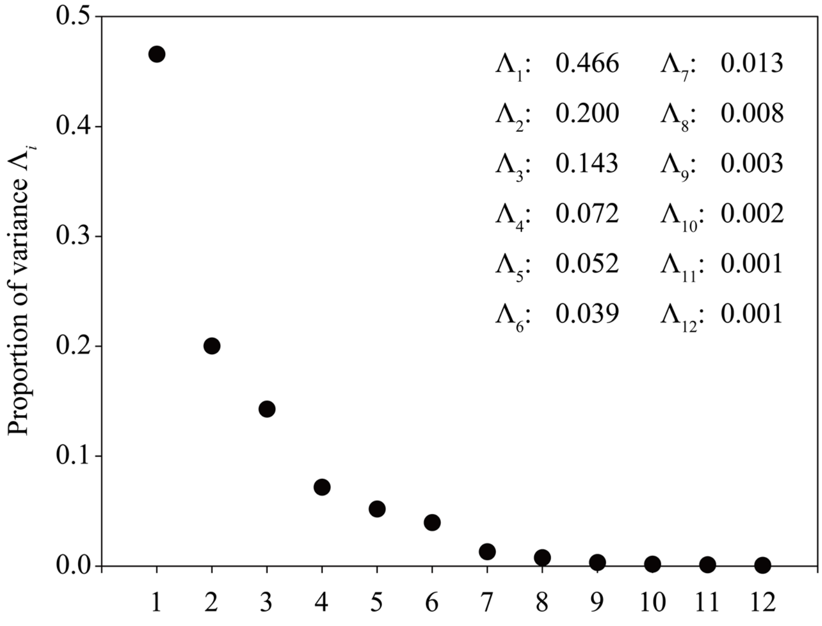

Figure 3.6. The proportion of variance for 19 structures on the global reaction route map for Au_5, obtained from the CMDS analysis.

Figure 3.7 shows the structural changes along the principal coordinates X_i, (a) X_1, (b) X_2, and (c) X_3, with several structures that have relatively small values for $\left|X_j\right|\left(j \neq i\right)$ and reflects the physical meanings of each principal coordinate. Figure 3.7a shows the structural changes along X_1, indicating that the more X_1 increases from negative to positive, the more the molecular geometries changes as quasi-linear (TS3-5), two-dimensional planar (TS1-5, TS1-3b, and MIN1), and three-dimensional non-planar structures (MIN4, TS1-4, and TS4-4). In other words, as X_1 increases, the number of Au-Au bonds increases, such as four bonds in TS3-5, seven bonds in MIN1, and nine bonds in TS4-4. This result is in good agreement with the tendency that a small gold cluster prefers to be a two-dimensional planar structure due to relativistic effects, as mentioned above. Figure 3.7b shows the structural changes along X_2 as follows: both the top and bottom-left Au atoms rotate in a clockwise direction as TS3-3 → TS1-3a → MIN1, and then, the center Au atom in MIN1 goes down to make MIN2, where blue arrows denote the characteristic atomic movements from TS3-3 to MIN2. Figure 3.7c shows that the molecular structures vary in the order MIN1, TS1-1b, TS1-3b, TS1-5, TS1-1c, and TS1-1d along X_3. These structures have a common tendency that Au_5 is composed of a nearly-equilateral triangle Au_3 (denoted by a blue triangle) and two other Au atoms. Consequently, as X_3 increases, the two Au atoms change to a linear form.

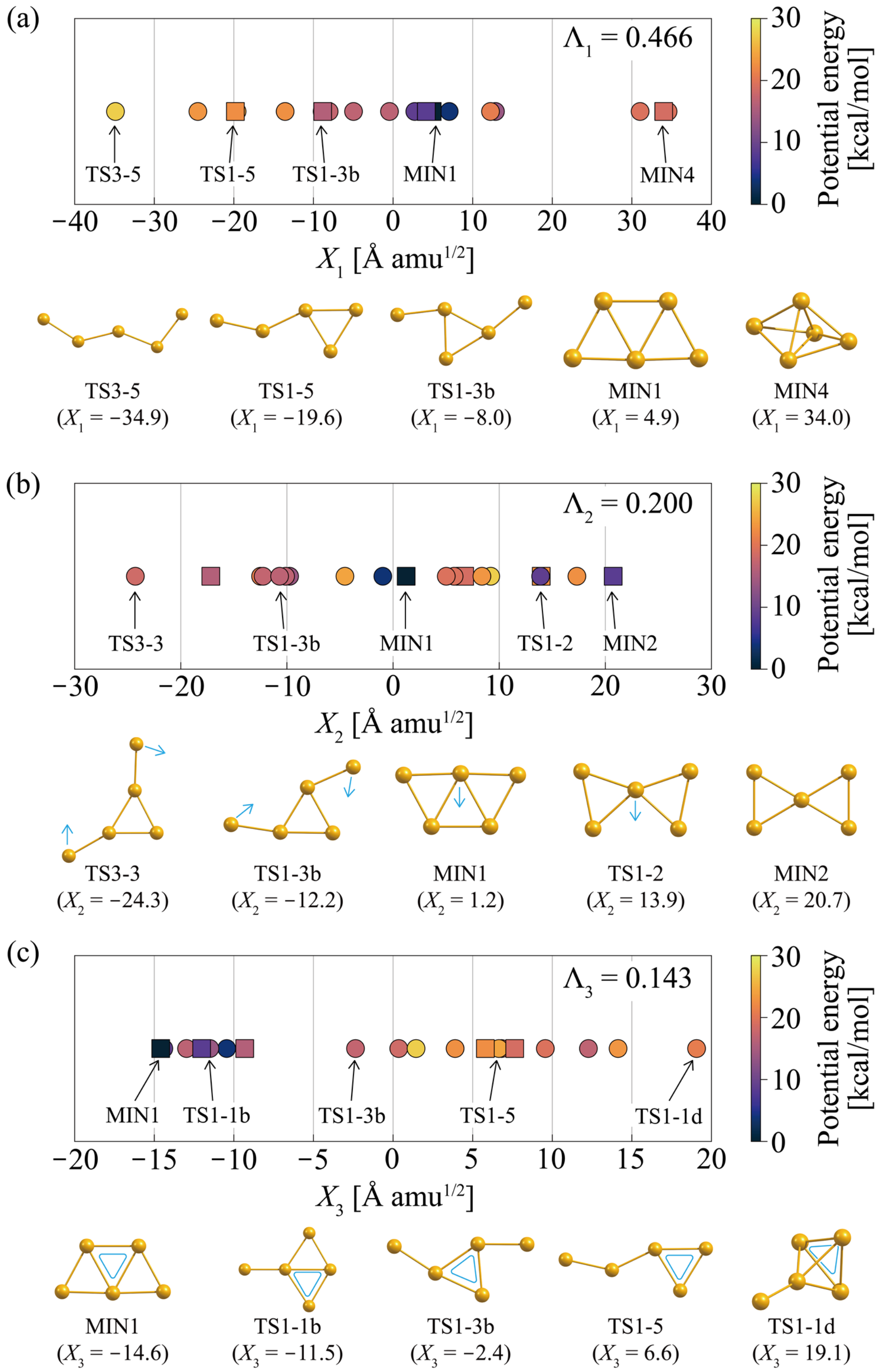

Figure 3.7. The distributions of 19 structures of Au_5 consisting of five MINs and 14 TSs in the global reaction route map, along the axis of the principal coordinates, (a) X_1, (b) X_2, and (c) X_3.

Figure 3.8 shows (a) two- and (b) three-dimensional global reaction route maps for Au_5, including five minima (denoted by squares) and 14 TSs (denoted by circles). In the two-dimensional map (Figure 3.8a), the global minimum, MIN1, is located almost at the origin, and the other four minima are located far away from each other. The low-energy region, including MIN1, MIN2, TS1-1a, and TS1-2, is roughly located in the range of $(X_1, X_2) = (5, -5 \sim 25)$. Additionally, TS*i*-*i* is located near MIN*i*, while TS*i*-*j* is located between MIN*i* and MIN*j*. The two-dimensional configuration obtained by the CMDS method is very informative and coincides with intuitive pictures for the reaction route network. The three-dimensional map (Figure 3.8b) clearly shows that TS1-1c, TS1-1d, and TS5-5 are separated from other structures, even though they are close to others in the two-dimensional map. Especially, TS1-1d and TS1-1b are located very closely in Figure 3.8a, but they have separated far away in Figure 3.8b. This feature can be interpreted by the meaning of the X_3 axis discussed above; TS1-1b comprises one Au atom and the diamond shape of Au_4, showing a relatively large negative X_3 value.

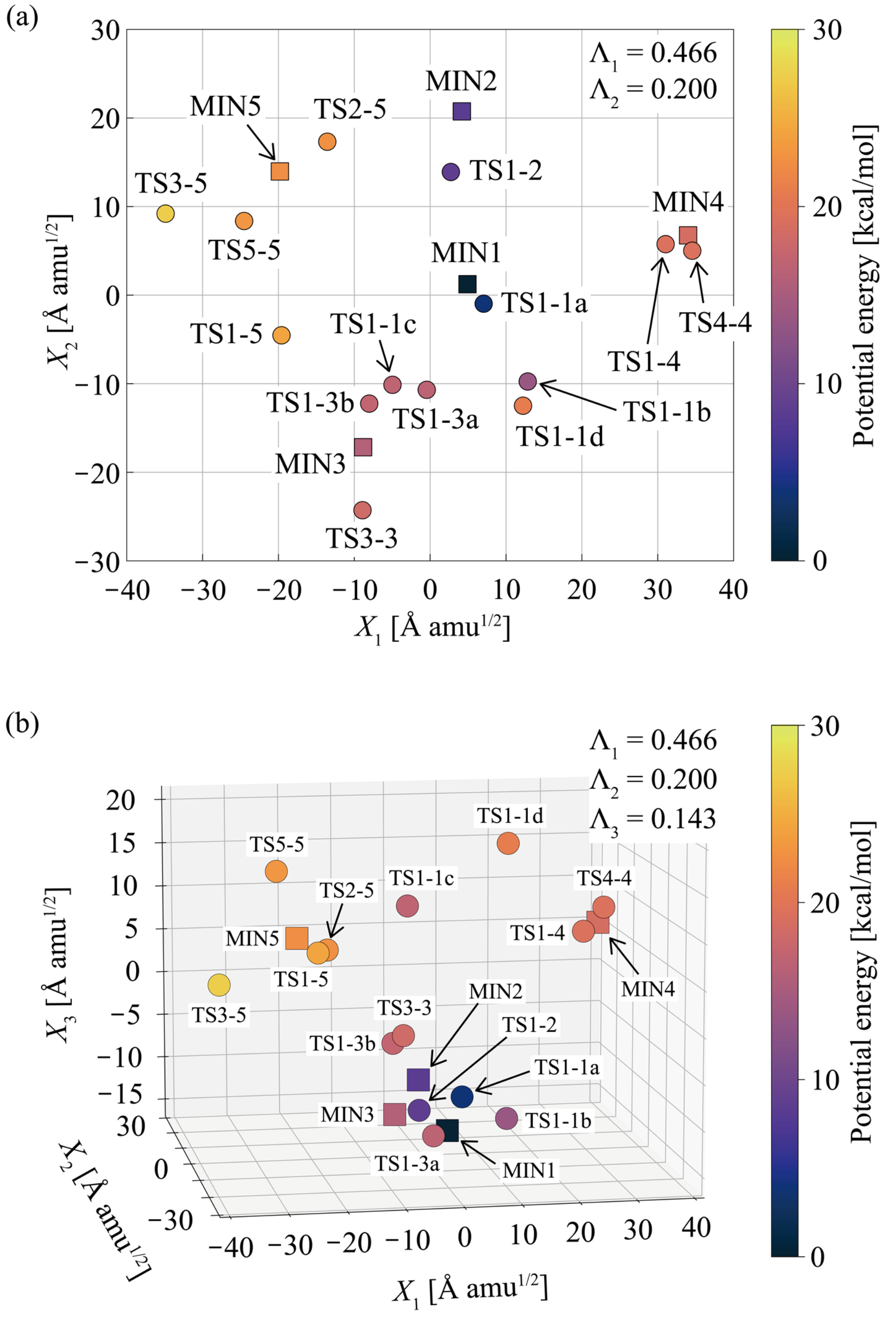

Figure 3.8. The five MINs (denoted by squares) and 14 TSs (denoted by circles) in the global reaction route map for Au_5, reduced to (a) two-dimension and (b) three-dimension by the CMDS analysis. The colormap shows the relative energies in kcal/mol. The proportions of variance for two coordinates, Λ_1 and Λ_2, are also shown.

Finally, I show a two-dimensional global reaction route map for Au_5 in **Figure 3.9**, where the straight lines link all stationary points including five minima and 14 TSs. In previous studies, such a two-dimensional map was illustrated by chemical intuition in terms of molecular similarity and IRC connectivity.[5,8] The reduced-dimensionality global reaction route map, however, is automatically generated based on the pairwise distance matrix for all the molecular structures by the CMDS method, and it assures the validity by a mathematical foundation. The location of each structure and its connectivity can provide a wealth of information to the structural transformations of Au_5. In **Chapter 2**, I proposed the on-the-fly trajectory mapping method that enables us to analyze dynamical reaction routes based on a global reaction route map.[5] Then, I applied it to the isomerization reaction of Au_5. In total, 200 trajectories were run starting from TS1-1d, and 198/200 trajectories first come across TS1-1b. After passing TS1-1b, 86/198 trajectories directly reached MIN1, while 62/198 trajectories approached TS1-3a before reaching MIN1.[5] Such dynamical behavior now can explain based on the reduced reaction map shown in Figure 3.9. The combination of a dynamical trajectory analysis with a reduced global reaction route map provides a deeper insight and understanding of chemical reaction dynamics.

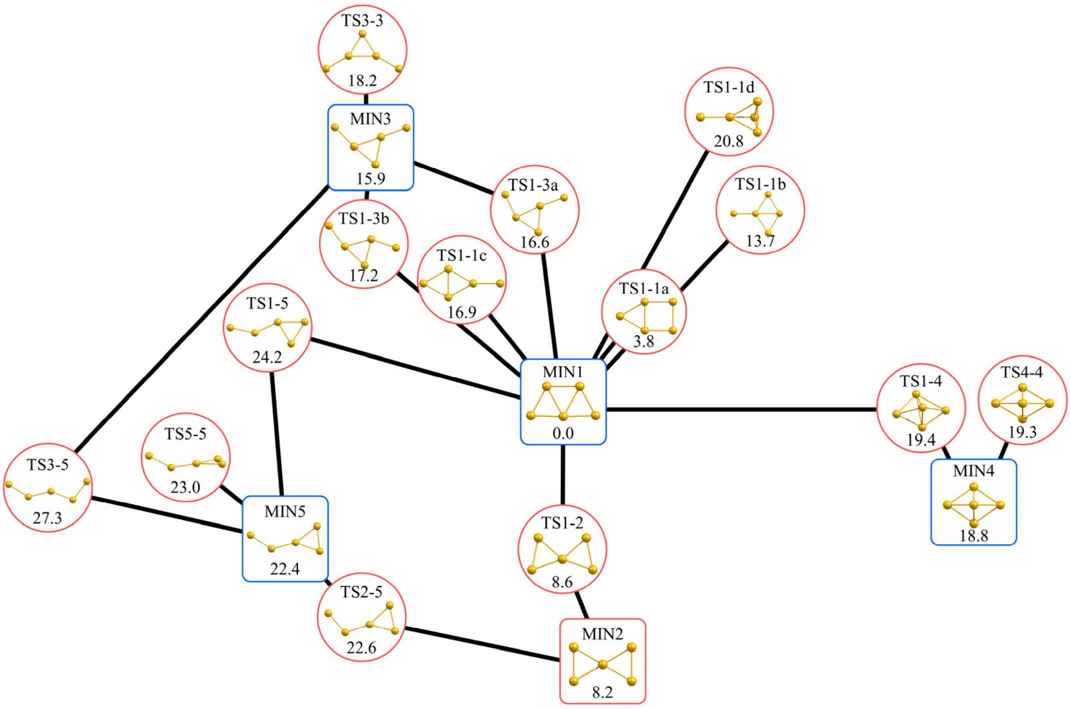
TS3-3
18.2
MIN3
15.9
TS1-1d
20.8
TS1-3a
16.6
TS1-1b
13.7
TS1-3b
17.2
TS1-1c
16.9
TS1-5
24.2
TS1-1a
3.8
MIN1
0.0
TS1-4
19.4
TS4-4
19.3
MIN4
18.8
TS3-5
27.3
TS5-5
23.0
MIN5
22.4
TS1-2
8.6
TS2-5
22.6
MIN2
8.2

Figure 3.9. The two-dimensional reduced global reaction route map of Au_5. Five MINs (blue squares) and 14 TSs (red circles) are connected by straight lines. The relative energy (in kcal/mol) is given for each structure.

3.4 Conclusion

In order to visualize multi-dimensional reaction routes, such as an IRC path and a global reaction route map, I employed the classical multidimensional scaling (CMDS) analysis to embed molecular structures onto a two- or three-dimensional subspace. Conceptually, the CMDS analysis transforms a distance matrix for a set of *n* data to a principal coordinate matrix, and thus, for application to molecules, I employed the pairwise distance matrix between molecules, as defined in equation (3-1). The validation of the dimensionality reduction can be assessed using the proportion of variance and the cumulated proportion.

As the first application, I visualized the IRC path of the intramolecular proton transfer in malonaldehyde. This reaction is categorized as a heavy-light-heavy mass-combination system where the IRC sharply curves around TS. The CMDS analysis successfully reproduced such a highly curved nature, and it verified that the IRC was well represented by only two principal coordinates: the H-transfer and the approach of two O atoms. The second application is the IRC path analysis of the S_N2 reaction, $OH^- + CH_3F \rightarrow CH_3OH + F^-$, and it was reported that the molecule deviates from the IRC and then proceeds to the non-IRC direct dissociation because of dynamical effects.[32] The visualized IRC profile in the two-dimensional principal coordinate space clearly shows the sharply curved path, predicting that the molecule will be pushed off from the curved region on the IRC. In the third application, the CMDS method was applied to five minima and 14 TSs in the global reaction route map of Au_5. The cumulated proportion of the first three principal coordinates was calculated as 0.809, indicating that all structures are appropriately described in the three-dimensional space. The reduced-dimensionality global reaction route map, in fact, well-reproduced the stationary point's connectivity, providing an intuitive insight into the isomerization reaction of the Au_5 cluster. The present analysis is a robust approach to visualize a set of molecular structures and reaction paths into a reduced-dimensional subspace by the pairwise distance relationship. Thus, I hope it will be used to clarify a geometrical feature of IRCs and an entire picture of a global reaction route map.

Very recently, Hare *et al.*[39] analyzed a series of molecular geometries by the principal component analysis (PCA) and visualized several IRC paths, which were discussed in this chapter[40], and the molecular dynamics trajectories, for example, the IRC of the intramolecular proton transfer in malonaldehyde and the IRC of the collision reaction of $OH^- + CH_3F \rightarrow CH_3OH + F^-$. They also published the PCA-based technique as the *PathReducer* program. The PCA is one of the most famous dimensionality reduction methods and is strictly consistent with the CMDS procedure in the general case. The advantage of PCA is to clearly interpret the meanings of each axis by transforming the reduced-dimensional data back into the full-dimensional space mathematically, which is called the reconstruction. However, for application to molecular systems, the pairwise molecular dissimilarity cannot be technically considered because PCA requires a common x-y-z Cartesian coordinate axes to all molecules. Also, the NPI treatment becomes more complicated in PCA. As discussed in this chapter,[40] the CMDS approach can handle such problems by utilizing the Kabsch algorithm[21] and the merged-NPI option, but the meanings of each principal coordinates are not clear and should be interpreted after visualization. I expect that both CMDS and PCA approaches are utilized as complementary tools visualizing a series of molecular geometries in the multi-dimensional space.

3.5 References

(1) Fukui, K. Formulation of the Reaction Coordinate. *J. Phys. Chem.* **1970**, *74*, 4161–4163.

(2) Fukui, K. The Path of Chemical Reactions — The IRC Approach. *Acc. Chem. Res.* **1981**, *14*, 363–368.

(3) Sumiya, Y.; Nagahata, Y.; Komatsuzaki, T.; Taketsugu, T.; Maeda, S. Kinetic Analysis for the Multistep Profiles of Organic Reactions: Significance of the Conformational Entropy on the Rate Constants of the Claisen Rearrangement. *J. Phys. Chem. A* **2015**, *119*, 11641–11649.

(4) Sumiya, Y.; Maeda, S. A Reaction Path Network for Wöhler's Urea Synthesis. *Chem. Lett.* **2019**, *48*, 47–50.

(5) Tsutsumi, T.; Harabuchi, Y.; Ono, Y.; Maeda, S.; Taketsugu, T. Analyses of Trajectory On-the-Fly Based on the Global Reaction Route Map. *Phys. Chem. Chem. Phys.* **2018**, *20*, 1364–1372.

(6) Ohno, K.; Maeda, S. Global Reaction Route Mapping on Potential Energy Surfaces of Formaldehyde, Formic Acid, and Their Metal-Substituted Analogues. *J. Phys. Chem. A* **2006**, *110*, 8933–8941.

(7) Maeda, S.; Sugiyama, K.; Sumiya, Y.; Takagi, M.; Saita, K. Global Reaction Route Mapping for Surface Adsorbed Molecules: A Case Study for H 2 O on Cu(111) Surface. *Chem. Lett.* **2018**, *47*, 396–399.

(8) Harabuchi, Y.; Ono, Y.; Maeda, S.; Taketsugu, T. Analyses of Bifurcation of Reaction Pathways on a Global Reaction Route Map: A Case Study of Gold Cluster Au_5. *J. Chem. Phys.* **2015**, *143*, 014301.

(9) Hotelling, H. Analysis of a Complex of Statistical Variables into Principal Components. *J. Educ. Psychol.* **1933**, *24*, 417–441.

(10) Pearson, K. LIII. On Lines and Planes of Closest Fit to Systems of Points in Space. *London, Edinburgh, Dublin Philos. Mag. J. Sci.* **1901**, *2*, 559–572.

(11) Torgerson, W. S. Multidimensional Scaling: I. Theory and Method. *Psychometrica* **1952**, *17*, 401–419.

(12) Kruskal, J. B. Multidimensional Scaling by Optimizing Goodness of Fit to a Nonmetric Hypothesis. *Psychometrika* **1964**, *29*, 1–27.

(13) Kohonen, T. Self-Organized Formation of Topologically Correct Feature Maps. *Biol. Cybern.* **1982**, *43*, 59–69.

(14) Horton, D. E.; Johnson, N. C.; Singh, D.; Swain, D. L.; Rajaratnam, B.; Diffenbaugh, N. S. Contribution of Changes in Atmospheric Circulation Patterns

to Extreme Temperature Trends. *Nature* **2015**, *522*, 465–469.

(15) Van Der Maaten, L.; Hinton, G. Visualizing Data Using T-SNE. *J. Mach. Learn. Res.* **2008**.

(16) Borg, I.; Groenen, P. J. F. *Modern Multidimensional Scaling*; Springer Series in Statistics; Springer New York: New York, NY, 2005.

(17) Härdle, W. K.; Simar, L. *Applied Multivariate Statistical Analysis*, 3rd Edit.; Springer Berlin Heidelberg: Berlin, Heidelberg, 2015.

(18) Koch, I. *Analysis of Multivariate and High-Dimensional Data*; Cambridge University Press: Cambridge, 2013.

(19) Pisani, P.; Caporuscio, F.; Carlino, L.; Rastelli, G. Molecular Dynamics Simulations and Classical Multidimensional Scaling Unveil New Metastable States in the Conformational Landscape of CDK2. *PLoS One* **2016**, *11*, 1–23.

(20) Li, X.; Xie, Y.; Hu, D.; Lan, Z. Analysis of the Geometrical Evolution in On-the-Fly Surface-Hopping Nonadiabatic Dynamics with Machine Learning Dimensionality Reduction Approaches: Classical Multidimensional Scaling and Isometric Feature Mapping. *J. Chem. Theory Comput.* **2017**, *13*, 4611–4623.

(21) Kabsch, W. A Solution for the Best Rotation to Relate Two Sets of Vectors. *Acta Crystallogr. Sect. A* **1976**, *32*, 922–923.

(22) Young, G.; Householder, A. S. Discussion of a Set of Points in Terms of Their Mutual Distances. *Psychometrika* **1938**, *3*, 19–22.

(23) Harabuchi, Y.; Okai, M.; Yamamoto, R.; Tsutsumi, T.; Ono, Y.; Taketsugu, T. SPPR. Hokkaido University: Sapporo, Japan 2020.

(24) Bicerano, J.; Schaefer, H. F.; Miller, W. H. Structure and Tunneling Dynamics of Malonaldehyde. A Theoretical Study. *J. Am. Chem. Soc.* **1983**, *105*, 2550–2553.

(25) Carrington, T.; Miller, W. H. Reaction Surface Hamiltonian for the Dynamics of Reactions in Polyatomic Systems. *J. Chem. Phys.* **1984**, *81*, 3942–3950.

(26) Carrington, T.; Miller, W. H. Reaction Surface Description of Intramolecular Hydrogen Atom Transfer in Malonaldehyde. *J. Chem. Phys.* **1986**, *84*, 4364–4370.

(27) Shida, N.; Barbara, P. F.; Almlöf, J. E. A Theoretical Study of Multidimensional Nuclear Tunneling in Malonaldehyde. *J. Chem. Phys.* **1989**, *91*, 4061–4072.

(28) Shida, N.; Almlof, J.; Barbara, P. F. Tunneling Paths in Intramolecular Proton Transfer. *J. Phys. Chem.* **1991**, *95*, 10457–10464.

(29) Yagi, K.; Taketsugu, T.; Hirao, K. Generation of Full-Dimensional Potential Energy Surface of Intramolecular Hydrogen Atom Transfer in Malonaldehyde and Tunneling Dynamics. *J. Chem. Phys.* **2001**, *115*, 10647–10655.

(30) Ford, K. W.; Hill, D. L.; Wakano, M.; Wheeler, J. A. Quantum Effects near a Barrier Maximum. *Ann. Phys. (N. Y).* **1959**, *7*, 239–258.

(31) Schmidt, M. W.; Baldridge, K. K.; Boatz, J. A.; Elbert, S. T.; Gordon, M. S.; Jensen, J. H.; Koseki, S.; Matsunaga, N.; Nguyen, K. A.; Su, S.; et al. General Atomic and Molecular Electronic Structure System. *J. Comput. Chem.* **1993**, *14*, 1347–1363.

(32) Sun, L.; Song, K.; Hase, W. L. A S_N2 Reaction That Avoids Its Deep Potential Energy Minimum. *Science* **2002**, *296*, 875–878.

(33) Ma, X.; Hase, W. L. Perspective: Chemical Dynamics Simulations of Non-Statistical Reaction Dynamics. *Philos. Trans. R. Soc. A Math. Phys. Eng. Sci.* **2017**, *375*, 20160204.

(34) Pratihar, S.; Ma, X.; Homayoon, Z.; Barnes, G. L.; Hase, W. L. Direct Chemical Dynamics Simulations. *J. Am. Chem. Soc.* **2017**, *139*, 3570–3590.

(35) Taketsugu, T.; Gordon, M. S. Dynamic Reaction Path Analysis Based on an Intrinsic Reaction Coordinate. *J. Chem. Phys.* **1995**, *103*, 10042–10049.

(36) Haruta, M. Gold Rush. *Nature* **2005**, *437*, 1098–1099.

(37) Gao, M.; Lyalin, A.; Takagi, M.; Maeda, S.; Taketsugu, T. Reactivity of Gold Clusters in the Regime of Structural Fluxionality. *J. Phys. Chem. C* **2015**, *119*, 11120–11130.

(38) Xu, S.; Zhang, Y.; Wei, Y.; Tian, G. Ground and Excited State Geometrical and Optical Properties of Au (n = 2–13) Nanoclusters: A First-Principles Study. *Comput. Theor. Chem.* **2020**, *1190*, 113007.

(39) Hare, S. R.; Bratholm, L. A.; Glowacki, D. R.; Carpenter, B. K. Low Dimensional Representations along Intrinsic Reaction Coordinates and Molecular Dynamics Trajectories Using Interatomic Distance Matrices. *Chem. Sci.* **2019**, *10*, 9954–9968.

(40) Tsutsumi, T.; Ono, Y.; Arai, Z.; Taketsugu, T. Visualization of the Intrinsic Reaction Coordinate and Global Reaction Route Map by Classical Multidimensional Scaling. *J. Chem. Theory Comput.* **2018**, *14*, 4263–4270.

Chapter 4

Projection of Dynamical Reaction Route onto Reduced-dimensionality Reaction Space

4.1 Introduction

The intrinsic reaction coordinate (IRC) is defined as the steepest descent path in mass-weighted coordinates, which connects two minima (MINs) *via* one transition state (TS) on a potential energy surface (PES).[1] A variation of geometrical structures along the IRC provides an intuitive picture of a chemical reaction process. In the last decade, Ohno and Maeda proposed automated reaction path search methods, the anharmonic downward distortion following (ADDF) and the artificial force induced reaction (AFIR),[2,3] and those methods enable us to construct a global reaction route map composing of all IRC paths for a given molecular system.

From the viewpoint of dynamics, it is well-known that a molecule is pushed off the IRC path around a highly-curved region due to a centrifugal force leading to the excitation of the transverse vibrational modes.[4–6] Also, when the potential valley along the IRC path bifurcates into several valleys due to the IRC instability, a molecule undergoes a bifurcation reaction yielding several different products.[7–9] Such dynamics effects can be examined by the on-the-fly molecular dynamics (MD) approach,[10–14] where atomic positions and velocities are evolved by Newton's equation of motion based on the atomic forces determined from quantum chemical calculations. On-the-fly trajectories explore the PES with a given energy, and the route is not restricted to the IRC paths; they can reach several different isomer structures or dissociative products. To clarify the dynamic reaction routes, as shown in **Chapter 2**, I proposed a trajectory mapping method on the basis of a global reaction path network, and it was applied to structural transformations of a small gold cluster; I investigated dynamics features for trajectory ensembles such as IRC-jump behaviors.[12] Recently, several trajectory mapping approaches were also proposed for various purposes.[13,14]

In order to combine the global reaction route network and the molecular dynamics analysis, it is necessary to construct the reference reaction space where molecular structures in both the static reaction routes and the dynamics routes are appropriately arranged. In such a reference map, similar structures should be located close to each other, while different structures should be located far away. A classical multidimensional scaling (CMDS) technique enables us to arrange each molecular structure properly and leads to the concept of the global reaction path "*map*." Recently, Li *et al.* employed the CMDS method to analyze trajectories obtained by the surface-hopping nonadiabatic on-the-fly dynamics simulation.[15] In **Chapter 3**, I employed the CMDS method to visualize the three target reactions into a reduced-dimensionality reaction space: the IRC paths for an intramolecular proton transfer in malonaldehyde, the IRC of the collision reaction, OH^- + CH_3F → $[CH_3OH\cdots F]^-$, and the global reaction path network for a small gold cluster.[16]

Projecting on-the-fly trajectories onto the reduced-dimensionality reaction space allows us to analyze dynamical reaction mechanisms based on the static reaction map.

Such a procedure was formulated by Trosset and Priebe, and their "*out-of-sample extensions*" of CMDS (oCMDS) can embed new data into the pre-defined subspace.[17] In biochemistry, oCMDS was applied to a classification of protein conformers, and they embedded classical trajectories into the CMDS configurational space determined by five crystal structures corresponding to typical conformers.[18] In this chapter, I examine the dynamical reaction routes in the subspace determined by the IRC path and the global reaction path map, using the on-the-fly MD simulations and oCMDS analysis. I also demonstrate the usefulness of the oCMDS analysis through applications to the collision reaction, $OH^- + CH_3F$,[10,16,19] and the structural transformation of a small gold cluster.[9,12]

4.2 Out-of-sample extension of Classical Multidimensional Scaling

In this section, the CMDS procedure for the reference structures on the IRC is described briefly, and then, the oCMDS approach is introduced to project on-the-fly trajectories into the reduced-dimensional subspace. The detailed procedures are introduced in **Chapter 3**[16] and several literature[20–22].

A geometrical structure of *N*-atomic molecule can be represented by 3*N* mass-weighted Cartesian coordinates, ξ, where the origin of the coordinate axes is taken at the center of mass. The difference between two structures, $\xi^{(i)}$ and $\xi^{(j)}$, can be measured by the Euclid distance defined as,

$$d_{ij} = \sqrt{\sum_{k}^{3N} \left(\xi_k^{(i)} - \xi_k^{(j)}\right)^2} = \left|\xi^{(i)} - \xi^{(j)}\right|, \tag{4-1}$$

where $\xi_k^{(i)}$ denotes the *k*th coordinate of the *i*th structure. For a pair of molecular geometries, $\xi^{(i)}$ and $\xi^{(j)}$, the orientation of x-y-z coordinate axes should be determined to minimize d_{ij}, and this alignment is conducted by the Kabsch algorithm.[23,24] As the related approach, in **Chapter 2**, I proposed the trajectory mapping method that describes the dynamical reaction paths based on the distance functions between the points on the trajectory and the reference structures taken over the static reaction path network.[12]

Here, I pick up *n* reference structures along the IRC and employ the CMDS method to determine the reduced-dimensionality subspace. The CMDS procedure consists of four steps:

1) Prepare a distance matrix $\mathbf{D}$ where *ij*th element is $d_{ij}\ (i, j = 1, \cdots, n)$.

2) Apply the Young-Householder transformation (double centering)[25] to a squared distance matrix $\mathbf{D}_{ij}^{(2)} = d_{ij}^2$ to get an inner product matrix $\mathbf{Q}$.

$$\mathbf{Q} = -\frac{1}{2}\left(\mathbf{E} - \frac{1}{n}\mathbf{1}\right)\mathbf{D}^{(2)}\left(\mathbf{E} - \frac{1}{n}\mathbf{1}\right)^T \tag{4-2}$$

Here, $\mathbf{E}$ is a unit matrix and $\mathbf{1}$ is a square matrix with all elements as 1.

3) Diagonalize the inner product matrix $\mathbf{Q}$, and then eigenvalues $\{\lambda_1, \cdots, \lambda_n\}$ and the corresponding eigenvectors $\{L_1, \cdots, L_n\}$ are ordered in a descending way of the eigenvalues $(\lambda_1 \geq \lambda_2 \cdots \geq \lambda_n)$.

4) Take *p* largest eigenvalues $\{\lambda_1, \cdots, \lambda_p\}$ with the corresponding eigenvectors $\{L_1, \cdots, L_p\}$, and generate principal coordinates $\mathbf{Y}_a = \mathbf{L}_a\sqrt{\lambda_a} \quad (1 \leq a \leq p)$.

The contribution of the respective principal coordinate to represent the relative positions of the reference structures is measured by the proportion Λ_a defined as[21]

$$\Lambda_a = \frac{\lambda_a}{\sum_c^b \lambda_c}, \tag{4-3}$$

where *b* is the number of nonnegative eigenvalues of λ_c. The representability in the reduced dimensional subspace spanned by $\{\mathbf{Y}_1, \cdots, \mathbf{Y}_p\}$ can be evaluated by the cumulated proportion Λ,[21]

$$\Lambda = \frac{\sum_c^p \lambda_c}{\sum_c^b \lambda_c}. \tag{4-4}$$

When Λ is close to 1, the relative positions for all reference structures are almost kept in a p-dimensional principal coordinate space.

In the oCMDS method, out-of-sample data are projected on the p-dimensional CMDS coordinate space. To illustrate the procedure of the oCMDS method, I introduce distance matrices, $\mathbf{D}_{n\times n}$, $\mathbf{D}_{n\times m}$, and $\mathbf{D}_{m\times m}$, for the reference structures and out-of-sample structures where n and m denote the number of the reference structures and out-of-sample structures, respectively. Then, the squared distance matrix $\mathbf{A}$ involving $\mathbf{D}^{(2)}_{n\times n}$, $\mathbf{D}^{(2)}_{n\times m}$, and $\mathbf{D}^{(2)}_{m\times m}$ is defined as

$$\mathbf{A} \equiv \begin{pmatrix} \mathbf{D}^{(2)}_{n\times n} & \mathbf{D}^{(2)}_{n\times m} \\ \mathbf{D}^{(2)}_{m\times n} & \mathbf{D}^{(2)}_{m\times m} \end{pmatrix} \tag{4-5}$$

where $\mathbf{D}^{(2)}_{m\times n}$ denotes a transposed matrix of $\mathbf{D}^{(2)}_{n\times m}$. Next, a double centering is carried out for $\mathbf{A}$ following the Trosset formula,[17]

$$\mathbf{B} = \tau_{\mathbf{w}}\left(\mathbf{A}\right) = -\frac{1}{2}\left(\mathbf{E} - \frac{\mathbf{e}\cdot\mathbf{w}^T}{n}\right)\mathbf{A}\left(\mathbf{E} - \frac{\mathbf{e}\cdot\mathbf{w}^T}{n}\right)^T, \tag{4-6}$$

where $\mathbf{E}$ is a unit matrix, $\mathbf{e}$ is a column vector of $n + m$ dimension with all elements as 1, and $\mathbf{w}$ is a column vector of $n + m$ dimension with 1 (first n components) and 0 (remaining m components). In fact, through equation (4-6), the Young-Householder transformation[25] is applied to $\mathbf{D}^{(2)}_{n\times n}$ concerned with the original data set. The out-of-sample problem to obtain p-dimensional coordinates $\mathbf{X}_{(n+m)\times p}$ for out-of-sample structures is now solved by minimization of the following function,[17]

$$\min\left\|\mathbf{B}-\mathbf{X}\mathbf{X}^T\right\|^2=\min\left\|\begin{pmatrix}\mathbf{B}_{n\times n}-\mathbf{Y}\mathbf{Y}^T & \mathbf{B}_{n\times m}-\mathbf{Y}\mathbf{Z}^T\\ \mathbf{B}_{m\times n}-\mathbf{Z}\mathbf{Y}^T & \mathbf{B}_{m\times m}-\mathbf{Z}\mathbf{Z}^T\end{pmatrix}\right\|^2, \tag{4-7}$$

where $\mathbf{B}_{n\times n}$, $\mathbf{B}_{n\times m}$, $\mathbf{B}_{m\times n}$, and $\mathbf{B}_{m\times m}$ are a part of the inner matrix of $\mathbf{B}$ with $n + m$ dimension. **X** denotes p-dimensional coordinates as

$$\mathbf{X}=\mathbf{X}_{(n+m)\times p}\equiv\begin{pmatrix}\mathbf{Y}_{n\times p}\\ \mathbf{Z}_{m\times p}\end{pmatrix} \tag{4-8}$$

where $\mathbf{Y}_{n\times p}$ and $\mathbf{Z}_{m\times p}$ are coordinates for n reference structures and m out-of-sample structures, respectively. Note that $\mathbf{Y}$ means the principal coordinates obtained by the CMDS method. Hence, variables for optimization in equation (4-7) are only elements of $\mathbf{Z}_{m\times p}$, and the principal coordinates can be determined for out-of-sample structures in the p-dimensional CMDS subspace. The CMDS and oCMDS method is implemented in the SPPR program,[26] and, now, the out-of-sample data are projected one by one onto the fixed p-dimensional CMDS subspace.

4.3 Results and Discussion

4.3.1 Collision Reaction of $OH^- + CH_3F \rightarrow [CH_3OH\cdots F]^-$

As the first target reaction, I chose the collision reaction, $OH^- + CH_3F$. First, the IRC was calculated for this reaction at the MP2/6-31+G* level, and the CMDS method was employed for 101 reference structures taken along the IRC path. Then, the on-the-fly MD simulation was carried out at the same computational level, starting from the TS region. As the initial conditions, normal coordinates and conjugate momenta were determined randomly around the TS structure following the Boltzmann distribution at 300 K, and 50 trajectories that proceed from the TS to the product region were obtained. The time step was taken as 0.1 fs, and the respective trajectories were run over 1 ps until the C-F interatomic distance reaches 8 Å, or until the distance function between the point on the trajectory and the product structure, P, reaches 5 Å amu$^{1/2}$. Lastly, the oCMDS method was employed to project on-the-fly trajectories into the two-dimensional subspace determined for the IRC path by the CMDS method. The electronic structure calculations were performed by the GAMESS program,[27] and the on-the-fly MD simulations were performed by the SPPR program.[26]

For the *N*-atomic molecule, the IRC is regarded as a one-dimensional curved pathway in 3*N*–6 dimensional coordinate space. The reaction path tangent vector **v** for the IRC is defined as

$$\mathbf{v}(s) = \frac{d\xi^{\mathrm{IRC}}(s)}{ds}, \tag{4-9}$$

where s denotes a reaction coordinate and $\xi^{\mathrm{IRC}}(s)$ denotes the mass-weighted Cartesian coordinates of the structure at s on the IRC. A curvature vector $\mathbf{v}'(s)$ and the corresponding scalar curvature $\kappa(s)$ are defined as

$$\mathbf{v}'(s) = \frac{d\mathbf{v}(s)}{ds} = \frac{d^2\xi^{\mathrm{IRC}}(s)}{ds^2}, \tag{4-10}$$

$$\kappa(s) = \left|\mathbf{v}'(s)\right|. \tag{4-11}$$

The curvature vector along the reaction path can be calculated by numerical differentiation of the reaction path tangent vector, and the scalar curvature is defined as the norm of the curvature vector.[5] **Figure 4.1a** shows variations of the energy (black dots) along the IRC for the reaction, $OH^- + CH_3F \rightarrow [CH_3OH\cdots F]^-$, and the scalar curvature (red dots) from TS to P, where A (s = 1.74 Å amu$^{1/2}$) and B (s = 5.36 Å amu$^{1/2}$) correspond to the structures at the maximum of the scalar curvature. Geometrical changes along the IRC indicate that (1) F^- first attempts to dissociate from CH_3 until reaching the structure A, (2) F^- starts to roam around CH_3OH moiety (from A to B), and (3) a hydrogen-bonded structure is formed with an internal rotation of CH_3 fragment, which corresponds to the IRC terminal (from B to P). The sharp path curvature around A suggests a possible energy transfer between the C-F bond dissociation mode and F^- roaming mode.

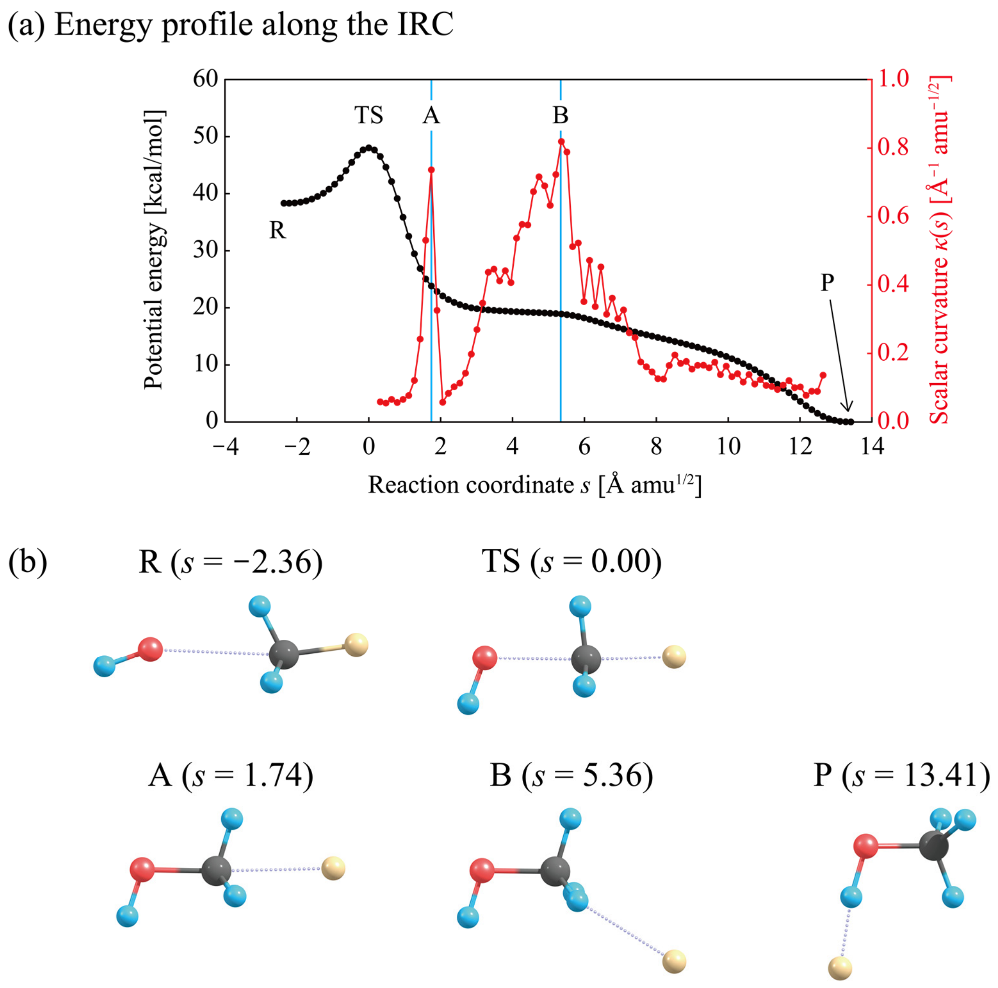

(a) Energy profile along the IRC

(b) R (s = −2.36) TS (s = 0.00)

A (s = 1.74) B (s = 5.36) P (s = 13.41)

Figure 4.1. (a) The energy profile (black dots in kcal/mol) along the IRC for the reaction, $OH^- + CH_3F \rightarrow [CH_3OH\cdots F]^-$, and the scalar curvature $\kappa(s)$ (red dots in $Å^{-1}$ $amu^{-1/2}$) from TS to the product structure. (b) Geometrical structures of reactant (R), TS, two highly-curved regions (A and B), and product (P) are also shown.

In the same way as **Chapter 3**, I employed the CMDS method to visualize the IRC path for $OH^{-} + CH_3F \rightarrow [CH_3OH\cdots F]^{-}$ in a reduced-dimensionality subspace. In the present computations, 101 geometries along the IRC were picked up as the reference structure, and the distance matrix $\mathbf{D}$ was generated for these reference structures by calculating pairwise distances defined in equation (4-1). Following steps 2 ~ 4 in Section 4.2, the principal coordinates (denoted by PCo) were determined to represent the IRC path in a reduced-dimensional subspace. **Figure 4.2** shows the IRC path in the two-dimensional principal coordinates, PCo1 and PCo2. The proportions for each principal coordinate are $\Lambda_1 = 0.819$ and $\Lambda_2 = 0.134$, respectively, and the cumulated proportion Λ for these two-dimensions is 0.953, indicating that most geometrical information of the IRC path is represented in this two-dimensional subspace. In this reaction space, I denote the reactant (R), the transition state (TS), the highly-curvature points (A, B), and the product (P) as a square, a circle, pentangles, and a square, respectively. Similar to the physical interpretations for PCo1 and PCo2 as mentioned in **Chapter 3**, PCo1 correlates with an O-C-F bond angle (related to F^{-} roaming) while PCo2 correlates with a C-F interatomic distance (related to C-F dissociation).[16] The visualized reaction path in Figure 4.2 is highly curved around B rather than around A. This nature is consistent with the scalar curvature behavior in Figure 4.1 that the scalar curvatures around B gradually increase wider region than around A.

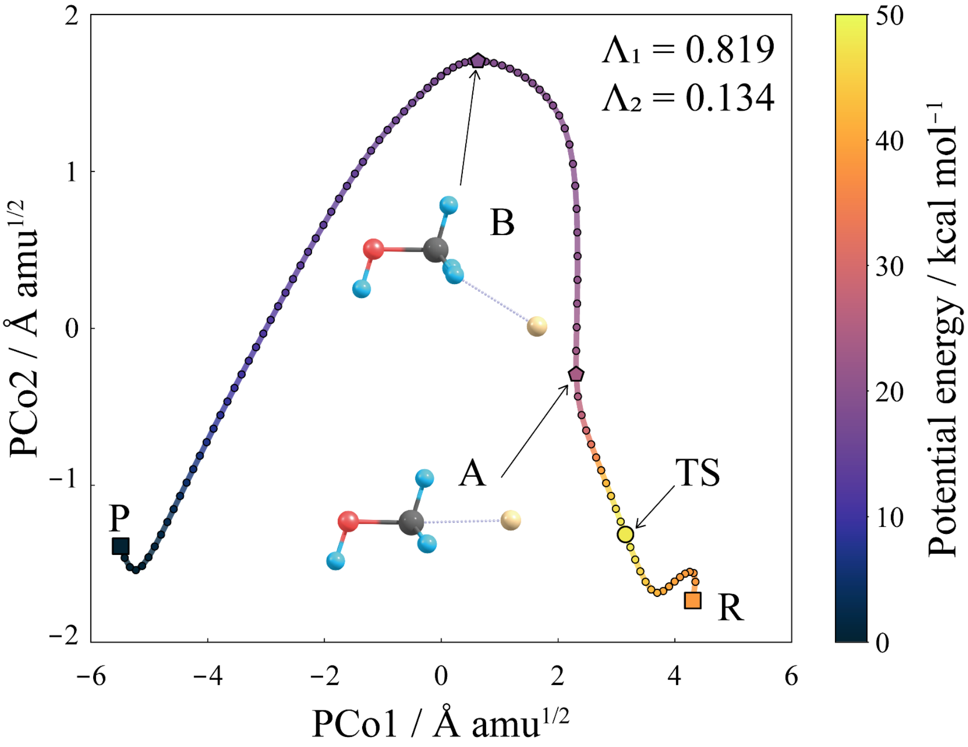

Figure 4.2. The IRC for $OH^- + CH_3F \rightarrow [CH_3OH\cdots F]^-$ projected to the two-dimensional principal coordinate subspace. R, TS, and P denote the reactant, transition state, and product, respectively, while A and B denote the points with a maximum of the reaction path curvature. The color shows the potential energy relative to the energy of P.

Next, I turn to the discussion of dynamic aspects on the basis of on-the-fly trajectories. Hase and coworkers reported a pioneering work for this S_N2 reaction to demonstrate the significance of non-IRC path by on-the-fly MD simulations at the MP2 level, where only 10% of trajectories reach the terminal of the IRC path, $[CH_3OH\cdots F]^-$, while 90% of trajectories lead to the dissociated products, $CH_3OH + F^-$.[10] They concluded that such non-IRC paths originate from the inefficient intramolecular vibrational energy distribution (IVR), resulting in the energy release to the relative translational motion of

CH_3OH and F^- rather than the O-C---F^- bending mode.[10] In the present on-the-fly MD simulations at the same MP2 level, 50 trajectories were run from the TS toward the product side, where 11 trajectories proceed near the IRC while 39 trajectories lead to the dissociation of F^- from CH_3OH. Among the 39 trajectories leading to $CH_3OH + F^-$, two trajectories show a return of F^- to the moiety of CH_3OH, making a complex of $[CH_3OH \cdots F]^-$ near the structures A and B.

Following the previously proposed procedure as summarized in **Chapter 2**, I calculated distance functions between all points along the obtained trajectories and the five reference structures (R, TS, A, B, and P). **Figure 4.3** shows changes of the distance functions for (a) a typical trajectory proceeding near the IRC, (b) a typical trajectory leading to $CH_3OH + F^-$, and (c) a typical trajectory where F^- leaves once and comes back to the CH_3OH moiety. Figure 4.3a indicates that the trajectory proceeds along the IRC as TS → A → B → P (the closest reference structure exchanges in this order), which was terminated at 346.9 fs when the distance function from P reached within 5 Å amu$^{1/2}$. In the case of Figure 4.3b and c, the trajectories depart from the IRC around B in the initial stage, suggesting that they cannot follow the IRC path and then proceed to the non-IRC channel of C-F dissociation due to an inertial force by the highly-curved reaction path. Such non-IRC behaviors support the inefficient IVR around the highly-curved region claimed in the previous study[10]. In Figure 4.3b, the C-F interatomic distance reaches 8 Å at 279.2 fs, while in Figure 4.3c, F^- could not escape from CH_3OH moiety and finally returns to A at 740.0 fs due to electrostatic interaction. Figure 4.3 provides fruitful information on the sequential dynamical reaction routes based on the reference structures; however, the detailed understandings require in-depth knowledge of the chemical reaction system.

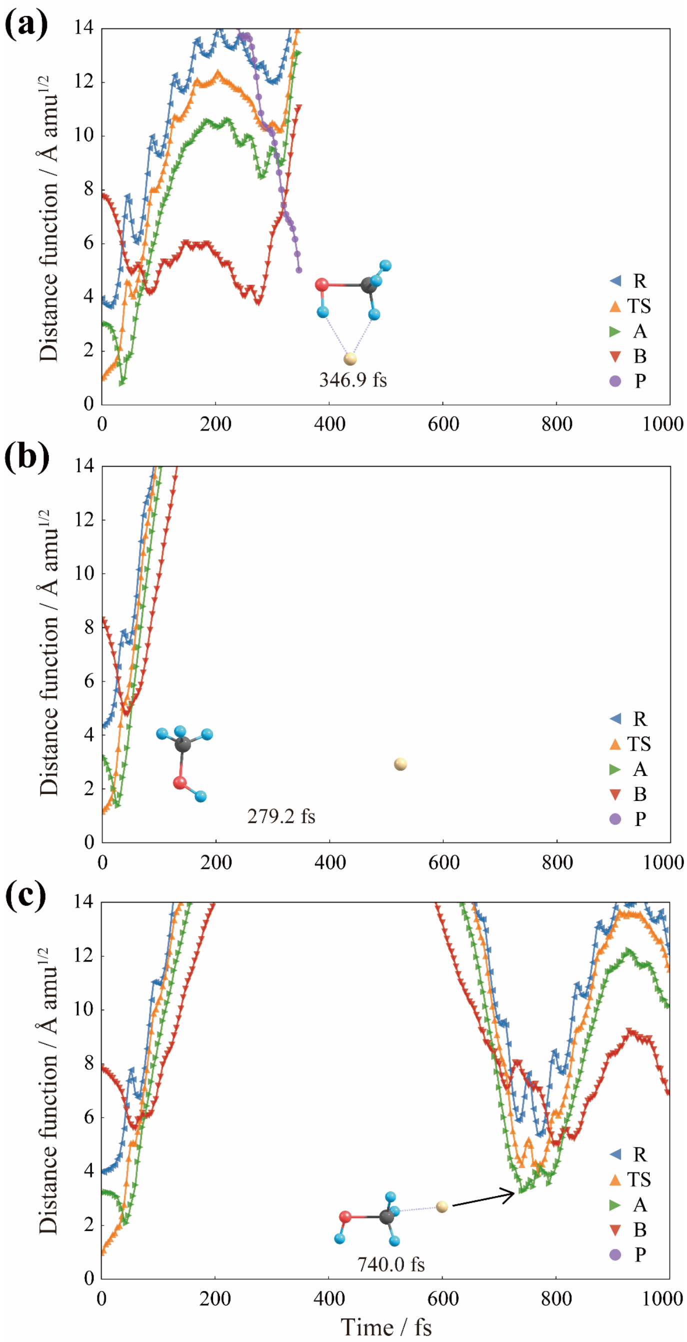

Figure 4.3. Variations of the distance functions from the reference structures, R, TS, A, B, and P, for (a) a typical trajectory proceeding near the IRC, (b) a typical trajectory leading to $CH_3OH + F^-$, and (c) a typical trajectory where F^- leaves once and comes back to the CH_3OH moiety.

Here, I perform the oCMDS procedure to map on-the-fly trajectories into the two-dimensional subspace determined by the molecular structures along the IRC. In this chapter, the out-of-sample data is the molecular structures along the trajectories, and the principal coordinates (PCos) are determined by optimizing equation (4-7) using a modified Powell algorithm[28] for each out-of-sample structure. **Figure 4.4** shows three different types of trajectories projected on the two-dimensional subspace, corresponding to three trajectories as shown in Figures 4.3a, b, and c: (a) a trajectory proceeding near the IRC, (b) a trajectory leading to $CH_3OH + F^-$, and (c) a trajectory where F^- leaves once and comes back to the CH_3OH moiety. Figure 4.4a shows that the molecule starting from TS attempts to depart from the IRC around the highly-curved region of B, but it comes back to the IRC path due to the attracting force from the IRC valley and finally enters the region around P. In Figure 4.4b, the molecular system mostly departs from the highly-curved region around B, and F^- leaves from a moiety of CH_3OH. In Figure 4.4c, the molecular system attempts to depart from the region around B, but it comes back to the region around A. The difference between Figure 4.4b and Figure 4.4c probably originate from the energy distribution of F^- and CH_3O at the highly-curved region around B, suggesting that the B region works as a bifurcation point in a dynamic sense. Consequently, projecting the dynamical reaction route on the reduced-dimensionality reaction space clarifies that the centrifugal force due to a highly-curved IRC pushes the molecule in the direction orthogonal to the IRC, promoting major trajectories departing from the IRC (leading to the $CH_3OH + F^-$ dissociation) and preventing minor trajectories return to the IRC (leading to the complex of $CH_3OH\cdots F^-$).

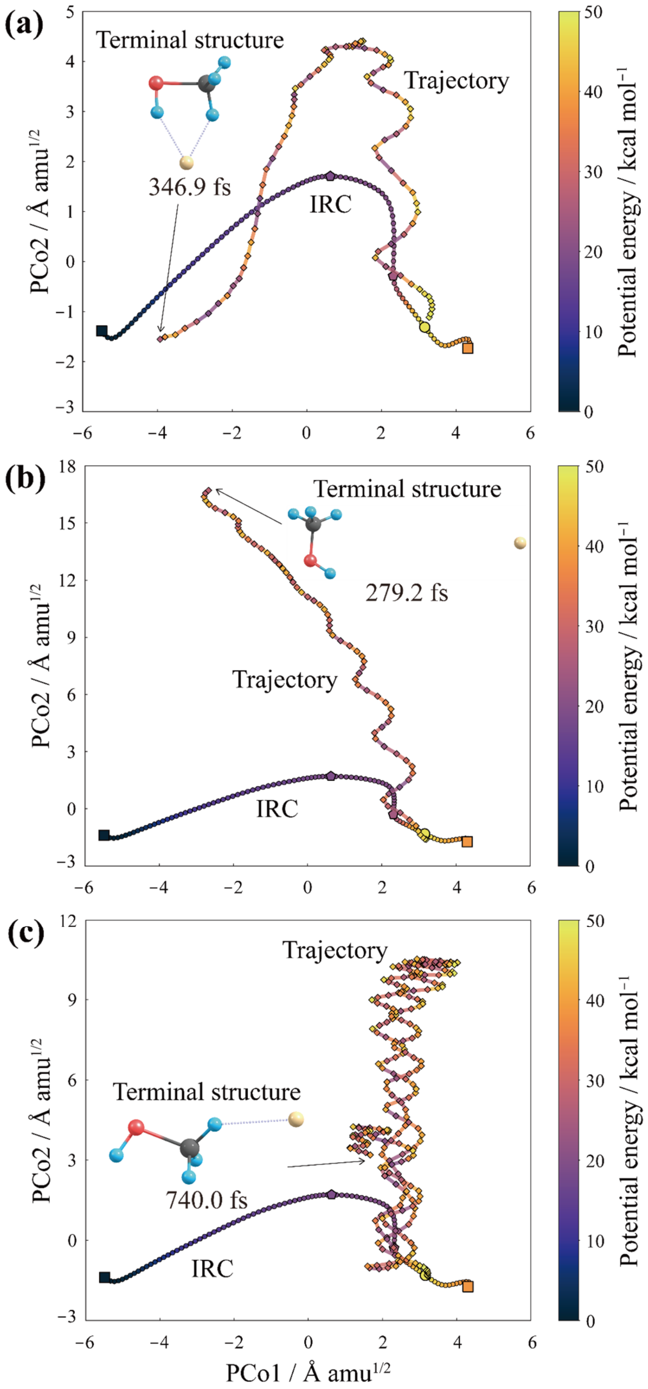

Figure 4.4. The trajectories projected to the two-dimensional subspace determined for the IRC path: (a) a trajectory which proceeds near the IRC and reaches the region around P; (b) a trajectory which departs from the IRC at a highly-curved region; (c) a trajectory which could not escape from the IRC due to the attraction force from the IRC. The color on the IRC and trajectories denotes the potential energy values.

4.3.2 Global Reaction Route Map of Au_5 Cluster

As the second application, I apply oCMDS to the isomerization reaction of the Au_5 cluster that was reported previously by ADDF (in **Chapter 2**),[9] on-the-fly MD (in **Chapter 2**),[12] and CMDS (in **Chapter 3**).[16] **Figure 4.5** shows the molecular structures involved in the global reaction path network of the Au_5 cluster, which has five MINs and 14 TSs at the PBE/LanL2DZ level.[9] **Chapter 2** performed on-the-fly MD simulations at the PBE/LanL2DZ level to elucidate dynamical reaction mechanisms, including the isomerization and the bifurcation reactions, and 200 trajectories from TS1-1d were analyzed by the distance functions.[12] In **Chapter 3**, I applied CMDS to all MINs and TSs involved in the global reaction path network of Au_5 and visualized these structures onto the two-dimensional principal coordinate subspace.[16] In this chapter, I reuse the global reaction path network and the on-the-fly trajectories from TS1-1d at the PBE/LanL2DZ level and employ CMDS to visualize the global reaction path map involved both all stationary points and the molecular structures along the IRCs. Then, I also project the reused trajectories from TS1-1d onto the principal coordinate subspace determined by the IRC network to clarify the dynamic reaction routes.

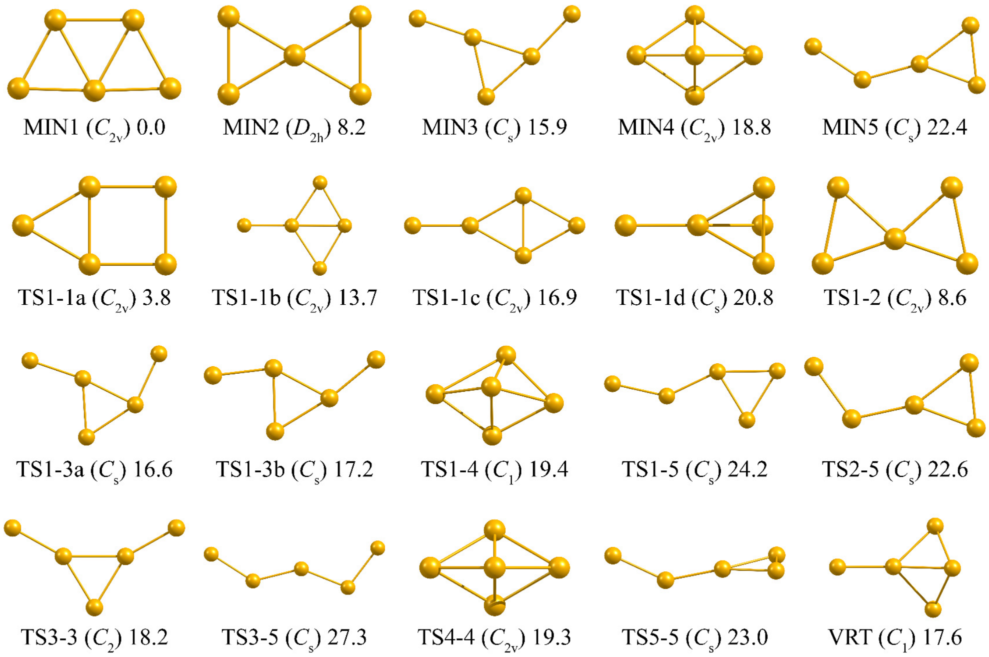
MIN1 (C_{2v}) 0.0 MIN2 (D_{2h}) 8.2 MIN3 (C_s) 15.9 MIN4 (C_{2v}) 18.8 MIN5 (C_s) 22.4

TS1-1a (C_{2v}) 3.8 TS1-1b (C_{2v}) 13.7 TS1-1c (C_{2v}) 16.9 TS1-1d (C_s) 20.8 TS1-2 (C_{2v}) 8.6

TS1-3a (C_s) 16.6 TS1-3b (C_s) 17.2 TS1-4 (C_1) 19.4 TS1-5 (C_s) 24.2 TS2-5 (C_s) 22.6

TS3-3 (C_2) 18.2 TS3-5 (C_s) 27.3 TS4-4 (C_{2v}) 19.3 TS5-5 (C_s) 23.0 VRT (C_1) 17.6

Figure 4.5. All minima, TS structures, and one VRT structure near TS1-1b for Au_5 calculated by PBE/LanL2DZ.[9] The point group and relative energy (in kcal/mol) are also given for each structure.

First, I examine the bifurcation reaction related to VRT located on the IRC starting from TS1-1d to MIN1. As mentioned in **Chapter 2**, three NPI isomers of TS1-1d are located very closely (denoted by TS1-1d, TS1-1d', and TS1-1d"), and three IRC paths from the respective TS1-1d connect two NPI isomers of MIN1 (denoted by MIN1 and MIN1', MIN1" and MIN1"", and MIN1"' and MIN1""', respectively). The previous study reported that VRT has the corresponding transition state, TS1-1b,[9] which also connects two NPI isomers of MIN1 (MIN1–TS1-1b–MIN1", MIN1""–TS1-1b'–MIN1""', and MIN1'–TS1-1b"–MIN1"'). Because the NPI isomers of TS1-1b connect the product following the original IRC and the bifurcation product yielded from the bifurcation reaction, to discuss the bifurcation mechanisms starting from TS1-1d, I should consider three IRCs starting from TS1-1d, TS1-1d', and TS1-1d'' and three IRCs starting from TS1-1b, TS1-1b', and TS1-1b'' (in total, 387 structures). Thus, I selected the molecular structures along six IRCs as the reference structures to determine the reduced-dimensionality reaction space. **Figure 4.6a** shows six IRCs projected on the two-dimensional principal coordinate subspace spanned by PCo1 and PCo2, where circles, squares, diamonds, and smaller circles denote MINs, TSs, VRTs, and IRC points, respectively. The proportions of PCo1 and PCo2 are the same value, 0.365, suggesting that these two principal coordinates belong to a doubly-degenerate symmetry representation. Although the cumulative proportion for the two principal coordinates is 0.730, three IRCs for NPI isomers of TS1-1b are not clearly illustrated. To construct the well-defined reduced-dimensionality bifurcation reaction space, I chose the partial reference structures from the pre-defined reference structures as follows: two sides of IRCs from TS1-1d (TS1-1d') to MIN1 (MIN1'') and one IRC starting from TS1-1b (connecting MIN1 and MIN1''), in total, 130 structures. Figure 4.6b shows the partial IRCs projected on the two-dimensional subspace. The proportions for PCo1 and PCo2 are $\Lambda_1 = 0.528$ and $\Lambda_2 = 0.432$, and the cumulated proportion is 0.960. This result indicates that almost all configurational information is represented in a two-dimensional subspace.

To elucidate the dynamical bifurcation mechanisms, I projected two fascinating trajectories departing from TS1-1d onto the two-dimensional principal coordinate subspace (Figure 4.6b). Figure 4.6c shows that the trajectory undergoes the IRC-jump process, which is introduced in **Chapter 2**, before VRT and finally reaches MIN1''. Such a dynamical reaction route corresponds to the conventional bifurcation mechanism, indicating that the PES shape orthogonal to the reaction coordinate gets close to flat. In contrast, Figure 4.6d shows that the trajectory initially moves to the side of TS1-1d' by the IRC-jump behavior, but it returns to the original IRC through VRT", finally reaching MIN1. Such a process does not produce the bifurcation product (MIN1") even though the trajectory crosses through the VRT region. This complicated mechanism is first recognized by combining the NPI concept and the IRC-jump behavior. Through the above discussion, the reduced-dimensionality strategy uncovers that the IRC-jump behaviors determine the fate of the product regions that the trajectories will reach.

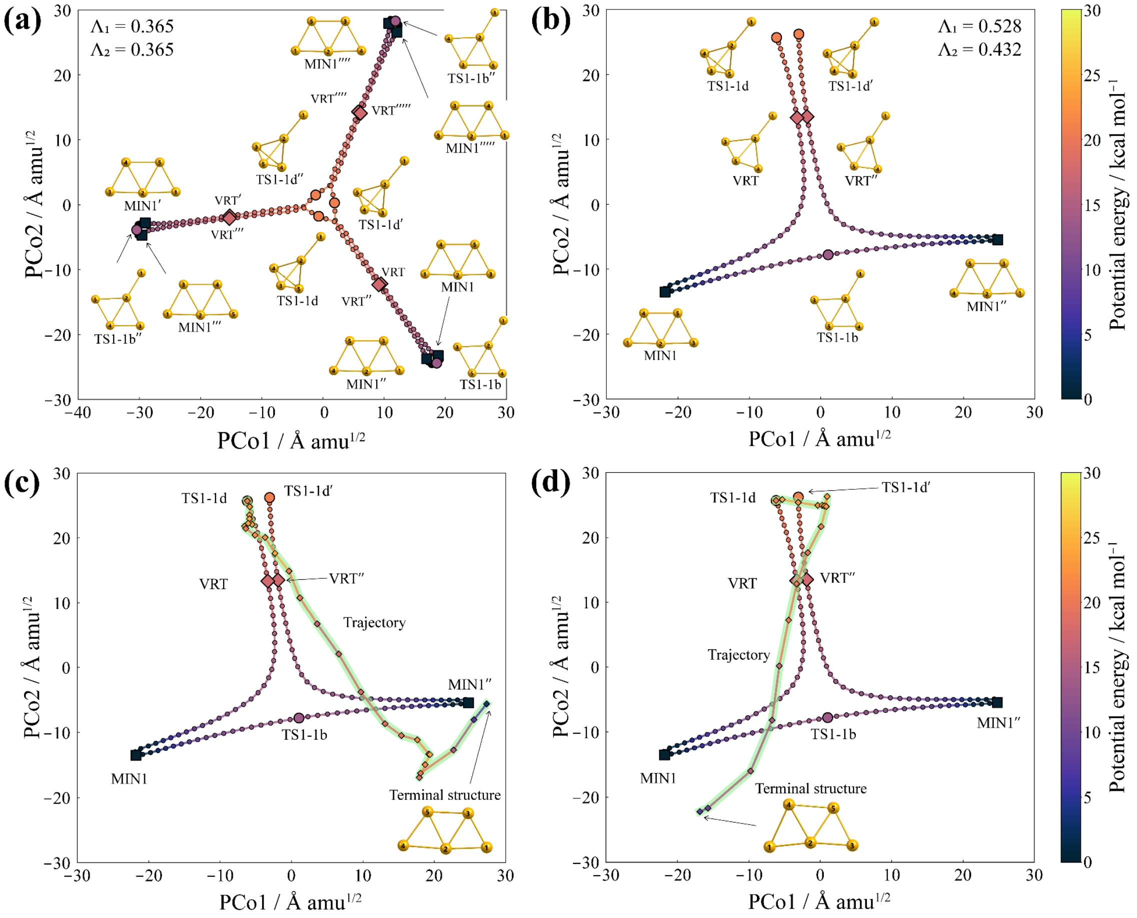

Figure 4.6. The IRCs and the on-the-fly trajectories for Au_5 structural transformation projected on the two-dimensional principal coordinate subspace determined by CMDS and oCMDS analyses without the merged-NPI option. Circles, squares, and diamonds denote TSs, MINs, and VRT, and smaller circles and smaller diamonds denote the structures along the IRCs and trajectories (highlighted by light green). The colormap shows the potential energy relative to the energy of MIN1. (a) Three IRCs for MIN1–TS1-1d–MIN1 and three IRCs for MIN1–TS1-1b–MIN1; (b) Two sides of IRCs for TS1-1d–MIN1 and one IRC for MIN1–TS1-1b–MIN1; (c, d) on-the-fly trajectories projected on the two-dimensional principal coordinate subspace (b).

Here, I move to the discussion on the isomerization reaction of Au_5 based on the reduced-dimensionality reaction space determined by the static reaction path network with the merged-NPI option as introduced in **Chapter 2**. In **Chapter 3**, I generated the two-dimensional principal coordinate subspace that involved 19 stationary points (five MINs and 14 TSs) of Au_5. **Figure 4.7a** corresponds to this two-dimensional subspace, where five MINs and 14 TSs are denoted by circles and squares and are connected by straight black lines. In this section, I added further structures along the 14 IRCs to the reference structures (in total, 336 reference structures) and carried out CMDS analysis to determine the two-dimensional principal coordinates (Figure 4.7b). In comparison with Figure 4.7a, Figure 4.7b shows almost the same stationary-point configurations and proportions despite the increase in so many reference structures. In Figure 4.7b, the cumulated proportion for two principal coordinates is 0.642, and the IRC profiles toward MIN2, MIN3, MIN4, and MIN5 are well described, but the IRCs around MIN1 are ambiguous.

To zoom in the low-energy region around MIN1, I picked up seven IRCs connected with MIN1 (passing TS1-1a, TS1-1b, TS1-1c, TS1-1d, TS1-2, TS1-3a, or TS1-3b) and again carried out CMDS analysis for those reference structures (in total, 260 structures). The results are shown in Figure 4.7c (in two-dimension) and Figure 4.7d (in three-dimension). The proportions for three principal coordinates are $\Lambda_1 = 0.385$, $\Lambda_2 = 0.269$, and $\Lambda_3 = 0.153$, and thus, the cumulated proportions for two- and three-dimensional map are 0.654 and 0.807, respectively. In comparison with Figure 4.7b, Figure 4.7c clearly represents the IRC network structure in the low-energy region. Moreover, considering the third principal coordinate, PCo3, clarifies the IRC network structure in more detail, as shown in Figure 4.7d. This result argues that one can define a more appropriate reduced-dimensionality principal coordinate subspace for the target reaction by designing the reference structures.

Finally, I focus on the dynamic reaction routes along the on-the-fly trajectories on the basis of the reduced-dimensionality map. In **Chapter 2**, by using the on-the-fly trajectory mapping method, I verified that, among 200 trajectories starting from TS1-1d toward MIN1, 62 trajectories initially approached TS1-3a before reaching MIN1.[12] To examine these reaction dynamics, I chose the typical trajectory approaching TS1-3a and projected it into the two-dimensional subspace (Figure 4.7c) and the three-dimensional subspace (Figure 4.7d) by the oCMDS approach. Because the IRC paths join around the neighborhood of minimum due to the PES geometry, several IRCs join near MIN1 in Figure 4.7c; however, some of the joined-IRCs separate each other by PCo3 in Figure 4.7d. Figure 4.7c shows that the trajectory proceeds along the IRC part from TS1-1d to TS1-1b, indicating that it deviates from the IRC and approaches to TS1-3a region. After that, it wanders around TS1-3a and finally approaches MIN1. Figure 4.7d shows the dynamic reaction route in the three-dimensional subspace. In this figure, MIN3, TS1-3a, TS1-3b, MIN2, TS1-2, and TS1-1b are located in the negative PCo3 region, and the trajectory seems to leave the IRC after passing VRT and then approaching TS1-3a. Later, it returns to the original IRC and finally reaching MIN1 *via* TS1-1a region. From these results, it is found that due to the excitation of vibrational modes orthogonal to the reaction coordinate, the molecule can switch from the IRC valley to another IRC related to TS1-3a through the IRC-jump behavior and finally comes back to the original IRC. The dimensionality-reduction-based approach enables us to elucidate the dynamic reaction routes and the driving force, which is difficult to grasp by the conventional reaction-dynamics analyses, based on both aspects of reaction dynamics analysis and static reaction path analysis.[29]

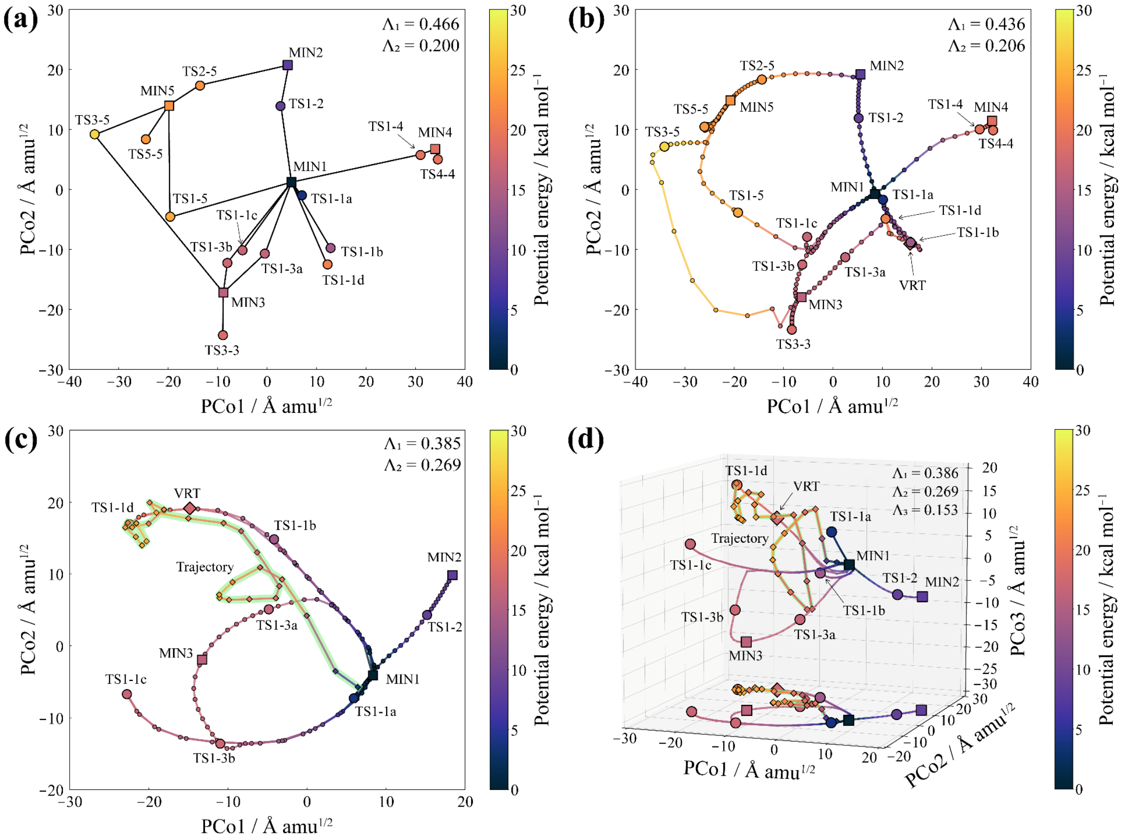

Figure 4.7. The two-dimensional principal coordinate subspace of Au_5 determined by CMDS: (a) 19 reference structures involving five MINs and 14 TSs and (b) 336 reference structures along the 14 IRCs. The typical on-the-fly trajectory projected onto the zoomed two- or three-dimensional principal coordinate subspace, which involves 260 reference structures along the seven IRCs, by oCMDS: (c) in two-dimension and (d) in three-dimension. In (d), the two-dimensional projection on PCo1-PCo2 is also given at the bottom. Circles, squares, and diamonds denote TSs, MINs, and VRT, and smaller circles and smaller diamonds denote the structures along the IRCs and trajectories (highlighted by light green). The colormap shows the potential energy relative to the energy of MIN1.

4.4 Conclusion

The IRC is a uniquely-determined one-dimensional reaction path to describe an elementary reaction process on the potential energy surface (PES), and the reaction path concept has played a significant role in understanding the reaction mechanism. However, since the definition of IRC depends on only the geometrical feature of PES, the IRC concept does not reflect dynamical effects. The reaction dynamics often play an essential role in the realistic reaction process, providing to the non-IRC process, and such a dynamic aspect can be recognized by examining the on-the-fly trajectory referring to the static IRC path. However, the multi-dimensionality of the molecular system makes it complex and challenging.

In this chapter, I propose a new approach to visualize a dynamic reaction route in the reduced-dimensionality subspace, which is pre-determined based on the IRCs, by employing the out-of-sample CMDS (oCMDS) method. As a demonstration, oCMDS was applied to the S_N2 reaction of $OH^- + CH_3F$ and the structural transformation of Au_5, which were investigated by CMDS in **Chapter 3**. The former application shows that both the IRC and the on-the-fly trajectories are well described in the two-dimensional principal coordinate subspace. It is also shown that the highly-curved region along the IRC works as a bifurcation point leading to two different reaction channels in a dynamical sense, which coincides with chemical intuition. For the Au_5 structural transformation, I carried out CMDS and oCMDS analyses in two different ways. First, I constructed the reduced-dimensionality bifurcation reaction space without the merged-NPI option and confirmed that several IRC-jump patterns determined the fate of the trajectory. Second, I generated the two- and three-dimensional principal coordinate subspace by CMDS for five MINs, 14 TSs, and molecular structures along 14 IRCs with the merged-NPI option. Then, I verified that the two-dimensional network is very similar to the previous map determined for only five MINs and 14 TSs in **Chapter 3**.[16] Finally, the trajectory was projected in the two- and three-dimensional principal coordinate subspaces by oCMDS, and its IRC-jump behavior was investigated based on the reduced-dimensionality reaction subspace. The present oCMDS approach that combines the IRCs and the on-the-fly MD simulations can be a robust tool to elucidate the significance of dynamic effects in the chemical reaction process.[29]

4.5 References

(1) Fukui, K. Formulation of the Reaction Coordinate. *J. Phys. Chem.* **1970**, *74*, 4161–4163.

(2) Maeda, S.; Ohno, K.; Morokuma, K. Systematic Exploration of the Mechanism of Chemical Reactions: The Global Reaction Route Mapping (GRRM) Strategy Using the ADDF and AFIR Methods. *Phys. Chem. Chem. Phys.* **2013**, *15*, 3683.

(3) Maeda, S.; Harabuchi, Y.; Takagi, M.; Saita, K.; Suzuki, K.; Ichino, T.; Sumiya, Y.; Sugiyama, K.; Ono, Y. Implementation and Performance of the Artificial Force Induced Reaction Method in the GRRM17 Program. *J. Comput. Chem.* **2018**, *39*, 233–250.

(4) Kato, S.; Morokuma, K. Potential Energy Characteristics and Energy Partitioning in Chemical Reactions: Ab Initio MO Study of Four-centered Elimination Reaction $CH_3CH_2F \rightarrow CH_2=CH_2+HF$. *J. Chem. Phys.* **1980**, *73*, 3900–3914.

(5) Taketsugu, T.; Gordon, M. S. Dynamic Reaction Path Analysis Based on an Intrinsic Reaction Coordinate. *J. Chem. Phys.* **1995**, *103*, 10042–10049.

(6) Taketsugu, T.; Gordon, M. S. Reaction Path Hamiltonian Based on a Reaction Coordinate and a Curvature Coordinate. *J. Chem. Phys.* **1996**, *104*, 2834–2840.

(7) Taketsugu, T.; Tajima, N.; Hirao, K. Approaches to Bifurcating Reaction Path. *J. Chem. Phys.* **1996**, *105*, 1933–1939.

(8) Yanai, T.; Taketsugu, T.; Hirao, K. Theoretical Study of Bifurcating Reaction Paths. *J. Chem. Phys.* **1997**, *107*, 1137–1146.

(9) Harabuchi, Y.; Ono, Y.; Maeda, S.; Taketsugu, T. Analyses of Bifurcation of Reaction Pathways on a Global Reaction Route Map: A Case Study of Gold Cluster Au_5. *J. Chem. Phys.* **2015**, *143*, 014301.

(10) Sun, L.; Song, K.; Hase, W. L. A S_N2 Reaction That Avoids Its Deep Potential Energy Minimum. *Science* **2002**, *296*, 875–878.

(11) Pratihar, S.; Ma, X.; Homayoon, Z.; Barnes, G. L.; Hase, W. L. Direct Chemical Dynamics Simulations. *J. Am. Chem. Soc.* **2017**, *139*, 3570–3590.

(12) Tsutsumi, T.; Harabuchi, Y.; Ono, Y.; Maeda, S.; Taketsugu, T. Analyses of Trajectory On-the-Fly Based on the Global Reaction Route Map. *Phys. Chem. Chem. Phys.* **2018**, *20*, 1364–1372.

(13) Olasz, B.; Czakó, G. Uncovering the Role of the Stationary Points in the Dynamics of the $F^- + CH_3I$ Reaction. *Phys. Chem. Chem. Phys.* **2019**, *21*, 1578–1586.

(14) Czakó, G.; Győri, T.; Olasz, B.; Papp, D.; Szabó, I.; Tajti, V.; Tasi, D. A.

Benchmark Ab Initio and Dynamical Characterization of the Stationary Points of Reactive Atom + Alkane and S_N2 Potential Energy Surfaces. *Phys. Chem. Chem. Phys.* **2020**.

(15) Li, X.; Xie, Y.; Hu, D.; Lan, Z. Analysis of the Geometrical Evolution in On-the-Fly Surface-Hopping Nonadiabatic Dynamics with Machine Learning Dimensionality Reduction Approaches: Classical Multidimensional Scaling and Isometric Feature Mapping. *J. Chem. Theory Comput.* **2017**, *13*, 4611–4623.

(16) Tsutsumi, T.; Ono, Y.; Arai, Z.; Taketsugu, T. Visualization of the Intrinsic Reaction Coordinate and Global Reaction Route Map by Classical Multidimensional Scaling. *J. Chem. Theory Comput.* **2018**, *14*, 4263–4270.

(17) Trosset, M. W.; Priebe, C. E. The Out-of-Sample Problem for Classical Multidimensional Scaling. *Comput. Stat. Data Anal.* **2008**, *52*, 4635–4642.

(18) Pisani, P.; Caporuscio, F.; Carlino, L.; Rastelli, G. Molecular Dynamics Simulations and Classical Multidimensional Scaling Unveil New Metastable States in the Conformational Landscape of CDK2. *PLoS One* **2016**, *11*, 1–23.

(19) Hare, S. R.; Bratholm, L. A.; Glowacki, D. R.; Carpenter, B. K. Low Dimensional Representations along Intrinsic Reaction Coordinates and Molecular Dynamics Trajectories Using Interatomic Distance Matrices. *Chem. Sci.* **2019**, *10*, 9954–9968.

(20) Cox, T.; Cox, M. *Multidimensional Scaling, Second Edition*, 2nd Edit.; C&H/CRC Monographs on Statistics & Applied Probability; Chapman and Hall/CRC: New York, 2000; Vol. 88.

(21) Härdle, W. K.; Simar, L. *Applied Multivariate Statistical Analysis*, 3rd Edit.; Springer Berlin Heidelberg: Berlin, Heidelberg, 2015.

(22) Bengio, Y.; Paiement, J.-F.; Vincent, P.; Delalleau, O.; Roux, N. Le; Ouimet, M. Out-of-Sample Extensions for LLE, Isomap, MDS, Eigenmaps, and Spectral Clustering. In *In Proceedings of the 16th International Conference on Neural Information Processing Systems (NIPS'03)*; MIT Press: Cambridge, MA, USA, 2003; pp 177–184.

(23) Kabsch, W. A Solution for the Best Rotation to Relate Two Sets of Vectors. *Acta Crystallogr. Sect. A* **1976**, *32*, 922–923.

(24) Kabsch, W. A Discussion of the Solution for the Best Rotation to Relate Two Sets of Vectors. *Acta Crystallogr. Sect. A* **1978**, *34*, 827–828.

(25) Young, G.; Householder, A. S. Discussion of a Set of Points in Terms of Their Mutual Distances. *Psychometrika* **1938**, *3*, 19–22.

(26) Harabuchi, Y.; Okai, M.; Yamamoto, R.; Tsutsumi, T.; Ono, Y.; Taketsugu, T.

SPPR. Hokkaido University: Sapporo, Japan 2020.

(27) Schmidt, M. W.; Baldridge, K. K.; Boatz, J. A.; Elbert, S. T.; Gordon, M. S.; Jensen, J. H.; Koseki, S.; Matsunaga, N.; Nguyen, K. A.; Su, S.; et al. General Atomic and Molecular Electronic Structure System. *J. Comput. Chem.* **1993**, *14*, 1347–1363.

(28) Powell, M. J. D. An Efficient Method for Finding the Minimum of a Function of Several Variables without Calculating Derivatives. *Comput. J.* **1964**.

(29) Tsutsumi, T.; Ono, Y.; Arai, Z.; Taketsugu, T. Visualization of the Dynamics Effect: Projection of on-the-Fly Trajectories to the Subspace Spanned by the Static Reaction Path Network. *J. Chem. Theory Comput.* **2020**, *16*, 4029–4037.

Chapter 5

Theoretical Study of Excited-state Branching Reaction Mechanisms of α-methyl-cis-stilbene

5.1 Introduction

The conical intersection (CI) at the crossing point of adiabatic potential energy surfaces (PESs) plays a significant role in photochemistry.[1] Recent progress in theoretical chemistry has made it feasible to elucidate the photoreaction mechanism and dynamics involving a non-radiative decay through CIs by the highly sophisticated quantum chemical approaches,[2] *ab initio* surface hopping molecular dynamics with the nonadiabatic coupling terms,[3,4] and systematic exploration of minimum energy CI (MECI) structures by the global reaction route mapping (GRRM) strategy.[5–7] A systematic search for low-lying MECIs enables the determination of the energetically favorable internal conversion paths from the Franck–Condon region. The difference in fluorescence quantum yields of aromatic molecules has recently been discussed based on the barrier heights along the internal conversion paths.[8,9]

Cis-stilbene (*cis*-SB) is a typical molecule that occurs the *cis*-*trans* photoisomerization on the $\pi\pi^*$ excitation, and its photoisomerization process has been investigated by many experimental[10–17] and theoretical[15,17–19] studies. The $\pi\pi^*$-excited *cis*-SB undergoes ultrafast decay to the ground state with a lifetime of around 1.0 ps[14,15] *via* the CI region between the singlet excited-state (S_1) and the ground-state (S_0) potential energy surfaces in the *twist* region, where the central C=C bond is twisted about 90°. Such a CI region with twisted-SB is known as the phantom state (P*).[10] Theoretical studies confirmed that the twisting motion around the central C=C bond, which is called the "*hula-twist*" motion, promotes the relaxation processes of the $\pi\pi^*$-excited *cis*-SB.[17] In addition, the $\pi\pi^*$-excited *cis*-SB has another reaction channel leading to the photocyclization to 4a,4b-dihydrophenanthrene (DHP), as well as the *cis*-*trans* isomerization. The branching ratio of products from $\pi\pi^*$-excited *cis*-SB has been experimentally measured: *cis*:*trans*:DHP = 55:35:10.[11–13,16]

Harabuchi *et al.* carried out reaction-path calculations on the S_1-PES and on-the-fly molecular dynamics (MD) simulations for the $\pi\pi^*$-excited *cis*-SB at the SF-TDDFT level and discussed the reaction mechanism and dynamics.[19] They found that the steepest descent pathway starting from the Franck–Condon point of *cis*-SB becomes sharply curved toward the DHP-form, reflecting that the two H atoms bound to the central C=C first quickly move so that each C-H-C_6H_5 fragment in SB becomes planar.[19] They also found that, in a very flat region of the S_1-PES, the on-the-fly trajectories bifurcate two ways: one direction is toward the DHP region similar to the steepest descent path, whereas another direction toward the *twist* region with a very small activation barrier.[19] Such an excited-state reaction path bifurcation can be regarded as an extension of the ground-state reaction path bifurcation.[20,21] The branching ratio from the on-the-fly MD simulations on the $\pi\pi^*$-excited *cis*-SB indicated that the dominant product is *twist*-SB (*twist*:DHP = 35:13)[19], which is consistent with the experimental data. This result suggests the importance of dynamics in photoreaction.

In 2012, Berndt *et al.* reported transit-absorption spectroscopy study on the photoreactions of 1,1'-dimethylstilbene (dmSB) in solution.[22] They also reported that the absorption band of the *cis*-dmSB in the S_1 state (CIS*) decreases with a lifetime of 0.2 ps, which is shorter than the corresponding lifetime of *cis*-SB (0.92 ps), while the absorption band of the P* state shows a surprisingly long lifetime of 19 ps in hexane, which is much longer than the corresponding lifetime of *cis*-SB (1.2 ps).[22] Harabuchi *et al.* investigated the reaction process of *cis*-dmSB in the S_1 state by the excited-state PES analysis and on-the-fly MD simulations.[23] They concluded that the long lifetime of P* state in dmSB is ascribed to the large geometrical difference between the minimum structure and MECI structure in the *twist* region and also found that the dominant product of the $\pi\pi^*$-excited *cis*-dmSB is not *trans*-dmSB but dmDHP.[23] Recently, Kokado *et al.* investigated the structural transformation of $\pi\pi^*$-excited tetraphenylethene, in which the two H atoms in stilbene are substituted by two phenyl rings, and proposed that the rotation about the central C=C bond is essential for the target process.[24] In the photoreaction process for stilbene derivatives, the substitution effect plays a significant factor in determining the photochemical properties, such as the decay lifetime and the quantum yield. Thus, the theoretical investigations on the excited-state reaction process for new substituted species can provide fruitful insights into new photoreaction concepts.

Figure 5.1 shows *cis*-, *trans*-, and DHP-forms of stilbene and its derivatives. In this chapter, I focus on α-methyl-*cis*-stilbene (*cis*-mSB). From the viewpoint of substituent effects, *cis*-mSB is expected to have intermediate properties between those of *cis*-SB and *cis*-dmSB. I also emphasize that, among three stilbene derivatives in Figure 5.1, only *cis*-mSB has asymmetric groups for ^{1}R and ^{2}R. In the same way as previous studies on *cis*-SB[19] and *cis*-dmSB[23], I examine the S_1-PES and the on-the-fly MD simulations for the ππ* excited *cis*-mSB at the SF-TDDFT level of theory and investigate the reaction routes in the S_1-state, the branching ratio provided from MD simulations, and the decay lifetime to the ground state. In contrast to SB and dmSB, there are only a few studies related to mSB.[25,26] Thus, this theoretical investigation can be utilized as predictions for this new target molecule.[27]

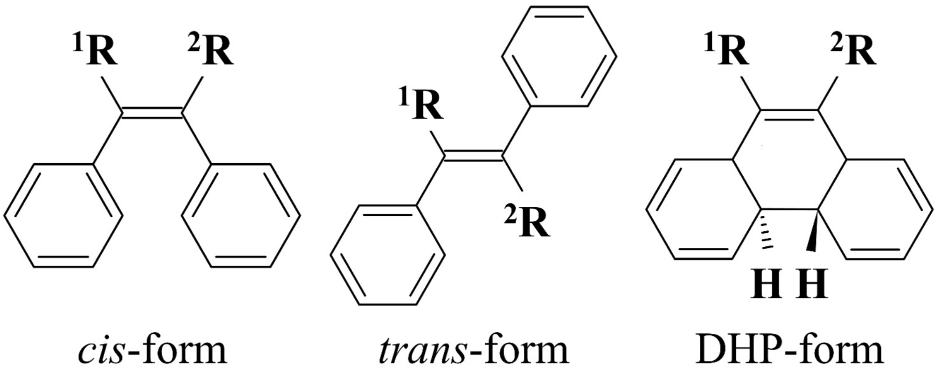

Figure 5.1. Three isomers of stilbene derivatives: stilbene for ^{1}R = ^{2}R = H, α-methyl-stilbene for ^{1}R = methyl group and ^{2}R = H, and 1,1'-dimethylstilbene for ^{1}R = ^{2}R = methyl group.

5.2 Computational Details

Geometry optimizations for mSB were performed at the SF-TDDFT level of theory to locate the minima in the S_0 and S_1 states (corresponding to *cis*-, *trans*-, *twist*-, and DHP-forms), the transition state (TS) structure connecting the DHP and *twist* regions in the S_1 state, and the S_1/S_0-MECIs in DHP and *twist* regions. The obtained minima and transition state structures were confirmed to be stationary points by normal mode analysis. The intrinsic reaction coordinate (IRC)[21,28] was calculated from the S_1-TS to confirm the connectivity of two minima in the DHP and *twist* regions. The steepest descent path in the S_1 state was calculated from the Franck–Condon (FC) structure in mass-weighted coordinates (referred to as the *meta-IRC* path). The SF-TDDFT calculations were performed with the BHHLYP functional and 6-31G(d) basis set using the GAMESS program,[29] whereas all minima, TSs, MECIs, IRCs, and meta-IRC paths were calculated by the GRRM14 program[30] with GAMESS. The branching plane update method was used in geometry optimization for the S_1/S_0-MECIs.[31]

On-the-fly MD simulations were performed for the ππ*-excited *cis*-mSB at the SF-TDDFT level using the SPPR program[32] with GAMESS. As mentioned in **Chapter 1**, the SF-TDDFT calculation provides unfavorable spin-contaminated states near the conical intersection region. In order to avoid such mixed states, I employed the T_{SF}-index method during simulations.[6] The initial conditions for the on-the-fly MD simulations were determined by normal mode sampling for the equilibrium of *cis*-mSB in the S_0 state. The initial atomic coordinates and conjugate momenta were prepared randomly by adding initial energies generated from the Boltzmann distribution at 300 K to each normal mode. The time step was set to 0.2 fs, and 40 trajectories were run until the energy difference between the S_0 and S_1 states became less than 0.2 eV or the simulation time reached 1 ps.

5.3 Results and Discussion

5.3.1 Geometries of Minima, TSs, and S_1/S_0-MECIs

By the geometry optimization, I obtained four minima in the S_0 state: $(S_0)_{cis\text{-min}}$, $(S_0)_{\mathrm{DHP\text{-}min}}$, $(S_0)_{trans1\text{-min}}$, and $(S_0)_{trans2\text{-min}}$, three minima in the S_1 state: $(S_1)_{\mathrm{DHP\text{-}min}}$, $(S_1)_{twist1\text{-min}}$, and $(S_1)_{twist2\text{-min}}$, and one TS between $(S_1)_{\mathrm{DHP\text{-}min}}$ and $(S_1)_{twist1\text{-min}}$: $(S_1)_{\mathrm{TS}}$. **Figure 5.2** shows the optimized geometries of stationary points and the relative energies in the S_0 and S_1 states, $E(S_0)$ and $E(S_1)$. The two *trans*-forms in the S_0 state have almost the same energies and are slightly lower than that of the *cis*-form (within 1 kcal/mol). Also, four significant parameters, r_{C5C6}, d_{C3C1C2C4}, d_{H7C1C2C3}, and d_{C8C2C1C4}, are summarized in **Table 5.1**, Hereafter, r_{AB} denotes the interatomic distance of *A-B* atoms, and d_{ABCD} denotes the absolute values of dihedral angle for *A-B-C-D* atoms. These four parameters indicate the structural transformations: r_{C5C6} indicates the cyclization from *cis*- to DHP-form, d_{C3C1C2C4} indicates the *cis-trans* (or *cis-twist*) isomerization, and both d_{H7C1C2C3} and d_{C8C2C1C4} indicate the pyramidalization of C1and C2 accompanying the distortion of H atom and methyl group in the central C=C bond, respectively.

In the S_0 state, there are two types of *trans*-minima where the two phenyl rings are slightly distorted from the central ethylenic plane due to steric repulsion between the methyl-phenyl groups. *Trans*-dmSB in the S_0 state also has two types of *trans*-minima for the same reason.[23] The DHP structure in the S_0 and S_1 state, $(S_0)_{\mathrm{DHP\text{-}min}}$ and $(S_1)_{\mathrm{DHP\text{-}min}}$, are almost the same geometric parameters, but the latter is slightly open the phenyl groups; $(S_0)_{\mathrm{DHP\text{-}min}}$ has $d_{\mathrm{C3C1C2C4}} = 10.1°$, but $(S_1)_{\mathrm{DHP\text{-}min}}$ has $d_{\mathrm{C3C1C2C4}} = 20.6°$. In the *twist* region in the S_1 state, two minima, $(S_1)_{twist1\text{-min}}$ and $(S_1)_{twist2\text{-min}}$, were found; the former has a pyramidal structure at H-C-phenyl (*H-pyramidal*) with $d_{\mathrm{H7C1C2C3}} = 141.8°$, and the latter has a pyramidal structure at CH_3-C-phenyl (*Me-pyramidal*) with $d_{C8C2C1C4}$ = 138.5°. Note that $(S_1)_{twist2\text{-min}}$ has higher $E(S_1)$ than $(S_1)_{twist1\text{-min}}$ (92.5 *vs.* 85.5 kcal/mol) because of the repulsion of the pramidalized methyl group and the phenyl group. As shown in Figure 5.2c, I also found a TS structure in the S_1 state and verified that $(S_1)_{TS}$ connects $(S_1)_{DHP\text{-min}}$ and $(S_1)_{twist1\text{-min}}$ (H-pyramidal structure) by IRC calculations. Thus, it is suggested that, in the *twist* region, the molecule will prefer the H-pyramidal structure rather than the Me-pyramidal structure.

(a) S_0-minima

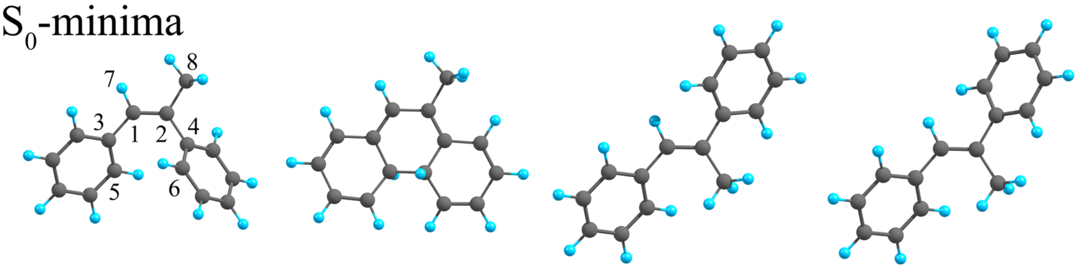

	$(S_0)_{cis\text{-min}}$	$(S_0)_{\text{DHP-min}}$	$(S_0)_{trans1\text{-min}}$	$(S_0)_{trans1\text{-min}}$
$E(S_0)$	0.0	40.0	−0.9	−0.7
$E(S_1)$	119.2	108.5	115.1	116.5

(b) S_1-minima

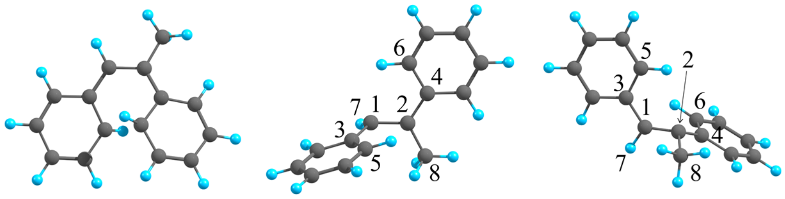

	$(S_1)_{\text{DHP-min}}$	$(S_1)_{twist1\text{-min}}$	$(S_1)_{twist2\text{-min}}$
$E(S_0)$	76.7	58.9	62.5
$E(S_1)$	83.6	85.5	92.5

(c) S_1-TS

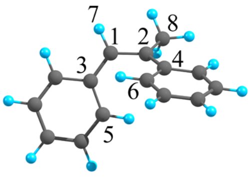

	$(S_1)_{\text{TS}}$
$E(S_0)$	38.2
$E(S_1)$	89.9

Figure 5.2. The optimized geometries of (a) the four minima in the S_0 state, (b) three minima in the S_1 state, and (c) one TS in the S_1 state for mSB. The energies of the S_0 and S_1 states relative to $(S_0)_{cis\text{-min}}$ (in kcal/mol) are shown.

Table 5.1. The relative energies (in kcal/mol) and four significant parameters of the stationary points and the MECI structures for mSB, including one interatomic distance (in Å), r_{C5C6}, and three dihedral angles (in degrees), d_{C3C1C2C4}, d_{H7C1C2C3}, and d_{C8C2C1C4}. The atom numbering is shown in Figure 5.2 and Figure 5.3.

	$E(\mathrm{S}_0)$	$E(\mathrm{S}_1)$	r_{C5C6}	d_{C3C1C2C4}	d_{H7C1C2C3}	d_{C8C2C1C4}
$(\mathrm{S}_0)_{\mathit{cis}\text{-min}}$	0.0	119.2	3.27	6.7	180.0	177.0
$(\mathrm{S}_0)_{\mathrm{DHP\text{-}min}}$	40.0	108.5	1.53	10.1	178.0	179.0
$^{*1}(\mathrm{S}_0)_{\mathit{trans}1\text{-min}}$	−0.9	115.1	5.44	179.7	178.8	179.1
$^{*1}(\mathrm{S}_0)_{\mathit{trans}2\text{-min}}$	−0.7	116.5	5.18	176.7	176.8	179.2
$(\mathrm{S}_1)_{\mathrm{DHP\text{-}min}}$	76.7	83.6	1.92	20.6	177.0	178.9
$(\mathrm{S}_1)_{\mathit{twist}1\text{-min}}$	58.9	85.5	4.05	109.1	141.8	179.8
$(\mathrm{S}_1)_{\mathit{twist}2\text{-min}}$	62.5	92.5	3.96	108.7	178.5	138.5
$(\mathrm{S}_1)_{\mathrm{TS}}$	38.2	89.9	3.17	66.0	170.0	179.9
$(\mathrm{S}_1/\mathrm{S}_0)_{\mathrm{DHP1}}$	85.8	85.8	1.94	30.6	164.7	178.8
$(\mathrm{S}_1/\mathrm{S}_0)_{\mathrm{DHP2}}$	92.1	92.1	1.93	33.5	177.8	160.8
$(\mathrm{S}_1/\mathrm{S}_0)_{\mathit{twist}1}$	91.8	91.8	4.05	124.3	103.9	177.0
$^{*2}(\mathrm{S}_1/\mathrm{S}_0)_{\mathit{twist}2}$	96.3	96.3	3.74	115.1	179.6	114.8
$(\mathrm{S}_1/\mathrm{S}_0)_{\mathit{twist}3}$	97.0	97.0	3.49	49.3	105.7	176.4
$^{*2}(\mathrm{S}_1/\mathrm{S}_0)_{\mathit{twist}4}$	97.2	97.2	4.47	133.2	173.6	115.4
$^{*3}(\mathrm{S}_1/\mathrm{S}_0)_{\mathit{twist}5}$	104.7	104.7	3.88	55.1	176.7	131.0
$^{*3}(\mathrm{S}_1/\mathrm{S}_0)_{\mathit{twist}6}$	107.9	107.9	3.84	83.8	170.2	123.5

^{*1} The difference between those two structures is d_{C1C2C4C6}; 31.8° for $(\mathrm{S}_0)_{\mathit{trans}1\text{-min}}$ and −39.8° for $(\mathrm{S}_0)_{\mathit{trans}2\text{-min}}$. ^{*2} The difference between those two structures is bond angles around the Me-pyramidalized carbon; (a_{C1C2C4}, a_{C1C2C8}) = (91.5°, 111.3°) for $(\mathrm{S}_1/\mathrm{S}_0)_{\mathit{twist}2}$, while (121.5°, 88.8°) for $(\mathrm{S}_1/\mathrm{S}_0)_{\mathit{twist}4}$. ^{*3} The difference between those two structures is bond angles around the Me-pyramidalized carbon; (a_{C1C2C4}, a_{C1C2C8}) = (139.4°, 84.6°) for $(\mathrm{S}_1/\mathrm{S}_0)_{\mathit{twist}5}$, while (87.8°, 121.8°) for $(\mathrm{S}_1/\mathrm{S}_0)_{\mathit{twist}6}$.

In the S_1/S_0-CI regions, I found two structures in the DHP region, $(S_1/S_0)_{\mathrm{DHP1}}$ and $(S_1/S_0)_{\mathrm{DHP2}}$, and six structures in the *twist* region, $(S_1/S_0)_{twist1}$, $(S_1/S_0)_{twist2}$, $(S_1/S_0)_{twist3}$, $(S_1/S_0)_{twist4}$, $(S_1/S_0)_{twist5}$, and $(S_1/S_0)_{twist6}$, as shown in **Figure 5.3**. The index for each structure is added in the descending order of potential energy. Several geometric parameters of eight MECI structures are summarized in Table 5.1. In the DHP region, $(S_1/S_0)_{\mathrm{DHP1}}$ is assigned as the H-pyramidal structure (d_{H7C1C2C3} = 164.7° and d_{C8C2C1C4} = 178.8°), while $(S_1/S_0)_{\mathrm{DHP2}}$ is assigned as the Me-pyramidal structure (d_{H7C1C2C3} = 177.8° and d_{C8C2C1C4} = 160.8°). $(S_1/S_0)_{\mathrm{DHP1}}$ is more stable than $(S_1/S_0)_{\mathrm{DHP2}}$ (85.9 *vs.* 92.1 kcal/mol) because of the steric repulsion. Also, $(S_1/S_0)_{\mathrm{DHP1}}$ is energetically close to $(S_1)_{\mathrm{DHP\text{-}min}}$ (within 2.3 kcal/mol), which indicates that the molecule could easily relax to the ground state through $(S_1/S_0)_{\mathrm{DHP1}}$ rather than $(S_1/S_0)_{\mathrm{DHP2}}$.

In the *twist* region, $(S_1/S_0)_{twist1}$ and $(S_1/S_0)_{twist3}$ are assigned to the H-pyramidal structure, whereas $(S_1/S_0)_{twist2}$, $(S_1/S_0)_{twist4}$, $(S_1/S_0)_{twist5}$, and $(S_1/S_0)_{twist6}$ are assigned to the Me-pyramidal structure. These pyramidalized structures are further classified into the *trans*-type and *cis*-type according to the relative positions of two phenyl rings; $(S_1/S_0)_{twist1}$, $(S_1/S_0)_{twist2}$, and $(S_1/S_0)_{twist4}$ correspond to the twisted-*trans*-pyramidal structure, and $(S_1/S_0)_{twist3}$, $(S_1/S_0)_{twist5}$, and $(S_1/S_0)_{twist6}$ correspond to the twisted-*cis*-pyramidal structure. The latter, twisted-*cis*-pyramidal-type MECI, has not been reported previously.[19,23] By considering those two classifications, the six S_1/S_0-MECI structures in the *twist* region can be classified into four types: H-twisted-*trans*-pyramidal ($(S_1/S_0)_{twist1}$), H-twisted-*cis*-pyramidal ($(S_1/S_0)_{twist3}$), Me-twisted-*trans*-pyramidal ($(S_1/S_0)_{twist2}$ and $(S_1/S_0)_{twist4}$), and Me-twisted-*cis*-pyramidal ($(S_1/S_0)_{twist5}$ and $(S_1/S_0)_{twist6}$).

Through the MD simulations, the molecule may preferentially approach the low-lying CI region. In order to confirm the feature of PES around CI regions, I performed meta-IRC calculations starting from the eight MECIs in the *twist* region. All the meta-IRC paths terminate at $(S_1)_{twist1\text{-min}}$ or $(S_1)_{twist2\text{-min}}$ without a barrier. Thus, the energy level of each MECI is a good factor to judge whether the on-the-fly trajectory wandering around the S_1-minima is accessible to corresponding MECIs.

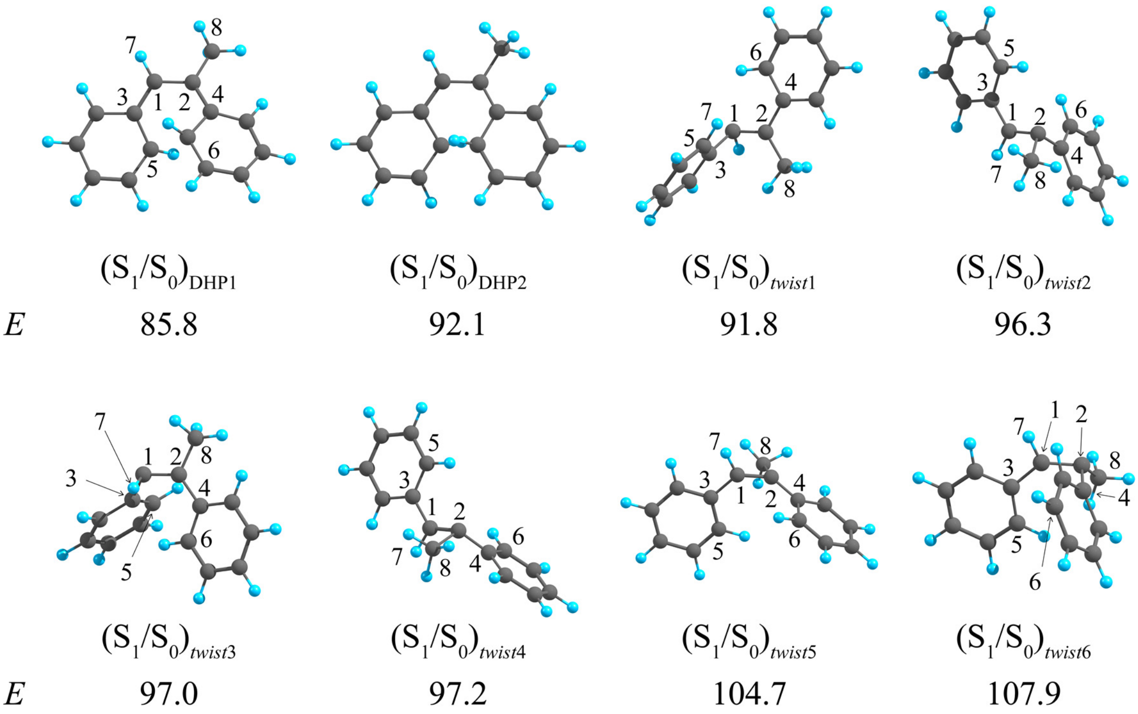
$(S_1/S_0)_{DHP1}$
$(S_1/S_0)_{DHP2}$
$(S_1/S_0)_{twist1}$
$(S_1/S_0)_{twist2}$
E 85.8 92.1 91.8 96.3
$(S_1/S_0)_{twist3}$
$(S_1/S_0)_{twist4}$
$(S_1/S_0)_{twist5}$
$(S_1/S_0)_{twist6}$
E 97.0 97.2 104.7 107.9

Figure 5.3. The optimized geometries of eight S_1/S_0-MECIs for mSB. The energy relative to $(S_0)_{cis\text{-min}}$ (*E* in kcal/mol) is also shown.

5.3.2 Reaction Pathways in the S_1 State

After the ππ*-excitation, *cis*-mSB runs down the slope of S_1-PES and branches into the DHP and *twist* regions. Following the previous studies on *cis*-SB[19] and *cis*-dmSB[23], I examine the feature of S_1-PES in the two-dimensional coordinate space spanned by r_{C5C6} and $d_{C3C1C2C4}$. As mentioned above, r_{C5C6} correlates with the photocyclization to the DHP form, and $d_{C3C1C2C4}$ correlates with the photoisomerization to the *twist* form. **Figure 5.4** shows the two-dimensional configuration space with the stationary points in the S_0 and S_1 states, the S_1/S_0-MECI structures, the meta-IRC from the Franck–Condon *cis*-structure, and the IRC in the S_1 state for (a) mSB, (b) SB[19], and (c) dmSB[23]. All molecular labels are defined in the same way as in the previous section. Note that (c) dmSB has the very flat *cis* region in the S_1 state, and there are two TSs linking the DHP-cis regions and the cis-twist regions. The meta-IRC path from the FC structure joins up with the IRC path between $(S_1)_{\text{DHP-min}}$ and $(S_1)_{twist1\text{-min}}$, indicating a branched reaction path.

The meta-IRC routes projected onto the two-dimensional subspace indicate that the molecule along the meta-IRC proceeds to the DHP region over the *twist* region in all cases. In the case of SB (Figure 5.4b), the direction of meta-IRC is toward the *twist* region in the early stage, but it rapidly turns to the DHP region before joining up with the IRC connected the DHP and *twist* minima. Thus, SB will feel the inertial force and be pushed to the *twist* region.[19] On the other hand, in the case of dmSB (Figure 5.4c), the direction of meta-IRC remains toward the DHP region, suggesting that the dominant product is the DHP-form.[23] As shown in Figure 5.4a, the meta-IRC path of mSB has the intermediate features between SB and dmSB, and thus, the branching ratio over the DHP and *twist* regions will be sensitive to the dynamic effects in the same way as the SB case.

As mentioned above, the ππ*-excited dmSB has a long lifetime of the P* state, and this behavior was ascribed to the difference in the S_1-minimum (non-pyramidal) and the S_1/S_0-MECI structure (pyramidal), where the energy difference is relatively large.[23] In the *twist* region of mSB, all S_1-minima and S_1/S_0-MECI structures have a pyramidal structure, and the energy difference between the lowest S_1-minimum and S_1/S_0-MECI is 6.3 kcal/mol that is smaller than the dmSB case (9 kcal/mol) and larger than the SB case (3 kcal/mol). Therefore, the ππ*-excited *cis*-mSB will reach the S_1/S_0-CI structures in the *twist* region much faster than the dmSB case, although its excited-state lifetime should be longer than the SB case.

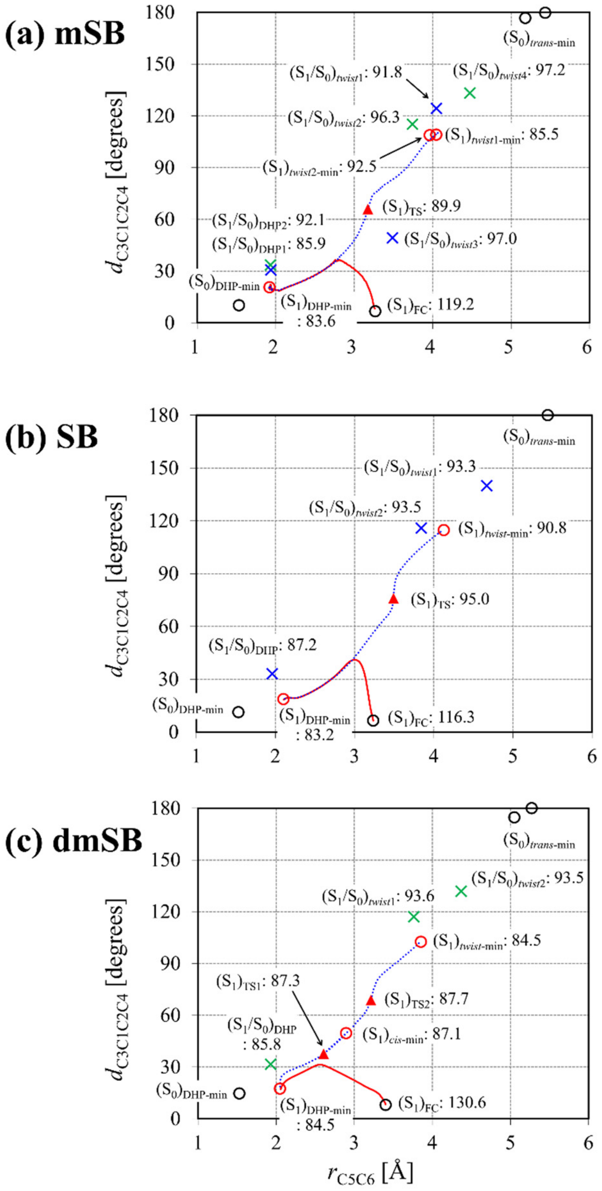

Figure 5.4. Minima, TSs, S_1/S_0-MECI structures, and reaction pathways in the S_1 state for (a) mSB, (b) SB,[19] and (c) dmSB[23] projected onto two-dimensional coordinate space. Black circles, red circles, and red triangles denote S_0-minima, S_1-minima, and S_1-TS, respectively. Also, Blue cross marks and green cross marks denote H-pyramidal and Me-pyramidal S_1/S_0-MECIs. Solid red lines and dotted blue lines denote the IRC paths and the meta-IRC path starting from the FC point. The S_1 energies (in kcal/mol) relative to $(S_0)_{cis\text{-min}}$ are given for the respective structures.

Figure 5.5 shows the variations in the dihedral angles $d_{C3C1C2C4}$, $d_{R7C1C2C4}$, and $d_{R8C2C1C3}$ (R = H or C) and r_{C5C6} along the meta-IRC from the FC point of *cis*-form for (a) mSB, (b) SB, and (c) dmSB, where $d_{C3C1C2C4}$ (in red) corresponds to the twisted angle of two phenyl groups, and $d_{R7C1C2C4}$ (in blue) and $d_{R8C2C1C3}$ (in green) correspond to the R7's and R8's deviations from the central ethylenic plane. Note that, in SB and dmSB, $d_{R7C1C2C4}$ and $d_{R8C2C1C3}$ have the same values along the meta-IRC path because of the C_2 symmetry. In all cases, $d_{C3C1C2C4}$ changes synchronously with the pair of $d_{R7C1C2C4}$ and $d_{R8C2C1C3}$; the former increases from 10° to 40° while the latter decreases from 175° to 150°. The slopes of the variations of these dihedral angles indicate the accelerations for the corresponding dihedral angles after ππ* excitation. In the *cis*-SB case (Figure 5.5b), $d_{C3C1C2C4}$ rapidly changes in the initial stage, whereas, in the *cis*-dmSB case (Figure 5.5c), $d_{C3C1C2C4}$ gradually changes. Thus, it is suggested that *cis*-SB is promptly accelerated toward the *twisted*-form, whereas the corresponding acceleration of *cis*-dmSB is much smaller. In the previous study, Harabuchi *et al.* concluded that such a difference in the reaction path profile between *cis*-SB and *cis*-dmSB was ascribed to the difference in the mass of the H and CH_3 groups in the central ethylenic part.[23] In the ππ*-excited *cis*-mSB case, the variation of $d_{C3C1C2C4}$ shows the intermediate behavior of *cis*-SB and *cis*-dmSB, which is consistent with the discussion on the reaction route profiles in Figure 5.4. However, due to the asymmetric substituent groups, the variation of $d_{H7C1C2C4}$ is not consistent with that of $d_{C8C2C1C3}$, and $d_{H7C1C2C4}$ decreases more rapidly than as shown in Figure 5.5a. Such asymmetric substituent groups (H and CH_3 groups) introduced in *cis*-mSB will provide the mixed dynamics effects that combine the features of both *cis*-SB and *cis*-dmSB.

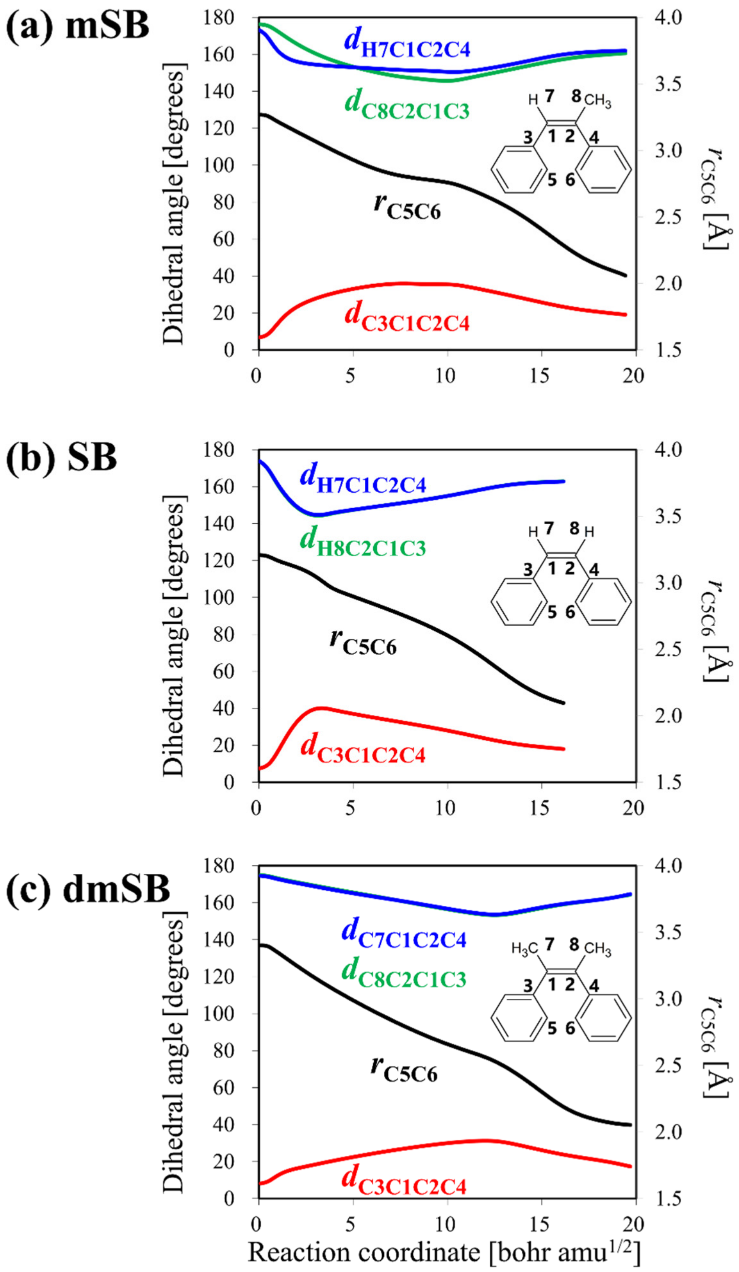

Figure 5.5. Variations in the dihedral angles $d_{C3C1C2C4}$, $d_{R7C1C2C4}$, and $d_{R8C2C1C3}$ (R = H or C) and r_{C5C6} along the meta-IRC from the Franck–Condon point of *cis*-form for (a) mSB, (b) SB, and (c) dmSB; $d_{C3C1C2C4}$ (in red) corresponds to the opening of two phenyl rings from *cis*- to *twist*-structure, $d_{R7C1C2C4}$ (in blue) corresponds to the motion of R7, and $d_{R8C2C1C3}$ (in green) corresponds to the motion of R8.

5.3.3 Excited State On-the-fly MD Simulations

The dynamics of the $\pi\pi^*$-excited *cis*-mSB, showing the branched nature toward the DHP and *twist* regions on the S_1-PES, was examined by on-the-fly MD simulations at the SF-TDDFT level. In total, 40 trajectories were run from the Franck–Condon (FC) region of the *cis*-form, in which 11 trajectories reach the DHP region while 29 trajectories reach the *twist* region, resulting in a DHP:*twist* branching ratio of 0.275:0.725. Among 40 trajectories, one exceptional trajectory enters the *twist* region first, and then it moves to the DHP region later without reaching S_1/S_0-CIs in the *twist* region. In previous studies, the branching ratio of DHP:*twist* was calculated as 0.26:0.74 for *cis*-SB[19] and 0.85:0.15 for *cis*-dmSB[23]. Thus, the ratio of *cis*-mSB is very close to that of *cis*-SB. Such branching processes are suggested from the meta-IRC profile and $(S_1)_{TS}$'s position on the two-dimensional coordinate space (Figure 5.4).

During the total simulation time of 1.0 ps, nine trajectories among the 11 trajectories entering the DHP region reached the CI region in 364 fs on average, while 16 trajectories among the 29 trajectories entering the *twist* region reached the CI region in 635 fs on average. Thus, the trajectories entering the DHP region from the FC region can more easily reach the S_1/S_0-CI and can hop to the ground state than those trajectories entering the *twist* region. **Figure 5.6** shows projections of four trajectories onto the two-dimensional coordinate space, as examples: the trajectories entering the DHP region and reaching the CI region with (a) the shortest time (117 fs) and (b) the longest time (876 fs), and the trajectories entering the *twist* region and reaching the CI region with (c) the shortest time (390 fs) and (d) the longest time (979 fs). As shown in Figure 5.6c and d, the trajectories that finally entered the *twist* region wander in the region between $(S_1)_{DHP\text{-}min}$ and $(S_1)_{TS}$, leading to a relatively longer lifetime than the trajectories in the DHP region.

I also analyzed the terminal CI points of nine trajectories in the DHP region. Four terminal structures can be categorized as H-pyramidal CI (close to $(S_1/S_0)_{DHP1}$), and one terminal structure can be categorized as Me-pyramidal CI (close to $(S_1/S_0)_{DHP2}$). However, it is difficult to classify the other four structures into H-pyramidal or Me-pyramidal structures: $(d_{H7C1C2C3}, d_{C8C2C1C4})$ = (177.7°, 173.2°), (174.3°, 175.0°), (170.0°, 173.2°), and (164.5°, 164.0°). In the case of the 16 trajectories that terminated in the *twist* region, the terminal CIs are all characterized as H-twisted-*trans*-pyramidal structures corresponding to $(S_1/S_0)_{twist1}$.

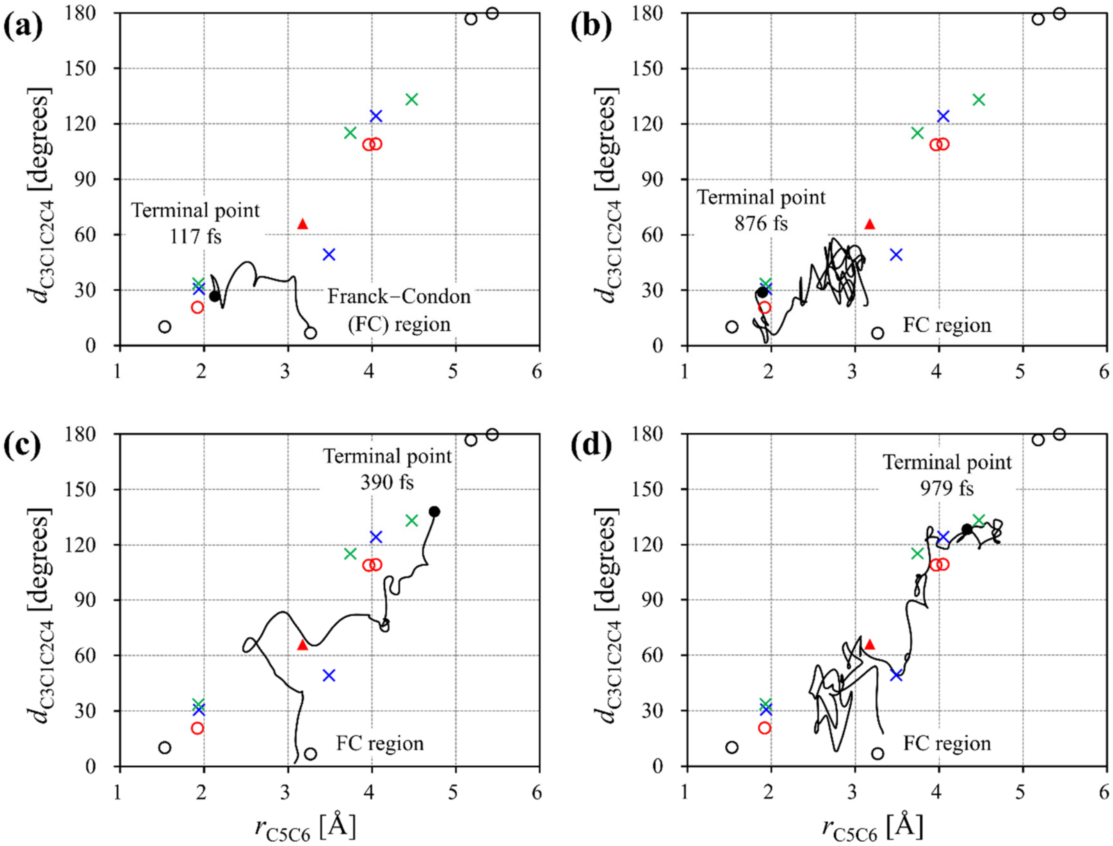

Figure 5.6. Four trajectories that start from the FC region of the *cis*-form and run on the S_1-PES: (a) one terminated at the CI in the DHP region with the shortest time; (b) one terminated at the CI in the DHP region with the longest time; (c) one terminated at the CI in the *twist* region with the shortest time; and (d) one terminated at the CI in the *twist* region with the longest time.

Figure 5.7 shows the decay of the S_1-population as a function of time calculated from on-the-fly MD simulations for (a) *cis*-mSB, (b) *cis*-SB,[19] and (c) *cis*-dmSB,[23] where all S_1 trajectories, those terminated in the DHP region, and those terminated in the *twist* region are plotted in black, red, and blue, respectively. Here, the "S_1-population" is defined as a ratio of the trajectories before reaching the CI regions between the S_0 and S_1 states. The trajectories for *cis*-SB reached the CI region on the *twist* side more quickly (Figure 5.7b), whereas the trajectories or *cis*-dmSB reached the CI region on the DHP side more quickly (Figure 5.7c). These results are explained by the directions of the meta-IRC path in the early stages and the geometrical and energy differences of the S_1-minimum and S_1/S_0-CI structures in the *twist* region.[23] In the *cis*-mSB case, the trajectories on the DHP side reach the CI region more quickly than those on the *twist* side, like for dmSB, but the trajectories in the *twist* region can proceed to the CI easily, unlike for dmSB. In other words, *cis*-mSB has no long-lifetime component in the S_1 state, unlike the *cis*-SB and *cis*-dmSB cases. This feature of *cis*-mSB is ascribed to the initial direction of the meta-IRC, which is oriented between the *twist* (*cis*-SB) and DHP (*cis*-dmSB) regions. In the *twist* region, the decay rate for mSB is slightly longer than that for SB because the energy difference of S_1-minima and S_1/S_0-MECIs is larger for mSB than for SB. The present on-the-fly MD simulations demonstrate that the introduction of light (H) and relatively heavy (CH_3) fragments to the central part of the molecule tunes the lifetime and results in the disappearance of the slow component in the excited-state dynamics.

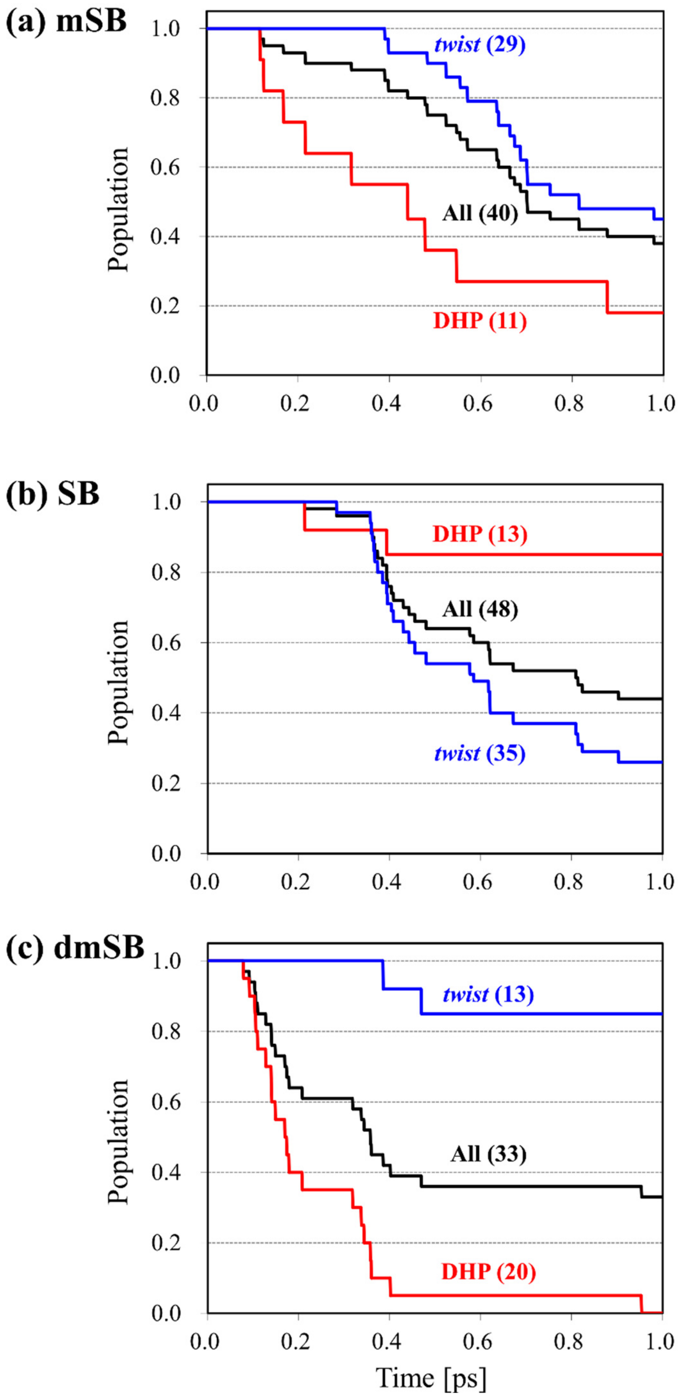

Figure 5.7. The decay of the S_1 population as a function of time derived from on-the-fly MD simulations for (a) *cis*-mSB, (b) *cis*-SB,[19] and (c) *cis*-dmSB.[23] The S_1 population for all the trajectories is plotted in black, while the decays for the trajectories remaining in the DHP region and for those in the *twist* region are plotted in red and in blue, respectively.

5.4 Conclusion

In this chapter,[27] the reaction pathways and branching dynamics on the excited-state potential energy surface for ππ*-excited *cis*-mSB were investigated by the static reaction path analysis and the on-the-fly MD simulation by using spin-flip time-dependent density functional theory (SF-TDDFT) and compared with the previous theoretical studies on *cis*-SB[19] and *cis*-dmSB[23]. In all systems, the meta-IRC path starting from the Franck–Condon structure of the *cis*-form is connected to the minimum in the DHP region, but the reaction path profile suggests that dynamics effects push the molecule partly to the *twist* region. In the case of *cis*-SB, all trajectories enter the *twist* region once because of the inertial force; subsequently, some trajectories enter the DHP region. In the case of *cis*-dmSB, most trajectories enter the DHP region along the meta-IRC path, and some trajectories move to the *twist* region later. The case of *cis*-mSB is intermediate between those of *cis*-SB and *cis*-dmSB, and, as the result of dynamics simulations, the branching ratio was calculated to be DHP:*twist* = 0.275:0.725, which is similar to the case of *cis*-SB. In the *twist* region, mSB will hop to the ground state through the H-twisted-*trans*-pyramidal S_1/S_0-CI. Concerning S_1 population decay, *cis*-SB has a slow component assigned to trajectories terminating in the DHP region, whereas *cis*-dmSB has a slow component assigned to trajectories terminating in the *twist* region. On the other hand, *cis*-mSB has no slow component because its reaction path profile is intermediate between those of *cis*-SB and *cis*-dmSB. Through the analysis of the excited state branching reactions, I suggest that the excited state reaction processes and the lifetime in stilbene derivatives can be controlled by the non-equivalent substitutions, such as H- and CH_3-groups, in the C=C part of stilbene.

In this chapter, I defined the two-dimensional coordinate space determined by two internal coordinates, which were chosen based on the chemical intuition on the excited state branching reaction of the stilbene derivatives. Such a dimensionality reduction approach enables us to interpret the reaction mechanisms for several derivatives in terms of the simple and common geometrical properties; however, it is not always possible to define appropriate internal coordinates that describe a multi-processes reaction. Even though the internal-coordinate-based dimensionality reduction method has these limitations, it is useful as a first approximation of the dimensionality reduction. In **Chapter 3**, I proposed a method to visualize a set of molecular structures onto the reduced-dimensionality coordinate space without any chemical intuition,[33] and, in **Chapter 4**, I also proposed a trajectory analysis method based on the reduced-dimensionality subspace.[34] In the next chapter, I will analyze the excited state branching reaction for the stilbene by combining the previously proposed methods.

5.5 References

(1) Domcke, W.; Yarkony, D. R. Role of Conical Intersections in Molecular Spectroscopy and Photoinduced Chemical Dynamics. *Annu. Rev. Phys. Chem.* **2012**, *63*, 325–352.

(2) Nakayama, A.; Harabuchi, Y.; Yamazaki, S.; Taketsugu, T. Photophysics of Cytosine Tautomers: New Insights into the Nonradiative Decay Mechanisms from MS-CASPT2 Potential Energy Calculations and Excited-State Molecular Dynamics Simulations. *Phys. Chem. Chem. Phys.* **2013**, *15*, 12322.

(3) Taketsugu, T.; Tajima, A.; Ishii, K.; Hirano, T. Ab Initio Direct Trajectory Simulation with Nonadiabatic Transitions of the Dissociative Recombination Reaction $HCNH^+ + e^- \rightarrow HNC/HCN + H$. *Astrophys. J.* **2004**, *608*, 323–329.

(4) Ootani, Y.; Satoh, K.; Nakayama, A.; Noro, T.; Taketsugu, T. Ab Initio Molecular Dynamics Simulation of Photoisomerization in Azobenzene in the $N\pi^*$ State. *J. Chem. Phys.* **2009**, *131*, 194306.

(5) Harabuchi, Y.; Maeda, S.; Taketsugu, T.; Minezawa, N.; Morokuma, K. Automated Search for Minimum Energy Conical Intersection Geometries between the Lowest Two Singlet States S_0/S_1-MECIs by the Spin-Flip TDDFT Method. *J. Chem. Theory Comput.* **2013**, *9*, 4116–4123.

(6) Maeda, S.; Harabuchi, Y.; Taketsugu, T.; Morokuma, K. Systematic Exploration of Minimum Energy Conical Intersection Structures near the Franck–Condon Region. *J. Phys. Chem. A* **2014**, *118*, 12050–12058.

(7) Maeda, S.; Taketsugu, T.; Ohno, K.; Morokuma, K. From Roaming Atoms to Hopping Surfaces: Mapping Out Global Reaction Routes in Photochemistry. *J. Am. Chem. Soc.* **2015**, *137*, 3433–3445.

(8) Harabuchi, Y.; Taketsugu, T.; Maeda, S. Exploration of Minimum Energy Conical Intersection Structures of Small Polycyclic Aromatic Hydrocarbons: Toward an Understanding of the Size Dependence of Fluorescence Quantum Yields. *Phys. Chem. Chem. Phys.* **2015**, *17*, 22561–22565.

(9) Harabuchi, Y.; Taketsugu, T.; Maeda, S. Nonadiabatic Pathways of Furan and Dibenzofuran: What Makes Dibenzofuran Fluorescent? *Chem. Lett.* **2016**, *45*, 940–942.

(10) Saltiel, J. Perdeuteriostilbene. The Role of Phantom States in the Cis-Trans Photoisomerization of Stilbenes. *J. Am. Chem. Soc.* **1967**, *89*, 1036–1037.

(11) Muszkat, K. A.; Fischer, E. Structure, Spectra, Photochemistry, and Thermal Reactions of the 4a,4b-Dihydrophenanthrenes. *J. Chem. Soc. B Phys. Org.* **1967**,

No. 0, 662.

(12) Wismonski-Knittel, T.; Fischer, G.; Fischer, E. Temperature Dependence of Photoisomerization. Part VIII. Excited-State Behaviour of 1-Naphthyl-2-Phenyl- and 1,2-Dinaphthyl-Ethylenes and Their Photocyclisation Products, and Properties of the Latter. *J. Chem. Soc. Perkin Trans. 2* **1974**, *15*, 1930.

(13) Petek, H.; Yoshihara, K.; Fujiwara, Y.; Lin, Z.; Penn, J. H.; Frederick, J. H. Is the Nonradiative Decay of S_1 Cis-Stilbene Due to the Dihydrophenanthrene Isomerization Channel? Suggestive Evidence from Photophysical Measurements on 1,2-Diphenylcycloalkenes. *J. Phys. Chem.* **1990**, *94*, 7539–7543.

(14) Todd, D. C.; Jean, J. M.; Rosenthal, S. J.; Ruggiero, A. J.; Yang, D.; Fleming, G. R. Fluorescence Upconversion Study of Cis -stilbene Isomerization. *J. Chem. Phys.* **1990**, *93*, 8658–8668.

(15) Pedersen, S.; Bañares, L.; Zewail, A. H. Femtosecond Vibrational Transition-state Dynamics in a Chemical Reaction. *J. Chem. Phys.* **1992**, *97*, 8801–8804.

(16) Rodier, J. M.; Myers, A. B. Cis-Stilbene Photochemistry: Solvent Dependence of the Initial Dynamics and Quantum Yields. *J. Am. Chem. Soc.* **1993**, *115*, 10791–10795.

(17) Fuß, W.; Kosmidis, C.; Schmid, W. E.; Trushin, S. A. The Photochemicalcis–Trans Isomerization of Free Stilbene Molecules Follows a Hula-Twist Pathway. *Angew. Chemie Int. Ed.* **2004**, *43*, 4178–4182.

(18) Taketsugu, T.; Harabuchi, Y. Ab Initio Molecular Dynamics Study on Photoisomerization Reactions: Applications to Azobenzene and Stilbene. In *Frontiers of Quantum Chemistry*; Wójcik, M. J., Nakatsuji, H., Kirtman, B., Ozaki, Y., Eds.; Springer Singapore: Singapore, 2018; pp 431–453.

(19) Harabuchi, Y.; Keipert, K.; Zahariev, F.; Taketsugu, T.; Gordon, M. S. Dynamics Simulations with Spin-Flip Time-Dependent Density Functional Theory: Photoisomerization and Photocyclization Mechanisms of Cis- Stilbene in Ππ* States. *J. Phys. Chem. A* **2014**, *118*, 11987–11998.

(20) Tsutsumi, T.; Harabuchi, Y.; Ono, Y.; Maeda, S.; Taketsugu, T. Analyses of Trajectory On-the-Fly Based on the Global Reaction Route Map. *Phys. Chem. Chem. Phys.* **2018**, *20*, 1364–1372.

(21) Maeda, S.; Harabuchi, Y.; Ono, Y.; Taketsugu, T.; Morokuma, K. Intrinsic Reaction Coordinate: Calculation, Bifurcation, and Automated Search. *Int. J. Quantum Chem.* **2015**, *115*, 258–269.

(22) Berndt, F.; Dobryakov, A. L.; Quick, M.; Mahrwald, R.; Ernsting, N. P.; Lenoir, D.; Kovalenko, S. A. Long-Lived Perpendicular Conformation in the

Photoisomerization Path of 1,1′-Dimethylstilbene and 1,1′-Diethylstilbene. *Chem. Phys. Lett.* **2012**, *544*, 39–42.

(23) Harabuchi, Y.; Yamamoto, R.; Maeda, S.; Takeuchi, S.; Tahara, T.; Taketsugu, T. Ab Initio Molecular Dynamics Study of the Photoreaction of 1,1′-Dimethylstilbene upon $S_0 \rightarrow S_1$ Excitation. *J. Phys. Chem. A* **2016**, *120*, 8804–8812.

(24) Kokado, K.; Machida, T.; Iwasa, T.; Taketsugu, T.; Sada, K. Twist of C═C Bond Plays a Crucial Role in the Quenching of AIE-Active Tetraphenylethene Derivatives in Solution. *J. Phys. Chem. C* **2018**, *122*, 245–251.

(25) Brandt, P.; Hedberg, C.; Andersson, P. G. New Mechanistic Insights into the Iridium–Phosphanooxazoline-Catalyzed Hydrogenation of Unfunctionalized Olefins: A DFT and Kinetic Study. *Chem. - A Eur. J.* **2003**, *9*, 339–347.

(26) Serreli, V.; Lee, C.-F.; Kay, E. R.; Leigh, D. A. A Molecular Information Ratchet. *Nature* **2007**, *445*, 523–527.

(27) Tsutsumi, T.; Harabuchi, Y.; Yamamoto, R.; Maeda, S.; Taketsugu, T. On-the-Fly Molecular Dynamics Study of the Excited-State Branching Reaction of α-Methyl-Cis-Stilbene. *Chem. Phys.* **2018**, *515*, 564–571.

(28) Fukui, K. Formulation of the Reaction Coordinate. *J. Phys. Chem.* **1970**, *74*, 4161–4163.

(29) Schmidt, M. W.; Baldridge, K. K.; Boatz, J. A.; Elbert, S. T.; Gordon, M. S.; Jensen, J. H.; Koseki, S.; Matsunaga, N.; Nguyen, K. A.; Su, S.; et al. General Atomic and Molecular Electronic Structure System. *J. Comput. Chem.* **1993**, *14*, 1347–1363.

(30) Maeda, S.; Harabuchi, Y.; Sumiya, Y.; Takagi, M.; Hatanaka, M.; Osada, Y.; Taketsugu, T.; Morokuma, K.; Ohno, K. GRRM14. Hokkaido University, Sapporo, Japan 2017.

(31) Maeda, S.; Ohno, K.; Morokuma, K. Updated Branching Plane for Finding Conical Intersections without Coupling Derivative Vectors. *J. Chem. Theory Comput.* **2010**, *6*, 1538–1545.

(32) Harabuchi, Y.; Okai, M.; Yamamoto, R.; Tsutsumi, T.; Ono, Y.; Taketsugu, T. SPPR. Hokkaido University: Sapporo, Japan 2020.

(33) Tsutsumi, T.; Ono, Y.; Arai, Z.; Taketsugu, T. Visualization of the Intrinsic Reaction Coordinate and Global Reaction Route Map by Classical Multidimensional Scaling. *J. Chem. Theory Comput.* **2018**, *14*, 4263–4270.

(34) Tsutsumi, T.; Ono, Y.; Arai, Z.; Taketsugu, T. Visualization of the Dynamics Effect: Projection of on-the-Fly Trajectories to the Subspace Spanned by the

Static Reaction Path Network. *J. Chem. Theory Comput.* **2020**, *16*, 4029–4037.

Chapter 6

Visualization of Multi-state Potential Energy Landscape: A Case Study on Excited-state Branching Reaction of Stilbene

6.1 Introduction

Cis-stilbene (SB)[1] has been of interest as a typical molecule in which the *cis*-*trans* photoisomerization and the photocyclization that provides 4a,4b-dihydrophenanthrene (DHP)[2] compete in the $\pi\pi^*$ excited state. The photoisomerization, which is a dominant relaxation channel for *cis*-SB, often has been discussed based on a traditional one-dimensional potential energy curve along mainly the twisting coordinate of the ethylenic part.[3] In this potential curve, a large barrier exists between *cis*- and *trans*-form in the ground electronic (S_0) state, whereas, in the first-excited singlet (S_1) state, there is a potential minimum at the 90° twisted form (often called "phantom state"), where S_0 and S_1 states seem to be degenerate. Then, the $\pi\pi^*$-excited *cis*-SB is regarded to decay through the twisted region and finally relax to either *trans*- or *cis*-form in the S_0 state. The spectroscopy studies revealed that the decay processes for the $\pi\pi^*$-excited *cis*-SB were complete within 2 ps, indicating there was almost no barrier during the twisting motion on the S_1 state.[4–6] Also, the experimental results concluded that a branching ratio for *cis*:*trans*:DHP was 55:35:10.[2,7,8] The femtosecond impulsive Raman spectroscopy[9] and the femtosecond time-resolved fluorescence spectroscopy[10] monitored excited-state dynamics for *cis*-SB, concluding that the molecule exhibited the twisting motions on the early stage of the S_1 state and proceeded to the non-twisted and the twisted regions with time constants 0.23 and 1.2 ps. For the *trans*-SB, there is a planar minimum of C_{2h} symmetry in the S_1 state, and therefore a small barrier exists along the *trans*-*cis* isomerization reaction coordinate, indicating the relatively long lifetime of $\pi\pi^*$-excited *trans*-SB (10 ~ 200 ps)[11–13] than *cis*-SB.

Many theoretical researchers have investigated the excited-state decay mechanisms for *cis*-SB. After the $\pi\pi^*$ excitation, *cis*-SB gradually twisted the C=C bond during the *cis*-*trans* photoisomerization and reached the twisted minimum (MIN) on the excited-state potential energy surface (PES).[14] The conical intersections (CIs) between the S_0 and S_1 states, where excited molecules pass through during the non-radiative decay process, were located near the twisted MIN,[14–17] and the molecule then proceeded to the CI region with the "*hula-twist*" motion.[18] Also, the photocyclization to DHP-form was investigated theoretically, and the CIs in DHP region[16,17,19] and the excited-state dynamics by semiclassical simulations[20] were reported. Harabuchi *et al.* carried out the static reaction path analysis and the on-the-fly molecular dynamics (MD) simulation for *cis*-SB and reported the excited-state branching reaction mechanism and the branching ratio for DHP and *twist* sides with the respective lifetimes.[21] To construct the two-dimensional excited-state reaction surface, they defined two internal coordinates, a twisting angle of C=C and a bond length involved the cyclization, and discussed the excited-state dynamics by projecting on-the-fly trajectories onto the reaction surface.[21] Very recently, the nonadiabatic dynamics for *cis*-SB were performed by the *ab initio* multiple spawning method, and they clarified the comprehensive non-radiative decay mechanisms including both the S_1 and S_0 states.[22]

The stilbene derivatives with the substituents on the central C=C region have also been studied for their excited-state dynamics. Berndt *et al.* measured the transient absorption spectra for 1,1'-dimethylstilbene (dmSB) in several solutions. The observed bands involved two decay components, which correspond to the *cis*-*trans* photoisomerization and the photocyclization to the DHP-form of dmSB, indicating interestingly that the tendencies of the branching ratio and the lifetimes for *cis*-dmSB was opposite to that for SB.[23] For elucidating the inherent factor making a crucial difference between *cis*-SB and *cis*-dmSB, Harabuchi *et al.* investigated the excited-state reaction dynamics for *cis*-dmSB based on the two-dimensional reaction surface, which is pre-defined in the previous study for *cis*-SB,[21] and revealed that the methyl substituents weight and steric repulsion hindered the twisting motion of *cis*-dmSB.[24] Later, as discussed in **Chapter 5**, I also investigated the photochemical reaction for α-methyl-*cis*-stilbene (mSB)[25] and discussed the excited-state branching reaction mechanisms compared to both *cis*-SB[21] and *cis*-dmSB[24]. In 2018, photoluminescence behaviors of a stilbene derivative with aggregation-induced emission were discussed experimentally and theoretically, indicating that quenching phenomena resulted from the C=C twisting motion.[26]

In the previous studies for SB,[21] mSB,[25] and dmSB,[24] the two-dimensional reaction surface was tentatively determined by two internal coordinates corresponding to the photoisomerization and the photocyclization; however, selecting those coordinates requires chemical intuition and is not unique. In data science, such ambiguity is avoided by a dimensionality reduction technique that extracts data features from high-dimensional data space. Several studies indeed verified that chemical reaction mechanisms and corresponding dynamics were discussed by dimensionality reduction techniques: the principal component analysis (PCA),[27,28] the classical multidimensional scaling (CMDS),[29–32] the isometric feature mapping (Isomap),[30,33] and the locally linear embedding (LLE).[33]

The CMDS method is a dimensionality reduction technique that reproduces a mutual distance relationship of given high-dimensional data in a lower-dimensional space. In molecule language, it transforms a pairwise distance matrix for a set of molecular structures into principal coordinates that determine the configuration of each molecule.[34–36] In 2008, Trosset *et al.* proposed a method to project "*out-of-sample*" data into the reduced-dimensionality subspace defined by the CMDS.[37] Such out-of-sample extended CMDS method is named as oCMDS in our research. Very recently, I applied these methods to visualize several chemical reaction routes for the collision reaction of OH^- $+CH_3F \rightarrow [CH_3OH\cdots F]^-$ and the ground-state isomerization reaction of a small gold cluster (in **Chapter 3**)[31] and revealed their dynamical reaction mechanisms based on the reduced-dimensionality reaction route map (in **Chapter 4**)[32]. In this chapter, I uniquely construct the ground-state, the excited-state, and the multi-state potential energy landscapes by applying the CMDS to the photochemical reaction for *cis*-SB. Also, by combining the on-the-fly MD simulation and the oCMDS method, I investigate the non-radiative decay processes of $\pi\pi^*$-excited *cis*-SB. Finally, I attempt to discuss geometrical features of the excited-state reaction route maps for *cis*-SB, *cis*-mSB, and *cis*-dmSB. The CMDS and oCMDS procedures are already summarized in **Chapter 3** and **Chapter 4**.

Similar to the previous Chapters, the proportion of variance for the *a*th principal coordinate (PCo) and the cumulated proportion are denoted by Λ_a and Λ, respectively.

6.2 Database of Molecular Structures in the S_0 and S_1 states

Through the quantum chemistry calculations, I found three minima, *cis*-, *trans*-, and DHP-forms (denoted by S_0-MIN$_{cis}$, S_0-MIN$_{trans}$, and S_0-MIN$_{\mathrm{DHP}}$) and two transition state (TS) structures (denoted by S_0-TS$_{cis\text{-}\mathrm{DHP}}$ and S_0-TS$_{cis\text{-}trans}$) in the S_0 state; three minima, DHP-, *twist*-, and *trans*-forms (denoted by S_1-MIN$_{\mathrm{DHP}}$, S_0-MIN$_{twist}$, and S_0-MIN$_{trans}$) and two TS structures (denoted by S_1-TS$_{\mathrm{DHP}\text{-}twist}$ and S_1-TS$_{twist\text{-}trans}$) in the S_1 state; and three minimum-energy conical intersections (MECIs) (denoted by S_1/S_0-CI$_{\mathrm{DHP}}$, S_1/S_0-CI$_{twist1}$, and S_1/S_0-CI$_{twist2}$) between the S_0 and S_1 states. Note that S_i-MIN$_{\mathrm{A}}$, S_i-TS$_{\mathrm{A\text{-}B}}$, and S_i/S_j-CI$_{\mathrm{A}}$ indicate a minimum (MIN) structure of A-form on the S_i state, a TS structure connecting A- and B-form on the S_i state, and a MECI structure in A-region between the S_i and S_j states, respectively. **Figure 6.1** shows these molecular structures with the relative potential energies in the S_0 and S_1 states.

The intrinsic reaction coordinates (IRCs), which is defined as the steepest descent path connecting two minima *via* one TS on the mass-weighted potential energy surface (PES), were calculated from three TS structures, and it verified that four IRCs from S_0-TS$_{cis\text{-}\mathrm{DHP}}$, S_0-TS$_{cis\text{-}trans}$, S_1-TS$_{\mathrm{DHP}\text{-}twist}$, and S_1-TS$_{twist\ \text{-}trans}$ connect *cis*- and DHP-forms in the S_0 state, *cis*- and *trans*-forms in the S_0 state, DHP- and *twist*-forms in the S_1 state, and *twist*- and *trans*-forms in the S_1 state, respectively. I also calculated the steepest descent paths starting from the Franck–Condon (FC) point of three S_0-minima on the S_1-PES. Note that such a path starting from a non-TS structure is called a "*meta-IRC*." Two meta-IRCs from the FC points of S_0-MIN$_{cis}$ and S_0-MIN$_{\mathrm{DHP}}$ both reached S_1-MIN$_{\mathrm{DHP}}$, while another meta-IRC from the FC point of S_0-MIN$_{trans}$ reached S_1-MIN$_{trans}$. Additionally, I calculated the meta-IRC paths on the S_0- and S_1-PESs from three MECIs. Because these MECIs found in this chapter are not the peaked CIs, which are consistent with minima on the S_1-PES, but the sloped CIs, the possible meta-IRCs on the S_0 and S_1 states are only one, respectively. Consequently, I obtained six meta-IRCs related to three MECIs: the meta-IRCs starting from S_1/S_0-CI_{DHP} reached *cis*- and DHP-forms on the S_0- and S_1-PESs, and ones from S_1/S_0-CI_{twist1} and S_1/S_0-CI_{twist2} both reached *trans*- and *twist*-forms on the S_0- and S_1-PESs, respectively.

To compare the excited-state reaction route map for *cis*-SB with those for the stilbene derivatives, I performed the excited-state reaction path analyses for mSB and dmSB. In mSB, I found S_1-MIN_{DHP}, S_1-MIN_{twist}, and S_1-$TS_{DHP\text{-}twist}$ and verified that the IRC starting from S_1-$TS_{DHP\text{-}twist}$ connected S_1-MIN_{DHP} and S_1-MIN_{twist} on the S_1-PES. Similarly, in dmSB, I found S_1-MIN_{DHP}, S_1-MIN_{cis}, S_1-MIN_{twist}, S_1-$TS_{DHP\text{-}cis}$, and S_1-$TS_{cis\text{-}twist}$ and verified the IRC connectivities: IRC starting from S_1-$TS_{DHP\text{-}cis}$ connected S_1-MIN_{DHP} and S_1-MIN_{cis} and IRC starting from S_1-$TS_{cis\text{-}twist}$ connected S_1-MIN_{cis} and S_1-MIN_{twist}, respectively. The meta-IRCs starting from each FC point of optimized S_0-MIN_{cis} for mSB and dmSB were calculated on the S_1-PES, indicating that each terminal point was S_1-MIN_{DHP}. The obtained minima and TS structures for mSB and dmSB were shown in Subsection 5.3.1 and Ref 24, respectively.

I also performed the on-the-fly MD simulation on both the S_1 and S_0 states to comprehensively discuss the non-radiative decay dynamics for *cis*-SB. First, the on-the-fly trajectories for $\pi\pi^*$-excited *cis*-SB were run on the S_1-PES. The initial conditions for the excited-state MD simulation were determined by the normal-mode sampling of S_0-MIN_{cis}: the atomic coordinates and the velocities were generated by adding initial energy following the Boltzmann distribution at 300 K to each normal mode. The time step was set to 0.2 fs, and 30 trajectories were run until the energy difference between the S_0 and S_1 states becomes 0.2 eV or less. All trajectories reached near CI regions within 5 ps.

Then, these trajectories continued to run on the S_0-PES until the additional simulation time reached 1 ps, where the initial atomic coordinates and the velocities were determined as those of terminal point for each trajectory simulated previously on the S_1 state. In this paper, I discuss typical two trajectories (Trj-DHP and Trj-*twist*) that decay from S_1/S_0-CI_{DHP} and S_1/S_0-CI_{twist2} to the S_0 state.

The molecular structure database obtained through the above static and dynamic analyses for SB is summarized in **Table 6.1**. To construct simple dimensionality-reduction maps, I thinned out the forward-, the backward-IRCs, and the meta-IRCs so that the number of molecular structures would be about 10. Similarly, the on-the-fly trajectories were thinned out accordingly. All electronic structure calculations were performed by the GAMESS program[38] with Spin-flip TDDFT (BHHLYP)/6-31g* level of theory. The geometry optimization and the reaction path calculation were performed by the GRRM17 program[39] with the T_{SF}-index option[40] as described in **Chapter 1**. To verify both S_0- and S_1-TS geometries obtained by the GRRM17 program, I further carried out the vibrational calculation by the GAMESS program. The on-the-fly MD simulation was performed by the SPPR program[41].

(a) Ground state (S_0)

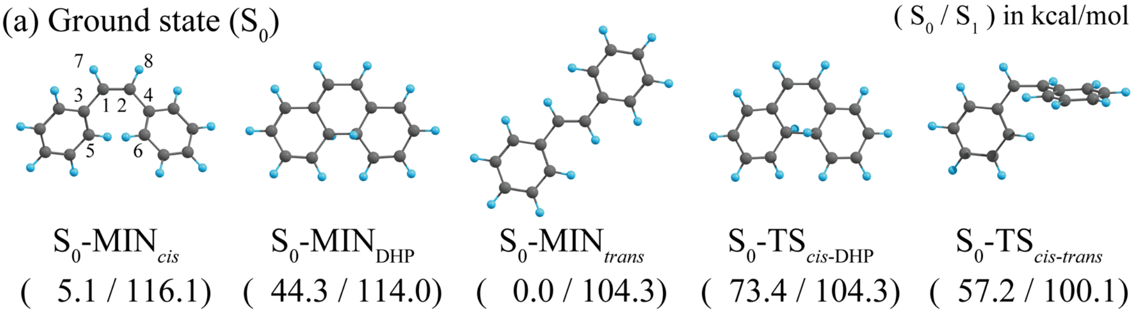
(S_0 / S_1) in kcal/mol
7
8
3
1
2
4
5
6
S_0-MIN$_{cis}$
(5.1 / 116.1)
S_0-MIN$_{\mathrm{DHP}}$
(44.3 / 114.0)
S_0-MIN$_{trans}$
(0.0 / 104.3)
S_0-TS$_{cis\text{-DHP}}$
(73.4 / 104.3)
S_0-TS$_{cis\text{-}trans}$
(57.2 / 100.1)

(b) Excited state (S_1)

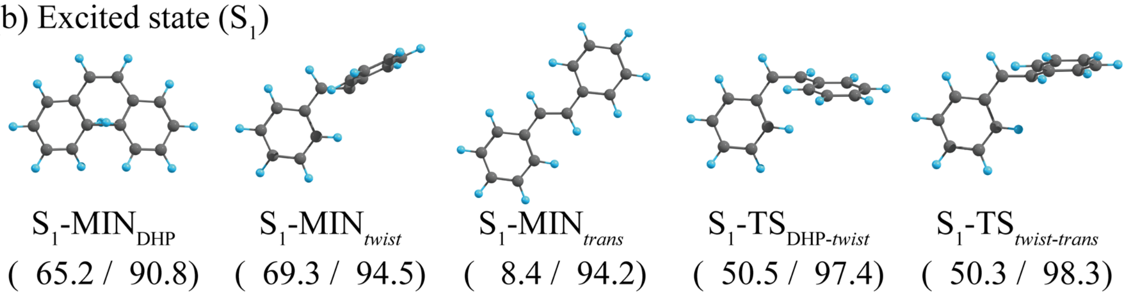
S_1-MIN$_{\mathrm{DHP}}$
(65.2 / 90.8)
S_1-MIN$_{twist}$
(69.3 / 94.5)
S_1-MIN$_{trans}$
(8.4 / 94.2)
S_1-TS$_{\mathrm{DHP}\text{-}twist}$
(50.5 / 97.4)
S_1-TS$_{twist\text{-}trans}$
(50.3 / 98.3)

(c) Conical intersections (S_1/S_0)

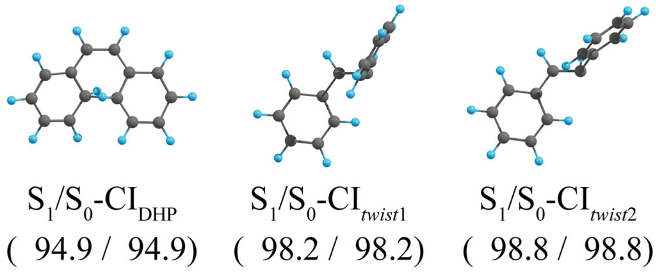
S_1/S_0-CI$_{\mathrm{DHP}}$
(94.9 / 94.9)
S_1/S_0-CI$_{twist1}$
(98.2 / 98.2)
S_1/S_0-CI$_{twist2}$
(98.8 / 98.8)

Figure 6.1. The molecular structures for stilbene (SB): (a) three minima and two transition state structures (TSs) in the S_0 state, (b) two minima and one TS in the S_1 state, and (c) three conical intersections (CIs) between the S_0 and S_1 states. The potential energies relative to S_0-MIN$_{trans}$ are shown as (S_0 / S_1) in kcal/mol.

Table 6.1. Database of the molecular structures for the stilbene (SB). Note that all IRCs, meta-IRCs, and trajectories are thinned out accordingly to obtain simple dimensionality-reduction maps.

SB	Descriptions	# of data
S_0-MIN	S_0-MIN$_{\mathrm{DHP}}$, S_0-MIN$_{cis}$, and S_0-MIN$_{trans}$	3
S_0-TS	S_0-TS$_{\mathrm{DHP}\text{-}cis}$ and S_0-TS$_{cis\text{-}trans}$	2
S_1-MIN	S_1-MIN$_{\mathrm{DHP}}$, S_1-MIN$_{twist}$, and S_1-MIN$_{trans}$	3
S_1-TS	S_1-TS$_{\mathrm{DHP}\text{-}twist}$ and S_1-TS$_{twist\text{-}trans}$	2
S_1/S_0-CI	S_1/S_0-CI$_{\mathrm{DHP}}$, S_1/S_0-CI$_{twist1}$, and S_1/S_0-CI$_{twist2}$	3
S_0-Path	IRC linking S_0-MIN$_{\mathrm{DHP}}$, S_0-TS$_{\mathrm{DHP}\text{-}cis}$, and S_0-MIN$_{cis}$	25
	IRC linking S_0-MIN$_{cis}$, S_0-TS$_{cis\text{-}trans}$, and S_0-MIN$_{trans}$	24
	Meta-IRC starting from S_1/S_0-CI$_{\mathrm{DHP}}$	12
	Meta-IRC starting from S_1/S_0-CI$_{twist1}$	12
	Meta-IRC starting from S_1/S_0-CI$_{twist2}$	12
S_1-Path	IRC linking S_1-MIN$_{\mathrm{DHP}}$, S_1-TS$_{\mathrm{DHP}\text{-}twist}$, and S_1-MIN$_{twist}$	25
	IRC linking S_1-MIN$_{twist}$, S_1-TS$_{twist\text{-}trans}$, and S_1-MIN$_{trans}$	22
	Meta-IRC starting from the Franck–Condon point of S_0-MIN$_{\mathrm{DHP}}$	13
	Meta-IRC starting from the Franck–Condon point of S_0-MIN$_{cis}$	11
	Meta-IRC starting from the Franck–Condon point of S_0-MIN$_{trans}$	12
	Meta-IRC starting from S_1/S_0-CI$_{\mathrm{DHP}}$	11
	Meta-IRC starting from S_1/S_0-CI$_{twist1}$	13
	Meta-IRC starting from S_1/S_0-CI$_{twist2}$	12
Trj-DHP	Reaching near S_1/S_0-CI$_{\mathrm{DHP}}$ on S_1-PES and running around S_0-MIN$_{\mathrm{DHP}}$ after hopping to S_0-PES.	40
Trj-*twist*1	Reaching near S_1/S_0-CI$_{twist2}$ on S_1-PES and running around S_0-TS$_{cis\text{-}trans}$ after hopping to S_0-PES.	27
Trj-*twist*2	Proceeding to *twist* region on S_1-PES and repeating the *cis-trans* isomerization after hopping to S_0-PES.	37

For a well-defined reduced-dimensionality map, I have to prepare the distance matrix scrutinized the atom mapping between pairwise molecules. The molecule with the different atom-mapping is called the nuclear permutation inversion (NPI) isomer, and the linear distance (eq. 1) between two NPI isomers becomes non-zero. In this chapter, to handle the NPI problem, I employ the smallest distance between a target molecule and arbitrary NPI isomers as a pairwise linear distance,[42] which is named the merged-NPI procedure. Although this procedure enables us to handle all possible NPI isomers, it is impractical to generate a distance matrix concerned with enormous NPI isomers. For example, stilbene-like chemical species ($C_{14}H_{12}$) has $(14! \times 12! \times 2)$ NPI isomers. However, NPI isomerization reactions such as substitution between distant atoms or atoms within a chemically stable group (e.g., benzene ring) have very high energy barriers; therefore, it is sufficient to consider only the easily generated NPI isomers in the actual analysis. In this chapter, I generate the NPI-restricted distance matrix concerned with 16 $(= 2^2 \times 2 \times 2)$ NPI isomers produced by the rotation of two phenyl rings, the inversion operation, and the atom-map flipping, which is the reflection operation on the atom-mapping around the C=C bond. Here, it is significant to emphasize the difference between the inversion operation and the atom-map flipping. As shown in Figure 6.1, S_1-MIN$_{twist}$ has the C2-Ph group rotated to the front side of the paper and then becomes pyramidal around C2. The inversion operation to S_1-MIN$_{twis}$ produces the chiral isomer rotated the C2-Ph group to the back side of the paper, with the pyramidal part around C2. In contrast, the atom-map flipping produces the NPI isomer rotated the C1-Ph group to the back side of the paper, with the pyramidal part around C1.

6.3 Results and Discussion

6.3.1 Ground-state Potential Energy Landscape

First, I focus on the ground-state molecular structures in Table 6.1. **Figure 6.2a** shows the ground-state two-dimensional reaction route map for SB determined by the CMDS method, including three S_0-MINs (denoted by squares), two S_0-TSs (denoted by larger circles), three S_1/S_0-CIs (denoted by diamonds), and five S_0-Paths (denoted by lines with smaller circles), in total, 93 structures. The edge colors mean PES types of each structure, and dark blue and green denote the S_0-PES and the crossing point between the S_1- and the S_0-PESs, respectively. The color map also shows the potential energy on the S_0 state relative to S_0-MIN$_{trans}$. Hereafter, the principal coordinates given by the CMDS method are referred to as PCos. The proportions of variance for PCo1 and PCo2 (Λ_1, Λ_2), which evaluate the validation of dimensionality reduction, are (0.877, 0.057), and the cumulated proportion is 0.932. Therefore, it is verified that two PCos sufficiently describe the ground-state reaction route map for SB. The PCo1 describes the structural changes along part of IRC starting from S_0-TS$_{cis\text{-}trans}$, correlating with the twisting motion on the central C=C bond related to the *cis-trans* isomerization. The PCo2 varies along both the DHP side of IRC starting from S_0-TS$_{cis\text{-}\mathrm{DHP}}$ and the *trans* region of IRC starting from S_0-TS$_{cis\text{-}trans}$. These structural changes accompany a motion to align two phenyl groups on the same plane as much as possible, suggesting that the PCo2 cannot be expressed in simple internal coordinates. Indeed, as shown in Figure 6.1, the two phenyl groups in S_1/S_0-CI$_{twist1}$ and S_1/S_0-CI$_{twist2}$ (large PCo2 structures) are pseudo-orthogonal, whereas those in S_0-MIN$_{\mathrm{DHP}}$ and S_0-MIN$_{trans}$ (small PCo2 structures) are pseudo-parallel and in the almost same plane.

Combining the dimensionality-reduced reaction space with multi-reaction paths and potential energy provides an intuitive insight into the geometrical features of PES. Figure 6.2b shows the ground-state potential energy landscape with the relative potential energy on the S_0 state as the third axis. In this landscape, the smaller circles corresponding to molecular structures along IRCs and meta-IRCs are dropped out to avoid complexity. By comparing barrier heights on two IRCs starting from S_0-$TS_{DHP\text{-}cis}$ and S_0-$TS_{cis\text{-}trans}$ in the S_0 energy landscape, it becomes immediately apparent that *cis*-SB is more likely to exhibit the *cis-trans* isomerization than the cyclization to DHP-form thermodynamically. However, since the reaction barriers are 73.4 and 57.2 kcal/mol for S_0-$TS_{DHP\text{-}cis}$ and S_0-$TS_{cis\text{-}trans}$, respectively, of course, these reactions seldom occur at room temperature. Although the visualized IRC profiles seem to sharply down from S_0-TSs in the energy landscape because of the data thinning, I verified that all molecular structures along the IRC starting from S_0-$TS_{cis\text{-}trans}$ provide the IRC profile smoothly going down the S_0-PES. Figure 6.2 also includes three meta-IRCs starting from three S_1/S_0-CIs corresponding to the sloped CIs, which have only one meta-IRC descending toward the S_0-PES. The meta-IRC starting from S_1/S_0-CI_{DHP} reaches S_0-MIN_{cis}, reflecting that S_1/S_0-CI_{DHP} is located on the *cis* side from S_0-$TS_{DHP\text{-}cis}$; in other words, the potential valley along the IRC starting from TS to *cis*-region induces the meta-IRC to proceed toward the *cis*-region. For the same reason, the meta-IRCs starting from S_1/S_0-CI_{twist1} and S_1/S_0-CI_{twist2} proceed to the *trans*-region on the S_0-PES. Finally, those paths join the IRC and reach S_0-MIN_{trans}.

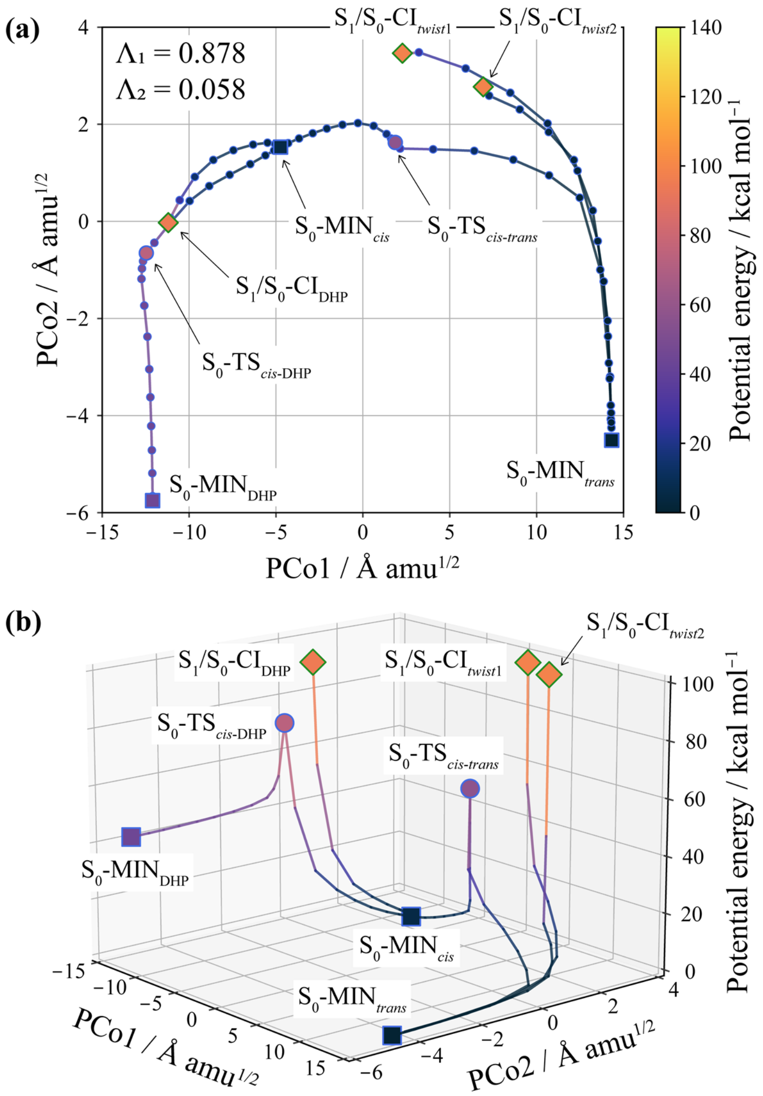

Figure 6.2. The ground-state reaction route map for SB by the CMDS method: (a) two-dimensional principal coordinate space and (b) potential energy landscape. S_0-MINs, S_0-TSs, and S_1/S_0-CIs are denoted by, respectively. The molecular structures along IRCs and meta-IRCs are interpolated by single lines and are denoted by small circles in (a). The edge colors mean PES types of each structure, and dark blue and green denote the S_0-PES and the crossing point between the S_1- and the S_0-PESs, respectively. The color map also shows the potential energy on the S_0 state relative to S_0-MIN*trans*.

6.3.2 Excited-state Potential Energy Landscape

Next, I construct the excited-state two-dimensional reaction route map for SB determined by the CMDS method; including six minima, three S_0-MINs and three S_1-MINs, (denoted by squares); two S_1-TSs (denoted by larger circles); three S_1/S_0-CIs (denoted by diamonds); and eight S_1-Paths (denoted by lines with small circles), in total, 135 structures (**Figure 6.3a**). Figure 6.3b also shows the excited-state potential energy landscape corresponding to Fig. 3a, where the smaller circles for molecule structures along reaction paths are dropped out. Note that S_0-$\mathrm{MIN_{DHP}}$, S_0-MIN_{cis}, and S_0-MIN_{trans} are also included as the Franck–Condon (FC) structures on the S_1-PES. The proportions of variance (Λ_1, Λ_2) are (0.859, 0.087), indicating that two PCos sufficiently reproduce the excited-state reaction route map for SB. Interestingly, the physical meanings of PCo1 and PCo2 correlate with the twisting angle on the central C=C bond and the alignment motion of two phenyl groups to the same plane as well as the ground-state reaction route map (Figure 6.2). This result suggests that both the ground- and the excited-state dimensionality-reduced reaction route maps can be determined together by common principal coordinates without significantly affecting the relative configuration.

Eight S_1-Paths consist of two IRCs starting from S_1-$\mathrm{TS}_{\mathrm{DHP}\text{-}twist}$ and S_1-$\mathrm{TS}_{twist\text{-}trans}$; three meta-IRCs starting from the FC points of S_0-$\mathrm{MIN_{DHP}}$, S_0-MIN_{cis}, and S_0-MIN_{trans}; three meta-IRCs starting from S_1/S_0-$\mathrm{CI_{DHP}}$, S_1/S_0-CI_{twist1}, and S_1/S_0-CI_{twist2}. The meta-IRC starting from S_0-MIN_{cis} joins the IRC starting from S_1-$\mathrm{TS}_{\mathrm{DHP}\text{-}twist}$, indicating that the potential valley along the IRC induces the initial direction of the meta-IRC. Also, the meta-IRC starting from S_0-MIN_{trans} reaches S_1-MIN_{trans} located very close to S_0-MIN_{trans}, as reported in the previous studies[1,11–13] The meta-IRC starting from S_1/S_0-$\mathrm{CI_{DHP}}$ reaches S_1-$\mathrm{MIN_{DHP}}$, and those starting from S_1/S_0-CI_{twist1} and S_1/S_0-CI_{twist2} reach both S_1-MIN_{twist}.

As shown in Figure 6.3b, because the potential energy for the FC point of S_0-MIN$_{cis}$ is higher than that for S_1/S_0-CIs, the ππ* excited *cis*-SB is energetically accessible to the S_1/S_0-crossing regions on the S_1-PES. The geometrical aspects of the reaction paths on the S_1-PES are clearly illustrated in the potential energy landscape (Figure 6.3b).

Experimental studies have supported that the photoisomerizations for *cis*- and *trans*-SB relax from the common *twist* region and have focused on the barrier existence from each FC point to the twist region. It has been reported that the ππ*-excited *cis*-SB can proceed to the *twist* region with a small barrier or barrierless, which reflects the ultrafast relaxation process with the fluorescence decay within 2.0 ps.[5] Harabuchi *et al.* theoretically clarified that the ππ*-excited *cis*-SB prefers the photoisomerization reaction toward *twist*-form by the initial excited-state dynamics and smoothly relaxes to the ground state through the conical intersection in the *twist* region.[21] From these results and our potential energy landscape in Figure 6.3b, it is suggested that the observed small barrier corresponds to the reaction barrier with S_1-TS$_{\mathrm{DHP}\text{-}twist}$ (6.6 kcal/mol from S_1-MIN$_{\mathrm{DHP}}$ to S_1-MIN$_{twist}$) and/or the energy differences between S_1-MIN$_{twist}$ and two CIs (S_1/S_0-CI$_{twist1}$ and S_1/S_0-CI$_{twist2}$). On the other hand, *trans*-SB has the planar minimum on the S_1-PES, and therefore there is a small barrier along reaction coordinates from the planar minimum to the *twist* region, yielding the vibrational relaxations within 25 ps.[11] As shown in Figure 6.3, the planar minimum, S_1-MIN$_{trans}$, is located near the FC point of S_0-MIN$_{trans}$, and *trans*-*twist* isomerization requires a potential barrier of 4.1 kcal/mol *via* S_1-TS$_{twist\text{-}trans}$. This activation barrier supports the observation of the relatively long lifetime in the *trans*-SB case.

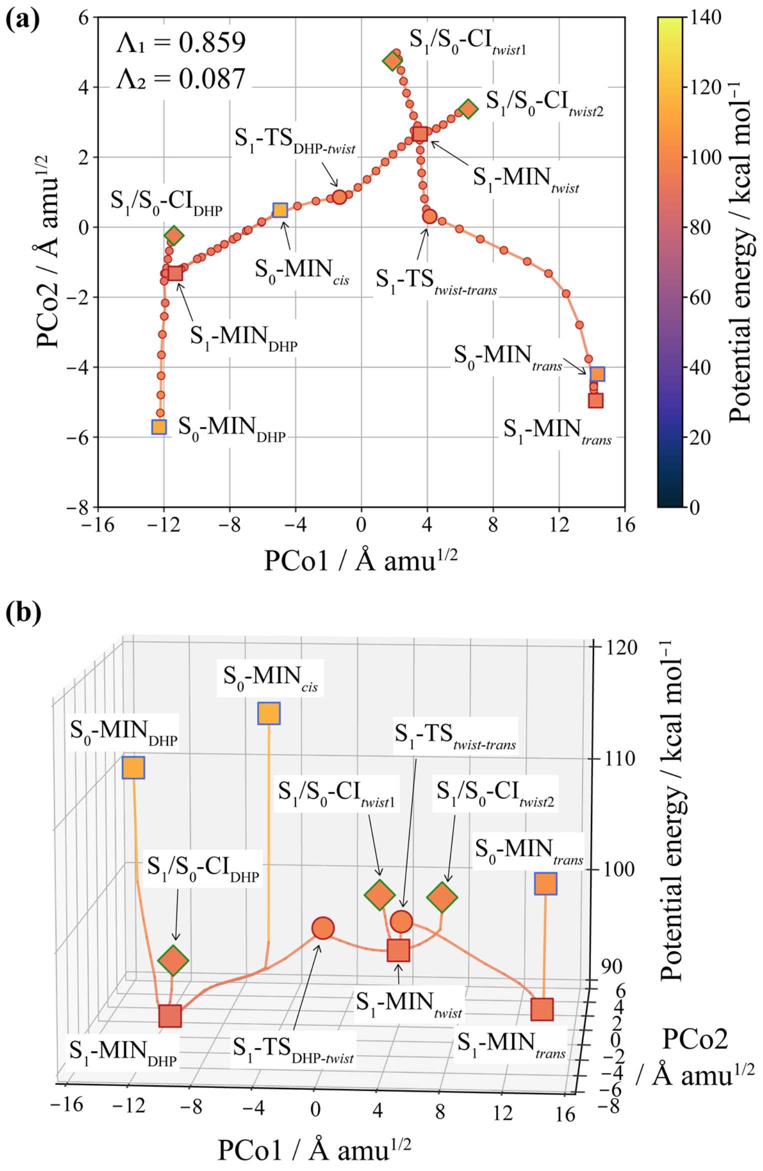

Figure 6.3. The excited-state reaction route map for SB: (a) two-dimensional principal coordinate space and (b) potential energy landscape. Minima, S_1-TSs, and S_1/S_0-CIs are denoted by squares, circles, and diamonds, respectively. The molecular structures along IRCs and meta-IRCs are interpolated by single lines and are denoted by small circles in (a). The edge colors mean PES types of each structure, and dark blue, dark red, and green denote the S_0-PES, the S_1-PES, and the crossing point between the S_1- and the S_0-PESs, respectively. The color map shows the potential energy relative to S_0-MIN*trans*.

6.3.3 Multi-state Potential Energy Landscape

To clarify the comprehensive photoreaction paths based on both the ground and excited states, I construct the "*multi-state*" reaction route map and potential energy landscape by the CMDS method. In **Figure 6.4a**, there are six minima (three S_0-MINs and three S_1-MINs) denoted by squares, four TSs (two S_0-TSs and two S_1-TSs) denoted by larger circles, three S_1/S_0-CIs denoted by diamonds, and 13 reaction paths (five S_0-Paths and eight S_1-Paths) denoted by lines with smaller circles, in total, 228 structures. Fig. 4b also shows the excited-state potential energy landscape, where the smaller circles for molecule structures along reaction paths are dropped out. The proportions of variance (Λ_1, Λ_2) are (0.863, 0.071), indicating that two PCos sufficiently reproduce the multi-state reaction space. Similar to what I discussed above, PCo1 and PCo2 mainly correlate with the twisting motion on the central C=C bond and the alignment motion of two phenyl groups, respectively. In order to explicitly illustrate the FC points on the S_1-PES, each S_0-MIN has two data points corresponding to the minimum structure on the S_0-PES and the FC point on the S_1-PES, which are overlapped in Figure 6.4a.

Many researchers have recognized that structural changes along the twisting angle on the central C=C bond of SB stabilize the S_1-PES around S_0-TS$_{cis\text{-}trans}$, and thus, they have interpreted that the ππ*-excited *cis*-SB undergoes the *cis-trans* photoisomerization with non-radiative decay through the stable region on the S_1-PES.[3,5,10,13,18,43,44] However, such a schematic picture is just a one-dimensional energy profile extracted from a multidimensional potential energy surface according to chemical intuition, and nobody can guarantee that it is suitable to discuss the chemical reaction. A dimensionality-reduced map constructed by the CMDS method is mathematically guaranteed to visualize a mutual distance relationship for full-dimensional data into lower-dimensional space as much as possible. Consequently, the dimensionality reduction map and its potential energy landscape are immensely helpful tools for describing a chemical reaction process. As shown in Figure 6.4a, the *cis-trans* photoisomerization reaction proceeds as increasing PCo1, which correlates with the twisting motion on the C=C bond, and the S_1-PES stabilizes while the S_0-PES destabilizes around PCo1 = 0 ~ 4 Å amu$^{1/2}$. Focusing on PCo1 with 86.3 % of the amount of information, S_0-TS$_{cis\text{-}trans}$ is located very close to S_1-MIN$_{twist}$, assumed in the traditional one-dimensional scheme. However, Figure 6.4b reveals that the potential energy levels for S_1- and S_0-PESs get zero at S_1/S_0-CI$_{twist1}$ and S_1/S_0-CI$_{twist2}$, which is located far from S_0-TS$_{cis\text{-}trans}$, indicating that the non-radiative relaxation to the ground state passes through not the avoid crossing near S_1-MIN$_{twist}$ but the sloped conical intersections. In contrast, S_0-TS$_{\mathrm{DHP}\text{-}cis}$ and S_1-MIN$_{\mathrm{DHP}}$ are energetically close and are located close to each other, reflecting the DHP-form rigidity. Such detailed geometrical knowledge of potential energy landscape cannot capture from the traditional reaction scheme, and the reduced-dimensionality reaction route map and potential energy landscape provide fruitful insight concerned with chemical reaction processes.

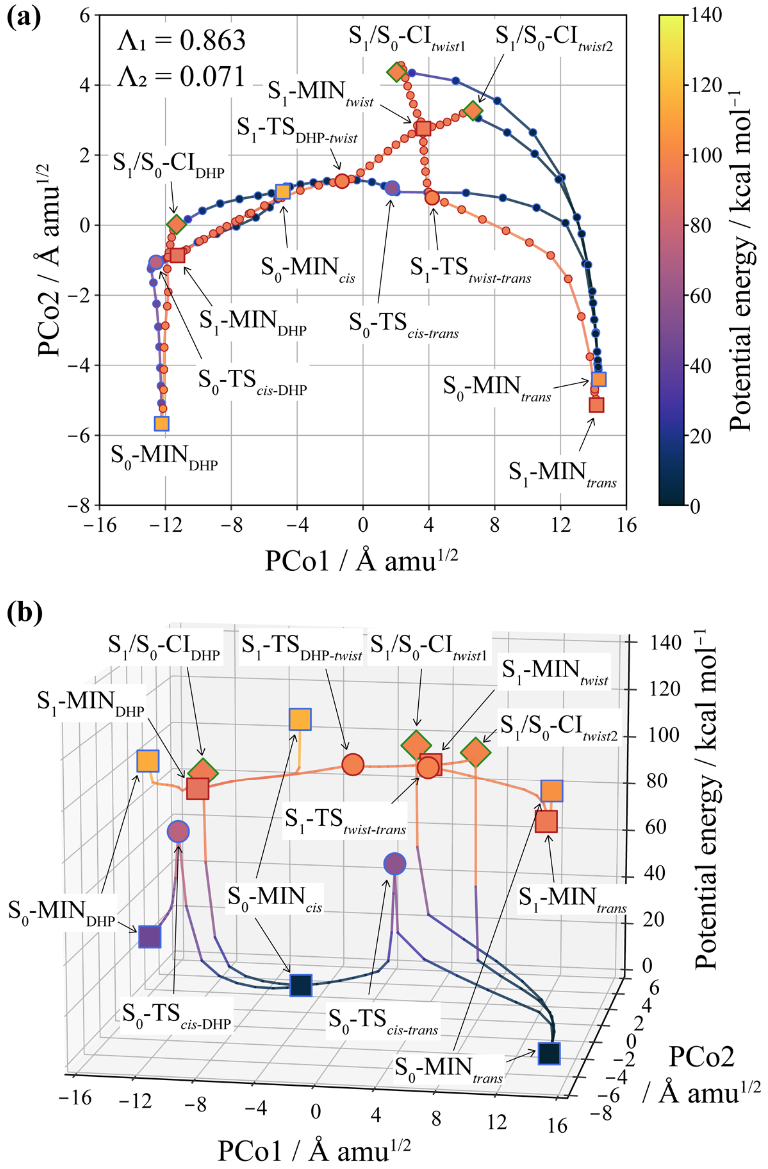

Figure 6.4. The multi-state reaction route map for SB: (a) two-dimensional principal coordinate space and (b) potential energy landscape. Minima, four TSs, and S_1/S_0-CIs are denoted by squares, circles, and diamonds, respectively. The molecular structures along IRCs and meta-IRCs are interpolated by single lines and are denoted by small circles in (a). The edge colors mean PES types of each structure, and dark blue, dark red, and green denote the S_0-PES, the S_1-PES, and the crossing point between the S_1- and the S_0-PESs, respectively. The color map also shows the potential energy relative to S_0-MIN*trans*.

6.3.4 On-the-fly Trajectory Analysis based on Multi-state Landscape

Next, I discuss the *cis*-SB's non-radiative decay mechanisms on both the S_1- and the S_0-PESs based on the dimensionality-reduced map. **Figure 6.5** shows three on-the-fly trajectories projected onto the multi-state reaction route map (Figure 6.4a) and the potential energy landscape (Figure 6.4b) by the out-of-sample technique[32,37], and Figure 6.5d shows the trajectory also visualized in Figure 6.5c. The molecular structures along the trajectories are denoted by small circles and are interpolated by single lines and blue highlighted lines; and the initial point, the hopping point from the S_1-PES to the S_0-PES, and the terminal point for the trajectory are denoted by cross marks. The color map and the third axis of Figure 6.5d indicate the relative potential energy for both the reaction route map and the on-the-fly trajectory. As mentioned in Section 6.2, I switched the target state for the excited-state on-the-fly MD simulation to the ground state when the energy difference between the S_1- and the S_0-PESs becomes 0.2 eV or less.

Figure 6.5a shows the on-the-fly trajectory relaxed from the S_1-DHP region to the ground state. After the ππ* excitation, this trajectory proceeds to the *twist* region on the S_1-PES and reaches near $S1/S_0\text{-CI}_{twist2}$. However, it cannot enter the CI region and quickly returns to the DHP region with passing through $S_1\text{-TS}_{\text{DHP-}twist}$. Then, it relaxes from near $S_1/S_0\text{-CI}_{\text{DHP}}$ to the S_0-PES and finally is trapped in the S_0-DHP region without crossing over $S_0\text{-TS}_{\text{DHP-}cis}$. Interestingly, all trajectories relaxed from the S_1-DHP region are trapped in the S_0-DHP region, although the hopping points of several trajectories are located at the *cis* side of the IRC starting from $S_0\text{-TS}_{\text{DHP-}cis}$. This result suggests that trajectories relaxed to the ground state prefer to enter the S_0-DHP region with keeping their velocity direction on the S_1-PES and then are trapped in the S_0-DHP region due to the relatively high energy barrier of $S_0\text{-TS}_{\text{DHP-}cis}$. Even though the relaxed classical trajectories have considerably higher potential energy than the reaction paths on the S_0-PES, the internal energy of the trajectory should be focused in the reactive direction in order to cross over the S_0-TS$_{\text{DHP-}cis}$.

Figure 6.5b and c show two on-the-fly trajectories that are relaxed from the S_1-*twist* region to the ground state. In Figure 6.5b, the trajectory directly reaches the CI region in the S_1-*twist* region and then relaxes to the S_0-PES. After that, it proceeds toward the S_0-*trans* direction due to the velocity at the hopping point, but it returns and finally reaches the S_0-*cis* region with crossing over S_0-TS$_{cis\text{-}trans}$. In Figure 6.5c, first, the trajectory proceeds to the S_1-DHP region as the meta-IRC starting from the FC point of S_0-MIN$_{cis}$, but it returns to the *twist* region and enters the CI region near S_1/S_0-CI$_{twist1}$. After the relaxation, it goes from the S_0-*cis* region to the S_0-*trans* region and then finally back to the S_0-*cis* region. In contrast to Figure 6.5a, these trajectories travel between *cis* and *trans* regions on the S_0-PES because the energy barrier of S_0-TS$_{cis\text{-}trans}$ is smaller than the potential energy of each trajectory. Indeed, Figure 6.5d indicates that the potential energy of the trajectory, which is illustrated in Figure 6.5c, is considerably larger than that of the reaction route maps for both S_1- and the S_0-PESs. Applying the dimensionality-reduced multi-state reaction route map to the on-the-fly trajectory analysis method enables us to clarify the comprehensive photochemical reaction processes based on the multi-state potential energy surfaces that are the stage for chemical reactions.

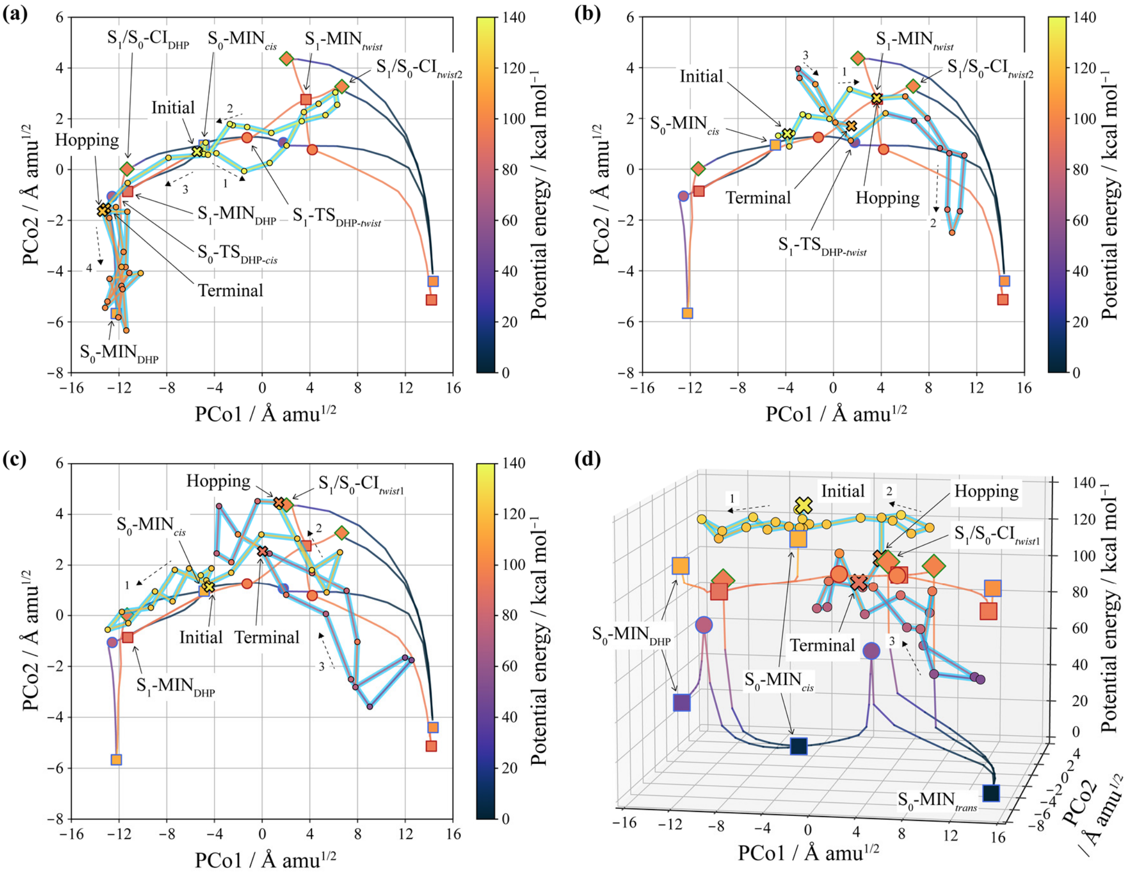

Figure 6.5. The on-the-fly trajectories projected onto (a-c) two-dimensional multi-state principal coordinate space (Figure 6.4a) and (d) potential energy landscape (Figure 6.4b). The molecular structures along the trajectories are denoted by small circles and are interpolated by single lines and blue highlighted lines. The initial point, the hopping point from the S_1-PES to the S_0-PES, and the terminal point for the trajectory are denoted by cross marks. The color map and the third axis of Fig.5d indicate the relative potential energy (S_0-MIN$_{trans}$ is set to be 0.0) for both the reaction route map and the on-the-fly trajectory.

6.3.5 Excited-state Reaction Route Maps of Stilbene Derivatives

Finally, I attempt to compare the excited-state reaction route maps for *cis*-stilbene (SB), α-methyl-cis-stilbene (mSB), and 1,1'-dimethyl-cis-stilbene (dmSB). In the previous studies, the difference of excited-state reaction mechanisms was discussed by comparing the meta-IRC profiles projected onto the two-dimensional space determined by two internal coordinates, a twisting angle of C=C and a bond length involved the cyclization.[21,24,25] As mentioned in **Chapter 5**, such an internal-coordinate-based dimensionality-reduction approach requires chemical intuition, but it is feasible to compare the different molecular systems with a different number of atoms in the common coordinate space. On the other hand, the CMDS method enables us to construct the principal coordinate space without chemical intuition, but it cannot directly apply to such different molecules because the linear distance matrix, which requires by the CMDS method, cannot define for the case of a different number of atoms. To overcome this problem, I attempt to define a dimensionality-reduced reaction space from a part of different molecular systems. In this chapter, I select the $C_{14}H_{10}$ part with the central C=C bond and two phenyl groups from SB, mSB, and dmSB, which is called the framework part hereafter. **Figure 6.6a** is the two-dimensional CMDS subspace determined by the framework parts of ten minima for SB, mSB, and dmSB: three *cis*-forms in the S_0 state (denoted by *cis*-SB(S_0), *cis*-mSB(S_0), and *cis*-dmSB(S_0)); one *cis*-form in the S_1 state (denoted by *cis*-dmSB(S_1)); three DHP-forms in the S_1 state (denoted by DHP-SB, DHP-mSB, and DHP-dmSB); and three *twist*-forms in the S_1 state (denoted by *twist*-SB, *twist*-mSB, and *twist*-dmSB). Note that only the dmSB has a *cis*-form in the S_1 state. Figure 6.6a is the common dimensionality-reduced reaction space for SB, mSB, and dmSB determined by ten minima corresponding to the termination points in the target reaction paths on the S_1-PES, providing the minimal reaction space. The proportions of variance (Λ_1, Λ_2) for PCo1 and PCo2 are (0.875, 0.085), and the cumulated proportion is 0.960. Figure 6.6a clarifies that although almost all structures are located in the region of $-2 <$ PCo2 < 1, only *cis*-dmSB(S_0) is far from other structures.

To compare the geometrical features of the S_1-PESs, I project the reaction paths on the S_1-PESs for SB, mSB, and dmSB onto the common CMDS subspace (Figure 6.6a) using the out-of-sample technique[32,37]. Figure 6.6b shows the excited-state reaction route map for SB, including *cis*-SB(S_0); DHP-SB; *twist*-SB; the IRC starting from S_1-TS$_{\text{DHP-}\textit{twist}}$; the meta-IRC starting from the FC point of *cis*-SB(S_0), in total, 185 framework parts. Note that this analysis uses all molecular structures along the IRC and the meta-IRC paths without thinning out. Similarly, Figure 6.6c shows the excited-state reaction route map for mSB, including *cis*-mSB(S_0); DHP-mSB; *twist*-mSB; the IRC starting from S_1-TS$_{\text{DHP-}\textit{twist}}$; the meta-IRC starting from the FC point of *cis*-mSB(S_0), in total, 265 framework parts. Also, Figure 6.6d shows the excited-state reaction route map for dmSB, including *cis*-dmSB(S_0); *cis*-dmSB(S_1); DHP-dmSB; *twist*-dmSB; two IRCs starting from S_1-TS$_{\textit{cis}\text{-DHP}}$ and S_1-TS$_{\text{DHP-}\textit{twist}}$; the meta-IRC starting from the FC point of *cis*-dmSB(S_0), in total, 235 framework parts. The previous studies analyzed the photochemical reaction dynamics after the ππ* excitation of SB, mSB, and dmSB and reported that the dominant products were *twist*-forms for SB and mSB cases, whereas it was DHP-form for dmSB case.[21,24,25] Since the excited-state dynamics for the vertically-excited molecule are driven by the potential gradient around the FC point, the dynamical behaviors are sensitive to the shape of the excited-state PES. Figure 6.6b-d show that although the dimensionally-reduced reaction route maps for SB and mSB are very similar, dmSB is significantly different from the others. Such nature is qualitatively consistent with the excited-state dynamics of stilbene derivatives discussed in previous studies.

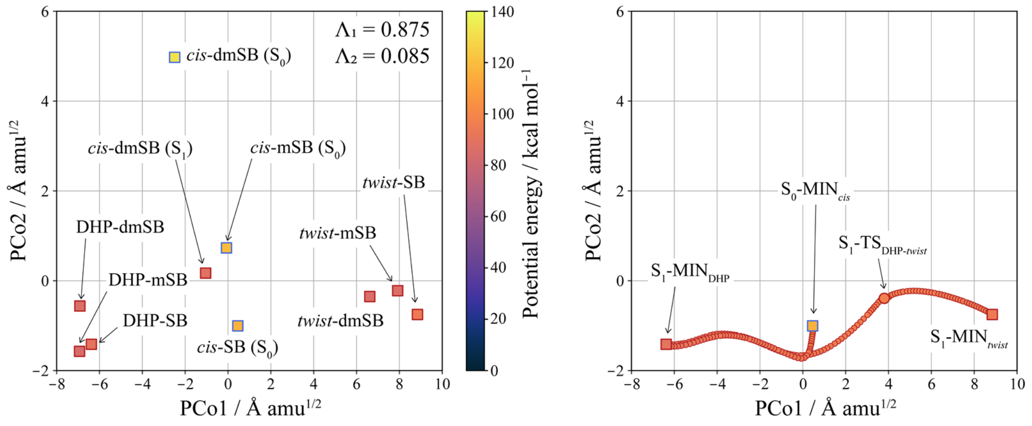

(a) S_1-PES on two-dimensional CMDS space

(b) S_1-PES of stilbene (SB)

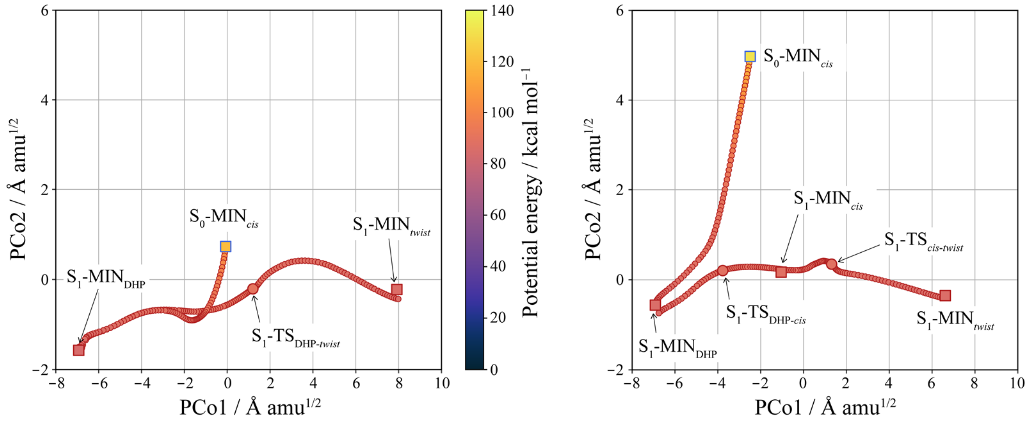

(c) S_1-PES of α-methly-stilebene (mSB)

(d) S_1-PES of 1,1′-dimethly-stilebene (dmSB)

Figure 6.6. a) The two-dimensional excited-state reaction plane determined by the CMDS method with ten minima for the framework parts of *cis*-stilbene (SB), α-methyl-*cis*-stilbene (mSB), and 1,1'-dimethyl-*cis*-stilbene (dmSB): three S_0-minima for the *cis*-forms, seven S_1-minima for the *cis*-, DHP-, and *twist*-forms. The dimensionality-reduced excited-state reaction route maps projected onto (a) by using the out-of-sample technique: (b) SB, (c) mSB, and (d) dmSB. In (b-d), only the relevant molecular structures are shown. The edge colors mean PES types of each structure, and dark blue and dark red denote the S_0-PES and the S_1-PES, respectively. The color map also indicates the potential energy relative to each *trans*-form on the S_0 state.

6.4 Conclusion

Cis-stilbene is a fundamental molecule in which the *cis*-*trans* photoisomerization and the photocyclization reactions compete after $\pi\pi^*$ excitation, and the decay mechanism is of great experimental and theoretical interest. The excited-state dynamics for stilbenes derivatives have been discussed on two-dimensional reaction surfaces defined by internal coordinates chosen by chemical intuition, but these choices are not unique. To avoid such ambiguity, I applied the classical multidimensional scaling (CMDS) method, one of the dimensionality reduction methods, to the photoreaction for *cis*-stilbene and constructed the reduced-dimensionally reaction route map and potential energy landscape without chemical intuition.

The ground-state reaction route map determined by CMDS can be adequately represented by two principal coordinates, suggesting that those two principal coordinates correlate with the twisting angle about the C=C bond and the planarity of the two phenyl groups, respectively. In this chapter, I also generated the excited-state potential energy landscape where the third axis of the relative potential energy is added to the two-dimensional excited-state reaction route map. This excited-state energy landscape clarified the relative locations of all stable structures and conical intersections and verified the experimentally-predicted energy barriers along the structural changes from the Franck–Condon points of *cis*- and *trans*-forms.

Furthermore, I proposed the reduced-dimensionality multi-state reaction route map by applying the CMDS method to a set of molecular structures in both ground and excited states, which enables us to discuss comprehensive photochemical reaction processes. In order to analyze dynamical reaction behaviors, I performed the on-the-fly molecular dynamics simulations corresponding to the non-radiative decay processes and then projected these trajectories onto the multi-state energy landscape determined by the CMDS method. From these results, it was revealed that the trajectories relaxed from the DHP region on the excited state were trapped in the DHP region on the ground state due to the high energy barrier of the transition state connecting the DHP- and the *cis*-forms. In contrast, it was also revealed that the trajectories relaxed from the *twist* region widely travel on the ground-state potential energy surface with crossing over the transition state connecting the *cis*- and the *trans*-forms.

I also constructed reduced-dimensionally excited-state reaction route maps determined by the framework parts of stilbene, α-methyl-stilbene, and 1,1'-dimethylstilbene and discussed excited-state branching reactions for these molecular systems. Such an approach makes it possible to compare the structural features of molecular systems with a different number of atoms in the same coordinate space. The features of the reaction route maps visualized by CMDS were qualitatively consistent with the tendency of their excited state dynamics.

Through this chapter, I proposed the reduced-dimensionally multi-state potential energy landscape. This approach provides a strategy to comprehensively analyze complicated photochemical reactions based on the ground- and excited-state PES. The proposed technique will help to understand the excited state dynamics regarding photochemical reactions governed by conformational features of a molecular system.[45,46]

6.5 References

(1) Waldeck, D. H. Photoisomerization Dynamics of Stilbenes. *Chem. Rev.* **1991**, *91*, 415–436.

(2) Muszkat, K. A.; Fischer, E. Structure, Spectra, Photochemistry, and Thermal Reactions of the 4a,4b-Dihydrophenanthrenes. *J. Chem. Soc. B Phys. Org.* **1967**, No. 0, 662.

(3) Saltiel, J. Perdeuteriostilbene. The Role of Phantom States in the Cis-Trans Photoisomerization of Stilbenes. *J. Am. Chem. Soc.* **1967**, *89*, 1036–1037.

(4) Greene, B. I.; Farrow, R. C. Subpicosecond Time Resolved Multiphoton Ionization: Excited State Dynamics of Cis-stilbene under Collision Free Conditions. *J. Chem. Phys.* **1983**, *78*, 3336–3338.

(5) Todd, D. C.; Jean, J. M.; Rosenthal, S. J.; Ruggiero, A. J.; Yang, D.; Fleming, G. R. Fluorescence Upconversion Study of Cis -stilbene Isomerization. *J. Chem. Phys.* **1990**, *93*, 8658–8668.

(6) Kovalenko, S. A.; Dobryakov, A. L.; Ioffe, I.; Ernsting, N. P. Evidence for the Phantom State in Photoinduced Cis–Trans Isomerization of Stilbene. *Chem. Phys. Lett.* **2010**, *493*, 255–258.

(7) Petek, H.; Yoshihara, K.; Fujiwara, Y.; Lin, Z.; Penn, J. H.; Frederick, J. H. Is the Nonradiative Decay of S_1 Cis-Stilbene Due to the Dihydrophenanthrene Isomerization Channel? Suggestive Evidence from Photophysical Measurements on 1,2-Diphenylcycloalkenes. *J. Phys. Chem.* **1990**, *94*, 7539–7543.

(8) Rodier, J. M.; Myers, A. B. Cis-Stilbene Photochemistry: Solvent Dependence of the Initial Dynamics and Quantum Yields. *J. Am. Chem. Soc.* **1993**, *115*, 10791–10795.

(9) Takeuchi, S.; Ruhman, S.; Tsuneda, T.; Chiba, M.; Taketsugu, T.; Tahara, T. Spectroscopic Tracking of Structural Evolution in Ultrafast Stilbene Photoisomerization. *Science* **2008**, *322*, 1073–1077.

(10) Nakamura, T.; Takeuchi, S.; Taketsugu, T.; Tahara, T. Femtosecond Fluorescence Study of the Reaction Pathways and Nature of the Reactive S_1 State of Cis-Stilbene. *Phys. Chem. Chem. Phys.* **2012**, *14*, 6225.

(11) Greene, B. I.; Hochstrasser, R. M.; Weisman, R. B. Spectroscopic Study of the Picosecond Photoisomerization of Stilbene. *Chem. Phys. Lett.* **1979**, *62*, 427–430.

(12) Baskin, J. S.; Bañares, L.; Pedersen, S.; Zewail, A. H. Femtosecond Real-Time Probing of Reactions. 20. Dynamics of Twisting, Alignment, and IVR in the

Trans -Stilbene Isomerization Reaction. *J. Phys. Chem.* **1996**, *100*, 11920–11933.

(13) Syage, J. A.; Lambert, W. R.; Felker, P. M.; Zewail, A. H.; Hochstrasser, R. M. Picosecond Excitation and TRANS-CIS Isomerization of Stilbene in a Supersonic Jet: Dynamics and Spectra. *Chem. Phys. Lett.* **1982**, *88*, 266–270.

(14) Quenneville, J.; Martínez, T. J. Ab Initio Study of Cis−Trans Photoisomerization in Stilbene and Ethylene. *J. Phys. Chem. A* **2003**, *107*, 829–837.

(15) Amatatsu, Y. Ab Initio Study on the Electronic Structures of Stilbene at the Conical Intersection. *Chem. Phys. Lett.* **1999**, *314*, 364–368.

(16) Minezawa, N.; Gordon, M. S. Photoisomerization of Stilbene: A Spin-Flip Density Functional Theory Approach. *J. Phys. Chem. A* **2011**, *115*, 7901–7911.

(17) Ioffe, I. N.; Granovsky, A. A. Photoisomerization of Stilbene: The Detailed XMCQDPT2 Treatment. *J. Chem. Theory Comput.* **2013**, *9*, 4973–4990.

(18) Fuß, W.; Kosmidis, C.; Schmid, W. E.; Trushin, S. A. The Photochemicalcis–Trans Isomerization of Free Stilbene Molecules Follows a Hula-Twist Pathway. *Angew. Chemie Int. Ed.* **2004**, *43*, 4178–4182.

(19) Bearpark, M. J.; Bernardi, F.; Clifford, S.; Olivucci, M.; Robb, M. A.; Vreven, T. Cooperating Rings in Cis -Stilbene Lead to an S 0 /S 1 Conical Intersection. *J. Phys. Chem. A* **1997**, *101*, 3841–3847.

(20) Dou, Y.; Allen, R. E. Dynamics of the Photocyclization of Cis -Stilbene to Dihydrophenanthrene. *J. Mod. Opt.* **2004**, *51*, 2485–2491.

(21) Harabuchi, Y.; Keipert, K.; Zahariev, F.; Taketsugu, T.; Gordon, M. S. Dynamics Simulations with Spin-Flip Time-Dependent Density Functional Theory: Photoisomerization and Photocyclization Mechanisms of Cis- Stilbene in Ππ* States. *J. Phys. Chem. A* **2014**, *118*, 11987–11998.

(22) Weir, H.; Williams, M.; Parrish, R. M.; Hohenstein, E. G.; Martínez, T. J. Nonadiabatic Dynamics of Photoexcited Cis -Stilbene Using Ab Initio Multiple Spawning. *J. Phys. Chem. B* **2020**, *124*, 5476–5487.

(23) Berndt, F.; Dobryakov, A. L.; Quick, M.; Mahrwald, R.; Ernsting, N. P.; Lenoir, D.; Kovalenko, S. A. Long-Lived Perpendicular Conformation in the Photoisomerization Path of 1,1′-Dimethylstilbene and 1,1′-Diethylstilbene. *Chem. Phys. Lett.* **2012**, *544*, 39–42.

(24) Harabuchi, Y.; Yamamoto, R.; Maeda, S.; Takeuchi, S.; Tahara, T.; Taketsugu, T. Ab Initio Molecular Dynamics Study of the Photoreaction of 1,1′-Dimethylstilbene upon $S_0 \rightarrow S_1$ Excitation. *J. Phys. Chem. A* **2016**, *120*, 8804–8812.

(25) Tsutsumi, T.; Harabuchi, Y.; Yamamoto, R.; Maeda, S.; Taketsugu, T. On-the-

Fly Molecular Dynamics Study of the Excited-State Branching Reaction of α-Methyl-Cis-Stilbene. *Chem. Phys.* **2018**, *515*, 564–571.

(26) Kokado, K.; Machida, T.; Iwasa, T.; Taketsugu, T.; Sada, K. Twist of C═C Bond Plays a Crucial Role in the Quenching of AIE-Active Tetraphenylethene Derivatives in Solution. *J. Phys. Chem. C* **2018**, *122*, 245–251.

(27) Komatsuzaki, T.; Hoshino, K.; Matsunaga, Y.; Rylance, G. J.; Johnston, R. L.; Wales, D. J. How Many Dimensions Are Required to Approximate the Potential Energy Landscape of a Model Protein? *J. Chem. Phys.* **2005**, *122*, 084714.

(28) Hare, S. R.; Bratholm, L. A.; Glowacki, D. R.; Carpenter, B. K. Low Dimensional Representations along Intrinsic Reaction Coordinates and Molecular Dynamics Trajectories Using Interatomic Distance Matrices. *Chem. Sci.* **2019**, *10*, 9954–9968.

(29) Pisani, P.; Caporuscio, F.; Carlino, L.; Rastelli, G. Molecular Dynamics Simulations and Classical Multidimensional Scaling Unveil New Metastable States in the Conformational Landscape of CDK2. *PLoS One* **2016**, *11*, 1–23.

(30) Li, X.; Xie, Y.; Hu, D.; Lan, Z. Analysis of the Geometrical Evolution in On-the-Fly Surface-Hopping Nonadiabatic Dynamics with Machine Learning Dimensionality Reduction Approaches: Classical Multidimensional Scaling and Isometric Feature Mapping. *J. Chem. Theory Comput.* **2017**, *13*, 4611–4623.

(31) Tsutsumi, T.; Ono, Y.; Arai, Z.; Taketsugu, T. Visualization of the Intrinsic Reaction Coordinate and Global Reaction Route Map by Classical Multidimensional Scaling. *J. Chem. Theory Comput.* **2018**, *14*, 4263–4270.

(32) Tsutsumi, T.; Ono, Y.; Arai, Z.; Taketsugu, T. Visualization of the Dynamics Effect: Projection of on-the-Fly Trajectories to the Subspace Spanned by the Static Reaction Path Network. *J. Chem. Theory Comput.* **2020**, *16*, 4029–4037.

(33) Shi, W.; Jia, T.; Li, A. Quasi-Classical Trajectory Analysis with Isometric Feature Mapping and Locally Linear Embedding: Deep Insights into the Multichannel Reaction on an NH 3 + (4 A) Potential Energy Surface. *Phys. Chem. Chem. Phys.* **2020**, *22*, 17460–17471.

(34) Torgerson, W. S. Multidimensional Scaling: I. Theory and Method. *Psychometrica* **1952**, *17*, 401–419.

(35) Cox, T.; Cox, M. *Multidimensional Scaling, Second Edition*, 2nd Edit.; C&H/CRC Monographs on Statistics & Applied Probability; Chapman and Hall/CRC: New York, 2000; Vol. 88.

(36) Härdle, W. K.; Simar, L. *Applied Multivariate Statistical Analysis*, 3rd Edit.; Springer Berlin Heidelberg: Berlin, Heidelberg, 2015.

(37) Trosset, M. W.; Priebe, C. E. The Out-of-Sample Problem for Classical Multidimensional Scaling. *Comput. Stat. Data Anal.* **2008**, *52*, 4635–4642.

(38) Schmidt, M. W.; Baldridge, K. K.; Boatz, J. A.; Elbert, S. T.; Gordon, M. S.; Jensen, J. H.; Koseki, S.; Matsunaga, N.; Nguyen, K. A.; Su, S.; et al. General Atomic and Molecular Electronic Structure System. *J. Comput. Chem.* **1993**, *14*, 1347–1363.

(39) Maeda, S.; Harabuchi, Y.; Takagi, M.; Saita, K.; Suzuki, K.; Ichino, T.; Sumiya, Y.; Sugiyama, K.; Ono, Y. Implementation and Performance of the Artificial Force Induced Reaction Method in the GRRM17 Program. *J. Comput. Chem.* **2018**, *39*, 233–250.

(40) Maeda, S.; Harabuchi, Y.; Taketsugu, T.; Morokuma, K. Systematic Exploration of Minimum Energy Conical Intersection Structures near the Franck–Condon Region. *J. Phys. Chem. A* **2014**, *118*, 12050–12058.

(41) Harabuchi, Y.; Okai, M.; Yamamoto, R.; Tsutsumi, T.; Ono, Y.; Taketsugu, T. SPPR. Hokkaido University: Sapporo, Japan 2020.

(42) Tsutsumi, T.; Harabuchi, Y.; Ono, Y.; Maeda, S.; Taketsugu, T. Analyses of Trajectory On-the-Fly Based on the Global Reaction Route Map. *Phys. Chem. Chem. Phys.* **2018**, *20*, 1364–1372.

(43) Repinec, S. T.; Sension, R. J.; Szarka, A. Z.; Hochstrasser, R. M. Femtosecond Laser Studies of the Cis-Stilbene Photoisomerization Reactions: The Cis-Stilbene to Dihydrophenanthrene Reaction. *J. Phys. Chem.* **1991**, *95*, 10380–10385.

(44) Pedersen, S.; Bañares, L.; Zewail, A. H. Femtosecond Vibrational Transition-state Dynamics in a Chemical Reaction. *J. Chem. Phys.* **1992**, *97*, 8801–8804.

(45) Kotani, R.; Liu, L.; Kumar, P.; Kuramochi, H.; Tahara, T.; Liu, P.; Osuka, A.; Karadakov, P. B.; Saito, S. Controlling the S_1 Energy Profile by Tuning Excited-State Aromaticity. *J. Am. Chem. Soc.* **2020**, *142*, 14985–14992.

(46) Kimura, R.; Kuramochi, H.; Liu, P.; Yamakado, T.; Osuka, A.; Tahara, T.; Saito, S. Flapping Peryleneimide as a Fluorogenic Dye with High Photostability and Strong Visible-Light Absorption. *Angew. Chemie Int. Ed.* **2020**, *59*, 16430–16435.

Chapter 7

General Conclusion

Both static reaction path analysis and *ab initio* molecular dynamics have been recognized as powerful tools to elucidate chemical reaction mechanisms theoretically. The global reaction route map (GRRM) method enabled us to systematically explore intrinsic reaction coordinates (IRCs), providing a "*global reaction route map*" concept. In reaction dynamics, the on-the-fly molecular dynamics (MD) simulation, including both the *ab initio* MD with the wave function theory and the first-principal MD with the density functional theory, has become a practical approach and has been applied to the ground- and excited-state chemical reactions. Up to now, although the static and dynamic analyses have been developed as independent methodologies, they are, in fact, closely related through the potential energy surface (PES) derived from the Born–Oppenheimer approximation. In this doctoral thesis, by combining these two approaches, I successfully developed the generalized *ab initio* MD analysis method based on the static reaction route map.

The on-the-fly trajectory provides a chemical reaction route traveling on the PES, but it is challenging to grasp a reaction mechanism and a driving force without chemical knowledge because a realistic chemical reaction involves multiple elementary reaction processes. In **Chapter 2**, to overcome such difficulties in analysis, I proposed the on-the-fly trajectory mapping method that analyzes the dynamical reaction process along the on-the-fly trajectory by referring to the static reaction route network. This mapping method requires a distance function, which is a time-series function of a Euclid distance in the mass-weighted Cartesian coordinate between reference structures on the reaction route network and a molecular structure of the on-the-fly trajectory at time *t*, and then expresses the dynamical reaction route as a time-series data of reference structures with the shortest distance. In this chapter, I focused on the bifurcation and the isomerization reactions for the Au_5 cluster and investigated the on-the-fly trajectories exploring the PES based on the global reaction route network. Through the analysis of 200 trajectories, I revealed that 114 trajectories undergo the "*IRC-jump*" processes in which they switch from one IRC to another due to traversing the PES valley orthogonal to the original IRC direction. From the bifurcation analysis, I also found that the IRC-jump determines the fate of the product region where the trajectory reaches by considering both the nuclear permutation-inversion (NPI) concept and the IRC-jump behavior.

The on-the-fly trajectory mapping method enables us to trace dynamical reaction processes, but their proper visualization has been challenging due to the multi-dimensionality of PES. The technique for embedding multi-dimensional data in lower-dimensional space is called a dimensional reduction method in data science and is utilized in a wide area in both the natural and social sciences. In **Chapter 3**, I focused on the classical multidimensional scaling (CMDS), one of the dimensionality reduction methods, and visualized two IRCs corresponding to the intramolecular hydrogen transfer reaction of malondialdehyde and the collision reaction of $OH^- + CH_3F \rightarrow CH_3OH + F^-$ onto the two-dimensional coordinate subspace. Thereby, I confirmed that the highly-curved IRC could be reproduced well in the two-dimensional subspace determined by the CMDS method. Furthermore, I applied CMDS to the global reaction route map of the Au_5 cluster, including five minima and 14 transition state structures, and constructed the two- and three-dimensional reaction route maps. Consequently, I concluded that the dimensionality reduction method is a powerful tool to construct the uniquely-defined chemical reaction space and provide the reduced-dimensionality reaction space reflecting the geometrical features of PES.

In order to interpret dynamical reaction routes based on the reaction route map, the on-the-fly trajectory should be projected onto the reduced-dimensionality coordinate space determined by the CMDS method. In **Chapter 4**, I employed the out-of-sample extension method of CMDS (oCMDS), proposed by Trosset and Priebe, to project the on-the-fly trajectory (the out-of-sample data) onto the reduced reaction route map (the original data). As applications, I shed new light on the collision reaction of $OH^- + CH_3F \rightarrow CH_3OH + F^-$ and the isomerization reaction of the Au_5 cluster, as already discussed in Chapter 2 and Chapter 3. The previous theoretical study for this collision reaction reported that about 90% of on-the-fly trajectories starting from the transition state proceeded to not the product region connected by the IRC but a "*non-IRC*" channel deviating from the IRC. In this chapter, I examined the non-IRC dynamics based on the reduced-dimensionality coordinate space by using the CMDS and oCMDS methods and revealed that the non-IRC trajectories originated from the sharply-curved region of the IRC profile. Furthermore, I investigated the isomerization reaction of Au_5 by projecting the on-the-fly trajectories, which were obtained in Chapter 2, onto the two- and three-dimensional reaction space, including five minima, 14 transition state structures, and molecular structures along 14 IRCs. Through these analyses, I clarified the detailed IRC-jump processes traveling on the reduced-dimensionality coordinate space. This dimensionality reduction strategy provides chemical insight into the chemical reaction mechanism and the driving force from both the static reaction route map and the reaction dynamics.

In **Chapter 5**, I tackled the elucidation of excited-state branching reaction dynamics using both the static reaction path analysis and the on-the-fly MD simulations. *Cis*-stilbene is of interest as a fundamental molecule where the *cis*-*trans* photoisomerization and the photocyclization are competitive after the ππ* excitation. Previous studies investigated the excited-state branching mechanisms for *cis*-stilbene (*cis*-SB) and 1,1'-dimethyl-*cis*-stilbene (*cis*-dmSB) and found that the tendency of branching ratio and lifetime for *cis*-SB were opposite to those of *cis*-dmSB. To further understand the methyl-substituent effects for *cis*-SB, I examined the excited-state reaction mechanism for α-methyl-*cis*-stilbene (*cis*-mSB) by comparing it to those of *cis*-SB and *cis*-dmSB. In this chapter, I constructed the two-dimensional reaction space determined by two internal coordinates associated with two competing photochemical reactions and then projected the excited-state reaction network and the on-the-fly trajectories for *cis*-SB, *cis*-mSB, and *cis*-dmSB. From the methyl-substituent feature, the chemical properties for *cis*-mSB are expected to be intermediate between *cis*-SB and *cis*-dmSB. However, the excited-state dynamics indicate that the branching ratio for *cis*-mSB agreed quantitively with *cis*-SB but opposite to *cis*-dmSB. On the other hand, in contrast to the branching ratio, the S_1-population relaxation for *cis*-mSB becomes relatively faster than those for *cis*-SB and *cis*-dmSB because of the non-equivalent methyl-substituent nature. Consequently, this study suggested that the excited-state branching reaction mechanisms for SB-like molecules may be controlled by the substituent introduced to the central ethylenic part.

Chapter 5 defined the two-dimensional reaction space for SB-like molecules by choosing two internal coordinates based on chemical intuition, but it is not unique. To avoid such ambiguity, in **Chapter 6**, I applied the CMDS method to construct three types of two-dimensional reaction route maps for *cis*-SB: the ground-state, the excited-state, or the "*multi-state*" reaction route maps. I also constructed their potential energy landscapes where the potential energy axis is added to the respective two-dimensional maps. Through the analysis of the reduced-dimensionality reaction space, I found that both the ground-state and excited-state maps are successfully represented by two principal coordinates and reproduce the geometrical features of PES. To examine comprehensive non-radiative relaxation processes for ππ*-excited *cis*-SB, I performed the on-the-fly molecular dynamics simulations on both the ground- and excited-states and then projected these trajectories onto the multi-state energy landscape. From these analyses, I found that the trajectories have considerably higher potential energy than the ground-state reaction route map, and therefore, they can easily cross over the transition state related to the cis-trans isomerization on the ground-state PES. Finally, I constructed reduced-dimensionally excited-state reaction space determined by the framework parts of SB, mSB, and dmSB, which could not handle in the conventional CMDS procedure. Consequently, I clarified that the features of each reaction space were qualitatively consistent with the tendency of their excited state dynamics, as discussed in Chapter 5. Combining the reduced-dimensionality reaction route map and the on-the-fly trajectory analysis enables us to uncover photochemical reaction processes based on the multi-state potential energy surfaces that are the stage for chemical reactions.

Through this doctoral thesis, I have developed a new methodology to analyze a dynamical reaction route accompanying multiple elementary reaction processes on the basis of a reduced-dimensionality reaction route map determined by representative structures on the potential energy surface. In addition, by applying the CMDS method to molecular structures belonging to both the ground- and excited-states, I successfully constructed a multi-state reduced-dimensionality potential energy landscape, which enables a comprehensive discussion on the radiative and non-radiative relaxation processes in photochemistry. In order to construct the fruitful reduced-dimensionality reaction space, it is crucial to obtain the appropriate pairwise linear distance. In the molecule case, such a well-defined distance is achieved by properly handling the x-y-z axes' orientation and the nuclear permutation-inversion (NPI) isomers, and I deal with them by the Kabsch algorithm and the merged-NPI procedure, as shown in Chapter 2. However, this preprocessing is cumbersome, and it is challenging to apply this strategy to a large-scale molecular system directly. These difficulties may be resolved by using a new molecular dissimilarity that is not affected by the molecular orientation and the NPI isomers. Also, since the CMDS method is the linear dimensionality reduction method, it cannot incorporate non-linear effects. In data science, a wide variety of linear and non-linear dimensionality reduction methods have been proposed and applied to various problems. The present reduced-dimensionality strategy should be achieved not only by the CMDS method but also by other methods. Therefore, the role of other dimensionality reduction methods, especially non-linear methods, for the visualization of molecular structures should be highlighted in the future. Finally, in this doctoral thesis, the proposed method was employed to analyze chemical reaction mechanisms, but it also has the aspect of the automatic extraction of essential descriptors from the full-dimensional chemical space. From such a viewpoint, I would like to also apply the proposed strategy to data science-based analysis in the future.

Acknowledgments

First and foremost, I am extremely grateful to my supervisor, Prof. Tetsuya Taketsugu, Department of Chemistry, Faculty of Science, Hokkaido University, for his invaluable advice, continuous support, and thoughtful guidance during my life in Quantum Chemistry Laboratory (QCL). I would also like to thank him for giving me many opportunities to further develop my research. His insightful feedback and suggestion pushed me to sharpen my thinking and brought my work to a higher level.

I am deeply grateful to Prof. Satoshi Maeda, Department of Chemistry, Faculty of Science, Hokkaido University, for his valuable advice and fruitful discussion in my studies, especially **Chapter 2** and **Chapter 5**, and for serving as the chief of my doctoral thesis committee.

I would like to express my sincere gratitude to Prof. Tamiki Komatsuzaki, Research Institute for Electronic Science, Hokkaido University; Prof. Jun-ya Hasegawa, Institute for Catalysis, Hokkaido University; Associate Prof. Shin-ichiro Sato, Faculty of Engineering, Hokkaido University, for their constructive suggestions and comments and for serving as members of my doctoral thesis committee.

My sincere thanks to Prof. Zin Arai, Academy of Emerging Sciences, Chubu

University, for his great support during my short-visit and for continuous discussion on **Chapter 3** and **Chapter 4**.

I would like to thank Assistant Prof. Yu Harabuchi, Department of Chemistry, Faculty of Science, Hokkaido University, for his practical guidance, great encouragement, and fruitful discussion during my QCL life and for helpful advice, comment, and enormous contribution to **Chapter 2** and **Chapter 5**.

I would also like to thank Assistant Prof. Yuriko Ono, Institute for Chemical Reaction Design and Discovery (WPI-ICReDD), Hokkaido University, for her great encouragement and continuous discussion in **Chapter 2**, **Chapter 3**, **Chapter 4**, and **Chapter 6**.

I am very grateful to Ms. Rina Yamamoto, who is my senior colleague in QCL, for her practical advice, kind cooperation, and daily discussion during my life in QCL, especially in **Chapter 5**.

I would like to thank the following people for helpful discussions on ultrafast photodissociation dynamics research (*J. Phys. Chem. Lett.* **2021**, 12, 674), although it is not included in my doctoral thesis: Associate Prof. Taro Sekikawa, Mr. Hironori Igarashi, and Mr. Yuki Nitta, Department of Applied Physics in Hokkaido University; Dr. Oliver Schalk, Department of Chemistry, University of Copenhagen; and Assistant Prof. Kenichiro Saita and Mr. Satoi Wada in QCL.

I am deeply appreciative of Mr. Shuichi Ebisawa in QCL for his tolerant discussions on the mathematical aspects of the potential energy hyper-surface (*J. Comput. Chem.* **2021**, 42, 27), which is also not included in my doctoral thesis.

My special thanks to Prof. Srihari Keshavamurthy, Department of Chemistry, Indian Institute of Technology Kanpur, for his many fruitful discussions and inspiring ideas during the half-year he spent in OCL.

I express my gratitude to Prof. Tamiki Komatsuzaki and Associate Prof. Hiroshi Teramoto, Research Institute for Electronic Science, Hokkaido University, for giving me the opportunity to attend the stimulating workshop in Telluride, USA. I am also very grateful to Prof. Toda Mikito, Department of Physics, Faculty of Science, Nara Women's University, and the Komatsuzaki Laboratory members, especially Assistant Prof Yuta Mizuno; Dr. Yutaka Nagahata; and Mr. Ryoichi Tanaka, for their continuous discussions and inspiring suggestions.

I would also like to express my deepest gratitude to Prof. Kiyotaka Asakura, Institute for Catalysis, Hokkaido University, for their great efforts and numerous supports in organizing the Chemical Sciences and Engineering (CSE) Summar School.

I would like to express my many, many thanks to all the past and present QCL members for invaluable discussions, tremendous supports, and great encouragement during all my student life in QCL, particularly Associate Prof. Masato Kobayashi, Assistant Prof. Takeshi Iwasa, Assistant Prof. Kenichiro Saita, Assistant Prof. Min Gao, Dr. Takao Tsuneda, Dr. Tomoko Akama, Dr. Yosuke Sumiya, Dr. Makito Takagi, Mr. Sota Satoh, Mr. Masashi Sampei, Ms. Maki Nakahara, Mr. Hiroshi Morita, Mr. Kohei Oda, Mr. Yuta Iwabuchi, Mr. Shuichi Ebisawa, Ms. Rio Konishi, Mr. Satoi Wada, Mr. Kenichiro Iwata, Mr. Jo Sakugawa, Mr. Masatoshi Hasebe, and Ms. Naoko Kanou.

I also sincerely thank my two colleagues, Mr. Masato Takenaka and Mr. Toshikazu Fujimori, who have maintained a well-balanced relationship during the six years since we joined QCL. The daily discussions and chats with all of you have motivated me to continue my research. Thank you very much. I wish you all the best in your future endeavors.

I would like to thank my family for their great support and continuous encouragement. I am also grateful to all my friends who invited me to activities such as drinking and traveling.

Finally, I was supported by the Ministry of Education, Culture, Sports, Science and Technology (MEXT, Japan) through Program for Leading Graduate Schools (Hokkaido University "Ambitious Leader's Program"), Grant-in-Aid for Japan Society for the Promotion of Science (JSPS, Japan) Fellows Grant Number JP18J20856, and Yamaguchi Masae Memorial Scholarship Foundation. Without their financial supports, I would not have been able to continue my Ph.D. program. I would like to express my heartfelt appreciation for their tremendous supports.